ABSTRACT

Title of dissertation: ANALYSIS OF A WATER VAPOR HELICON THRUSTER USING EMISSION SPECTROSCOPY

Adriane J. Faust, Doctor of Philosophy, 2018

Dissertation directed by: Professor Raymond Sedwick
Department of Aerospace Engineering

A helicon thruster was developed to research the use of emission spectroscopy diagnostics. Helicon thrusters differ from conventional electric propulsion systems in that the conductive components that power the thruster do not contact the plasma propellant. Because of this design, propellants that would be corrosive in conventional thrusters can be used in the helicon thruster. Water vapor is a possible propellant option because it is cheap, easy to store, and available in space for refueling, making it an attractive choice for deep space missions. Conventional invasive plasma diagnostics do not work reliably with water vapor plasma because it is corrosive and contains multiple species of positively and negatively charged particles, which probes that measure only plasma current are unable to distinguish. These probes can also have measurement errors in the presence of radio frequency, electric, or magnetic fields, making analysis of thruster performance difficult.

This research explores the validity of a non-invasive diagnostic technique using emission spectroscopy with a helium seed gas to determine the plasma parameters

for any propellant. A helium collisional radiative model was developed to estimate electron temperature and density from helium emission line ratios measured experimentally. Thruster tests conducted with pure helium were used to compare the collisional radiative model to existing models. Tests with pure argon and an argon/helium mix allow for a comparison of Langmuir probe measurements to the emission spectroscopy results and verification that the helium gas seeding does not significantly affect the thruster performance. The diagnostic technique is then tested on a water vapor/helium mix. The estimates for the electron density predicted those measured by the conventional probes well, but the diagnostic technique is less reliable for electron temperature at the experimental conditions.

ANALYSIS OF A WATER VAPOR HELICON THRUSTER USING EMISSION SPECTROSCOPY

by

Adriane J. Faust

Dissertation submitted to the Faculty of the Graduate School of the
University of Maryland, College Park in partial fulfillment
of the requirements for the degree of
Doctor of Philosophy
2018

Advisory Committee:
Professor Raymond Sedwick, Chair/Advisor
Professor Christopher Cadou
Professor Kenneth Yu
Professor David Akin
Professor Adil Hassam

Table of Contents

List of Tables

List of Figures

List of Abbreviations

α	alpha
β	beta
ϵ	epsilon
η	eta
λ	lambda
μ	mu
ν	nu
ω	omega
π	pi
ρ	rho
σ	sigma
θ	theta
ξ	xi
ζ	zeta
Γ	Gamma
Λ	Lambda
Ω	Omega
Φ	Phi

ANU	Australian National University
ASTRAL	Auburn Steady State Research Facility
CCD	Charge-Coupled Device
CCP	Capacitively Coupled Plasma
CGS-CRM	Constant Ground State Collisional Radiative Model
CRM	Collisional Radiative Model
ECR	Electron Cyclotron Resonance
EP	Electric Propulsion
ICP	Inductively Coupled Plasma
I-V	Current - Voltage
LxCat	Plasma Data Exchange Project
PPT	Pulsed Plasma Thruster
mHTX	MIT Mini-Helicon Thruster Experiment
MPD	Magneto-Plasma-Dynamic
NIST	National Institute of Standards and Technology
OML	Orbital Motion Limited
RF	Radio Frequency
RPA	Retarding Potential Analyzer
TG Waves	Trivelpiece-Gould Waves
UV	Ultra Violet
VASIMR	Variable Specific Impulse Magnetplasma
ZETA	Zero Energy Toroidal Assembly

Chapter 1: Introduction

1.1 Motivation

Current rocket engines can be classified as either chemical propulsion systems or electric propulsion systems. Chemical propulsion systems use the energy stored in chemical bonds in the fuel to accelerate the propellant and generate thrust. Electric propulsion (EP) systems generate thrust using electric and magnetic fields to impart energy to a propellant. EP systems have a much higher specific impulse, but lower thrust than chemical engines, making them a better option for space-based applications such as satellite station keeping and orbital maneuvering where specific impulse and fuel consumption are more important than amount of thrust.

Electric propulsion systems can be classified as electrothermal, electrostatic, and electromagnetic. Resistojets and arcjets are examples of electrothermal propulsion systems. Both heat propellant using electrical energy and expand the gas through a nozzle. The resistojet heats the propellant using resistive heating and the arcjet heats the propellant using an electrical arc. Electrostatic thrusters generate thrust by creating plasma, which is accelerated to high velocities by electrostatic forces. Hall thrusters and ion engines are types of electrostatic thrusters. Plasma is created by electron bombardment from an emitter. The positively charged heavy

particles are accelerated out the thruster exit by charged grids in the case of the ion engine, or an axial electric field in the Hall thruster. Since the exit plume is positively charged, a secondary electron emitter is needed at the exit to neutralize the gas. This prevents the spacecraft from becoming negatively charged, causing the ions to return and reducing the amount of thrust produced. Electromagnetic thrusters also utilize plasma propellant, which is accelerated by electric and magnetic forces. Pulsed plasma thrusters (PPTs), magneto-plasma-dynamic (MPD) thrusters, and helicon thrusters, the subject of this research, are considered electromagnetic thrusters. PPTs use pulsed arcs to ablate and ionize a solid propellant like Teflon. A magnetic field is created by the arc current and the resulting Lorentz force accelerates the ions. MPD thrusters also use the Lorentz force to accelerate ions. Gas enters an annular chamber with a radial electric field that causes the gas to ionize. The high current creates a magnetic field and an axial Lorentz force. The helicon thruster uses a radio frequency (RF) antenna around a tube containing propellant gas to create a time varying magnetic field, which in turn induces a curling electric field. The electric field accelerates free electrons which ionize the gas. An axially applied magnetic field allows for the formation of helicon waves. Charged particles accelerate through a plasma sheath layer that forms at the thruster exit.

Helicon thrusters have several advantages over conventional EP systems. Helicon plasma sources have a higher ionization efficiency than capacitively and inductively coupled plasma sources. The exhaust plume is quasi-neutral, eliminating the need for a neutralizer electrode at the thruster exit. The antenna is not immersed in the plasma, therefore the lifetime of the thruster is not limited by emitter or

grid erosion, and propellants that would be corrosive to other EP systems can be considered. Conventional thrusters use noble gas propellants like argon and xenon because they are not reactive. One unconventional propellant possibility for the helicon thruster is water vapor. Water vapor is cheap, safe to store, and can be found in space, making refueling a possibility. For example, Saturn's moon Enceladus emits plumes of water from its surface. A water vapor powered propulsion system could be used on a mission to explore such an environment.

Determining the performance of water vapor helicon plasma using conventional diagnostic tools presents challenges for the same reasons that prevent water vapor from being used in conventional EP systems. Plasma diagnostic tools like Langmuir probes and retarding potential analyzers consist of wires or metal grids that must be immersed in the plasma. Besides exposure to a corrosive environment in addition to electric, magnetic, and radio frequency (RF) fields, analysis from conventional probes proves difficult because they are unable to distinguish charged particle species in a molecular plasma. Water vapor plasma contains negatively charged hydroxide ions which are indistinguishable from electrons to a probe that measures only the total current. An alternative diagnostic technique that can work reliably with molecular plasma is needed.

1.2 Objective

The purpose of this research is to develop a non-invasive diagnostic tool for determining the performance characteristics of a helicon thruster powered by water

vapor plasma. Emission spectroscopy requires only a light of sight to the plasma, is unaffected by RF, electric, or magnetic fields, and can determine all the species present. This is advantageous for molecular plasmas, however, the analysis to determine the plasma parameters of electron temperature and electron density is complicated. A complex model of the transitions between excited states in the atoms or molecules as the result of particle interactions, called a collisional radiative model (CRM), is needed to predict emission line intensity. Electron temperature and density are inputs to the model which calculates a set of simulated emission lines for the given conditions. The CRM's complexity increases exponentially for molecular plasmas. The CRM also relies heavily on quantum mechanical data, such as collisional cross sections as a function of electron temperature, which are sparse for molecular plasmas. A simple gas like helium is a better candidate for developing a higher fidelity model. The necessary quantum data are readily available. To enable analysis with a simpler helium CRM, the main propellant gas is seeded with a small amount of helium gas. The intensities of helium emission lines in the observed spectrum were measured and compared to the CRM output. Because intensity is an arbitrary unit, the ratios of pairs of emission lines are used for the comparison. This helium seeding technique with line intensity ratio analysis is beneficial because it can be used to determine the plasma parameters for any propellant gas, regardless of its complexity.

A new helium CRM was developed using recently updated collisional cross sections and assumptions that model the experimental conditions, such as maintaining a constant ground state helium population to account for the flow of gas

from the tank, and metastable diffusion to the thruster walls. Helicon thruster tests were completed with pure helium, pure argon, argon/helium mixed gas, and water vapor/helium mixed gas. The pure helium tests were analyzed with both a simple corona model and the CRM. The argon/helium mixed gas tests were conducted to test the helium seeding technique with a noble gas that can also be analyzed with conventional probes. The pure argon tests were compared to the argon/helium mixed gas results for the conventional probes to determine how small amounts of helium affected the performance of the gas. The water vapor/helium mixed gas tests were conducted to demonstrate the helium seeding emission spectroscopy diagnostic with a molecular plasma.

1.3 Contributions of Thesis

This study made several contributions including the following: the development of a constant ground state helium CRM with updated cross sections and coefficients that can be solved exactly; addition of specific experimental conditions in the model including keeping the ground state population constant to account for the continuous propellant flow and metastable diffusion to the walls; demonstration that uncertainty in the collisional cross sections does not allow for accurate plasma parameter estimates at the helicon thruster operating conditions; and spectroscopic analysis of water vapor plasma in a helicon thruster using helium seed gas and line ratio comparison.

1.4 Outline of Thesis

Chapter 2 is a literature review including the history of the helicon thruster and the use of emission spectroscopy diagnostics in plasma research.

Chapter 3 describes the physics of helicon waves.

Chapter 4 discusses the experimental setup, including the helicon thruster, Langmuir probe diagnostics, and emission spectroscopy instruments.

Chapter 5 lists the steps in experimental procedure and describes the data analysis methods.

Chapter 6 provides a detailed description of the helium collisional radiative model.

Chapter 7 discusses the experimental results.

Chapter 8 provides the conclusion to the thesis.

Chapter 2: Literature Review

The literature review contains a history of the study of helicon waves and the possible plasma generation mechanisms. The development of the helicon thruster, the use of emission spectroscopy in helicon plasmas, and previous applications of helium line ratio analysis are discussed.

2.1 Helicon Waves

Helicon waves are a type of low frequency electromagnetic wave called a whistler wave. Whistler waves were first observed during World War I as whistling tones picked up over long telephone cables meant to detect enemy signals. The descending whistling tones were first mentioned by Barkhausen in 1919, and he later attributed them to wave reflection off the Heavyside layer caused by lightning strikes [1]. Hartree and Appleton derived the dispersion relation for whistler waves as a function of electron plasma frequency, the electron cyclotron frequency, and the angle between the wave vector and the magnetic field [2, 3]. Storey later simplified the relation by considering only the low frequency, high refractive index case to show that there is a maximum angle between the wave vector and the magnetic field, and the waves must propagate close to the magnetic field lines [4]. A lightning strike

provides a source with a broad frequency spectrum, which propagates along Earth's magnetic field lines in the dispersive plasma of the ionosphere.

The helicon wave is a whistler wave bounded by a transverse magnetic field. Helicon waves were discovered in laboratory solid state plasma by Aigrain in 1960 while studying waves in solid metals [5]. He observed waves in low temperature sodium that propagated at a frequency between the ion cyclotron and electron cyclotron frequencies. Since the waves electric field had a helical shape as it propagated along the magnetic field lines, he named them "helicon" waves. Several years later, both Legéndy and Klozenberg, McNamara, and Thonemann suggested a theory for the propagation of helicon waves in a cylindrical plasma [6, 7]. Helicon waves in a gaseous plasma were first observed, however, in a toroidal plasma source called the Zero Energy Toroidal Assembly (ZETA) [8]. The first experiment using a cylindrical plasma ignited by an RF power source was conducted by Lehane and Thonemann in 1965 [9]. The radial and longitudinal variation of the wave fields were measured by magnetic probes and the plasma density was measured by a Langmuir probe. The dispersion of the waves matched the theory presented by Klozenberg, McNamara, and Thonemann. Boswell first investigated the helicon wave properties and the high efficiency of helicon plasma created in an RF powered cylindrical source [10]. His experiment consisted of a 10 cm diameter Pyrex glass tube surrounded by a double loop antenna. Solenoid electromagnets around the tube and antenna assembly provided an axial magnetic field up to 1500 G. The antenna was powered by an 800 W, 8 MHz RF power supply. The tube was filled with argon gas at a pressure of $2\text{x}10^{-3}$ mbar. The plasma density was measured with a Langmuir probe and

peaked in the center of the tube at $4x10^{18}\,m^{-3}$. This value for plasma density is high for the amount of power needed to produce it compared to capacitively coupled plasma (CCP) and inductively coupled plasma (ICP) sources. Because of the high ionization efficiency of helicon plasma sources, they are used for several applications, including plasma processing [11–14], semiconductor etching [15], and space propulsion [16]. The mechanism responsible for this high ionization efficiency in helicon waves is still debated.

2.2 Mechanisms for Efficient Plasma Generation in Helicon Waves

Helicon waves are non-resonant waves capable of generating plasma efficiently. There are several mechanisms proposed that could be responsible for particle ionization including collisional and Landau damping [17], and electron cyclotron interaction [18]. Boswell discovered in his early helicon plasma source experiments, a collision frequency several orders of magnitude higher than the Coulomb collision frequency was needed to explain the ionization rate [10]. Chen proposed that inclusion of Landau damping could explain the energy absorption [17]. In a helicon plasma source experiment completed by Komori *et al.*, good agreement was also found by taking into account both collisional and Landau damping with Landau damping being the more prominent effect [19]. Experimental support for the Landau damping hypothesis also came from Keiter *et al.* who found that the maximum plasma density and minimum power needed to ignite a helicon wave is a function of magnetic field strength and tube geometry [20]. Landau damping could account for

the plasma density if the limit of the helicon wave was taken to be the radius of the tube instead of the radius of the vacuum chamber. Despite these promising experimental and theoretical results supporting Landau damping as the mechanism for plasma production, Chen and Blackwell reported that no non-Maxwellian electron distribution was ever directly measured after several years of conducting helicon experiments [21]. They experimentally disproved the existence of a high energy electron tail, or a high energy electron density was insignificantly small, using a time-resolved gridded analyzer, which negates the possibility of Landau damping being the heating mechanism.

Another possible mechanism for plasma generation are Trivelpiece-Gould waves. Trivelpiece-Gould (TG) waves are quasi-electrostatic waves that couple with helicon waves to deposit energy at the core of the plasma. Shamrai and Taranov were able to match their experimental values for plasma density to theory if there was a conducting boundary at the surface [22]. TG waves form at the surface of plasma tube if the plasma is not in good conductive contact with the wall. Borg and Boswell amended the cold plasma theory using a finite electron mass to describe both helicon and TG waves [23]. A 2-D computer model of helicon antenna coupling, wave propagation, Landau damping, and collisional damping heating mechanisms was developed [24]. The model predicted that TG modes dominate at low magnetic field strengths because the thickness of the TG waves at the plasma boundary is large and extends deeper into the plasma core [25], whereas collisional damping dominates at higher pressures and densities. Landau damping can have a significant effect at low pressures. TG waves in a helicon plasma source were measured with a J-dot probe,

similar to a Rogowski coil, by Blackwell *et al.* [26]. The TG waves were observed in only a thin layer at the surface of the plasma tube and were detectable only in magnetic fields below 50 G. Other experiments suggested ion heating was due to Landau damping of TG waves in the ions [27, 28].

2.3 Helicon Thruster

The helicon plasma source was first proposed for use in electron propulsion systems as a plasma generator for an electron cyclotron resonance (ECR) thruster and the Variable Specific Impulse Magnetoplasma Rocket (VASIMR) [16, 29]. The helicon is an attractive plasma source because it has a higher ionization efficiency than capacitively or inductively coupled plasma sources, and the antenna is on the outside of the plasma tube making these systems electrodeless. The first mention of the helicon plasma source alone as a possible thruster came from the Chi-Kung experiment at Australian National University (ANU) [30]. The Chi-Kung experiment consisted of a 15 cm diameter, 32 cm long glass tube, two solenoid magnets capable of producing up to 250 G, a diffusion chamber, and a grounded aluminum plate at one end of the tube. The system was powered by a 13.56 MHz RF power supply. The glass tube was filled with argon at a constant pressure of $4\text{x}10^{-3}$ mbar. The ion energy distribution function of the exit plume was measured using a retarding potential analyzer (RPA) and the results showed the presence of a current-free double layer, a region where plasmas at two different plasma potentials meet. This phenomenon is characterized by a stationary plasma and a supersonic ion beam,

indicated by a double energy peak in the RPA data [31]. Keesee *et al.* corroborated the RPA measurements of the ion energy distribution function with a laser-induced fluorescence diagnostic, confirming the presence of the supersonic ion beam in argon [32]. Gesto *et al.* confirmed that thrust is produced from a helicon double-layer thruster by studying the ion orbits in the exhaust [33]. A computer simulation was used to determine that the ions in the beam do not lose momentum because they detach from the magnetic field lines. The ion beam divergence angle was later measured experimentally with an RPA [34]. To determine if the current-free double-layer formation was the result of the plasma exhaust exiting into a vacuum chamber of finite volume, West *et al.* conducted a test of the ANU helicon double layer thruster in a space-simulation chamber [35]. RPA diagnostics revealed that the ion beam formed and varied in a way consistent with previous experiments. The ion energy distribution profile did not change as the RPA was moved downstream of the exit, proving that the helicon double layer thruster will operate in space. The beam velocity was dependent on the pressure of the argon gas, tested in the range of $5.3\text{x}10^{-4}$ and $2\text{x}10^{-4}$ mbar. Chen proposed that the double layer was in fact a single plasma sheath formed by the diverging magnetic field lines at the thruster exit and showed that experimental results could be explained by classical sheath theory [36]. The single sheath theory may be more applicable to space propulsion since the outside pressure would be below $2\text{x}10^{-4}$ mbar. Double layer experiments conducted by Plihon *et al.* showed that only a single plasma sheath exists at pressures below $1\text{x}10^{-4}$ mbar [37].

Several laboratories in addition to the Plasma Research Laboratory at ANU

have researched helicon thrusters. The University of Washington built and tested a high power helicon thruster capable of producing 1 N of thrust by operating at low frequency (0.5−1 MHz) and high power (50 kW) [38]. Plihon *et al.* reported comparable performance to the ANU helicon thruster using an RPA and Langmuir probes with argon gas in their prototype at the Laboratorie de Physique et Technologie des Plasmas at CNRS - Ecole Polytechnique [39]. The MIT Mini-Helicon Thruster Experiment (mHTX) uses a smaller tube diameter (2 cm), Helmholtz coil magnets that produce up to 1800 G, and an 800 W 13.56 MHz RF power supply to produce between 1−3 mN of thrust [40]. Toki *et al.* also developed a small diameter (2.5 cm) helicon thruster but were unable to produce the amount of thrust needed for space propulsion, possibly due to large losses at the tube walls [41].

To reduce power usage and thruster mass, several groups have proposed permanent magnet helicon thrusters, which would eliminate the need for an electromagnet power supply [40,42–44]. While most tests of the permanent magnet systems showed promising performance, one group reported that they were unable to create an ion beam with only permanent magnets [42]. Eliminating cusps in the magnetic field was necessary for beam formation and electromagnets were used in conjunction with permanent magnets to achieve thrust.

Most helicon thruster testing has been done using conventional noble gas propellants. The majority of the experiments mentioned in the above research summary were conducted with argon. The VASIMR helicon plasma source has been tested with light gases: helium, deuterium, and hydrogen [45]. ANU tested their helicon double layer thruster with hydrogen and xenon and reported behavior comparable

to the argon tests [46]. The MIT mHTX has been tested with neon, xenon, and N_2 in addition to argon [47]. Water vapor as a propellant for a space propulsion system has not been extensively tested. A water vapor fueled helicon source was presented as an efficient method of hydrogen dissociation [48, 49]. The diagnostics used were a Langmuir probe to measure electron temperature and plasma density, a residual gas analyzer to measure the concentrations of different species in the plasma, and an emission spectrograph, also used for species identification. A small water vapor powered helicon thruster is being considered for CubeSat propulsion [50].

2.4 Helium Emission Line Analysis

Using emission line ratios to determine the electron temperature of helium plasma was first proposed by Cunningham, who used the triplet-singlet pairing of 471/492 nm to find electron temperature with a corona model [51]. Because triplet lines are more sensitive to changes in electron temperature instead of electron density, singlet-triplet ratios can be used to determine the temperature. Later research expanded the line ratio diagnostic technique to use additional helium line ratios and CRM instead of the corona model [52–54]. This helium line ratio diagnostic technique has been used to determine plasma parameters in electron cyclotron resonance heated plasma, fusion divertor simulators, edge plasma in a reversed field pinch, stellarators, atmospheric glow discharge, Tokamaks, and a helicon plasma source [55–68].

The corona model is simplified model of electron interactions with excited

atoms that can be used to predict the electron temperature for low density plasmas. In this model, radiative processes dominate collisional processes, so only excitation from the ground state and radiative decomposition are considered. In plasmas with electron densities higher than $10^{16}\mathrm{m}^{-3}$, collisional processes become significant. The corona model simplifications are no longer valid, and a collisional radiative model is required to find the electron temperature and density. Bates *et al.* first developed the collisional radiative model, which expanded on the corona model to include collisional processes among higher energy states [69]. The collisional radiative model developed for this study is based on the helium model first described by Fujimoto in 1979, updated by Sasaki in 1996, and later revised by Goto in 2003 [70–72]. Several papers have been published describing emission line measurements and a CRM used to determine the performance of a helicon thruster for noble gases like helium, argon, and xenon [73–75].

Chapter 3: Helicon Wave Physics

A helicon wave is a low frequency electromagnetic wave similar to a ionospheric whistler wave. Helicon waves have a frequency between the ion cyclotron frequency and the electron cylcotron frequency, and are bounded by a cylinder. This chapter includes the derivation of the dispersion relation and waveform equations for the helicon wave. The two suggested mechanisms for ionization via helicon wave, Landau damping and Trivelpiece-Gould modes, are discussed. The chapter concludes with a description of a single layer plasma sheath and how it acts to produce thrust.

3.1 Dispersion Relation

The dispersion relation describes how helicon waves travel in the plasma by relating the wavelength, λ, or the wavenumber, k, to the frequency, ω. The derivation starts with Maxwell's equations and Ohm's Law.

$$\nabla \cdot \vec{B} = 0 \tag{3.1}$$

$$\nabla \times \vec{E} = \frac{-\partial \vec{B}}{\partial t} \tag{3.2}$$

$$\nabla \times \vec{B} = \mu_0 \vec{j} + \epsilon_0 \frac{\partial \vec{E}}{\partial t} \tag{3.3}$$

$$\rho \vec{j} = \vec{E} + \vec{v_e} \times \vec{B} \tag{3.4}$$

where $\vec{B}$ is the magnetic field, $\vec{E}$ is the electric field, t is time, $\vec{j}$ is the current density, $\vec{v}_e$ is the electron velocity, μ_0 is the permeability in vacuum, ϵ_0 is the permittivity in vacuum, and ρ is the resistivity of the plasma. Only the magnetic field acts in the axial, or $\hat{z}$ direction ($E_z = 0$), so $\rho = 0$. Ion motion can also be neglected because the frequency of the helicon wave is greater than the ion cyclotron frequency, so $\vec{j} = -en_0 \vec{v}_e$, where e is the electron charge and n_0 is the plasma density. Therefore, Eq. 3.4 can be rewritten as

$$\vec{E} = \frac{\vec{j} \times \vec{B}}{en_0}. \tag{3.5}$$

Substituting Eq. 3.5 into Eq. 3.2 and simplifying with vector identities gives the time rate of change of the magnetic field.

$$\frac{-\partial \vec{B}}{\partial t} = (\vec{B} \cdot \nabla) \frac{\vec{j}}{en_0} \tag{3.6}$$

Assume perturbations of $\vec{B}$ and $\vec{j}$ take the form $\exp i(m\theta + kz - \omega t)$, where k is the wavenumber, θ is the angle between k and B, and ω is the perturbation frequency. The magnetic field is axial, $\vec{B} = B\hat{z}$. The perturbed Eq. 3.6 becomes:

$$i\omega \vec{B} = \frac{ikB}{en_0} \vec{j} \tag{3.7}$$

Substituting Eq. 3.3 in for $\vec{j}$ gives the following equation for the magnetic field.

$$\vec{B} = \frac{k}{\omega} \frac{B}{en_0\mu_0} \nabla \times \vec{B} \tag{3.8}$$

Equation 3.8 can be rewritten in terms of the speed of light in vacuum, c, the plasma frequency, ω_p, and the electron cyclotron frequency, ω_c.

$$\nabla\times \vec{B} = \frac{\omega}{k}\frac{\omega_p^2}{c^2\omega_c}\vec{B} \tag{3.9}$$

The plasma and electron cyclotron frequencies are defined as follows.

$$\omega_p^2 = \frac{\mu_0 c^2 n_0 e^2}{m_e} \tag{3.10}$$

$$\omega_c = \frac{eB}{m_e} \tag{3.11}$$

The dispersion relation for a helicon wave is defined as the quantity α.

$$\alpha \equiv \frac{\omega}{k}\frac{\omega_p^2}{c^2\omega_c} \tag{3.12}$$

3.2 Helicon Waveform

The solutions for helicon wave modes can be found using Eqs. 3.9 and 3.12.

$$\nabla\times \vec{B} = \alpha\ \vec{B} \tag{3.13}$$

Taking the curl of both sides results in the following.

$$\nabla^2\ \vec{B} + \alpha^2\ \vec{B} = 0 \tag{3.14}$$

The $\hat{z}$ component of Eq. 3.14 can be expressed in cylindrical coordinates where r is the radial component, to get Bessel differential equation with mode number, m.

$$\frac{\partial^2 B_z}{\partial r^2} + \frac{1}{r}\frac{\partial B_z}{\partial r} + \left(\alpha^2 - k^2 - \frac{m^2}{r^2}\right) B_z = 0 \tag{3.15}$$

The components of the magnetic field can be expressed in cylindrical coordinates as functions of the electric field, E, the amplitude, A, the transverse wavenumber, $T \equiv \sqrt{\alpha^2 - k^2}$, and the Bessel function solution for $r = 0$, $J_m(Tr)$ [17].

$$B_r = -\frac{k}{\omega}E_\theta = \frac{2A}{T}\left[\frac{m\alpha}{r}J_m(Tr) + k\frac{\partial J_m(Tr)}{\partial r}\right]\cos(m\theta + kz - \omega t) \tag{3.16}$$

$$B_\theta = \frac{k}{\omega}E_r = -\frac{2A}{T}\left[\alpha\frac{\partial J_m(Tr)}{\partial r} + \frac{mk}{r}J_m(Tr)\right]\sin(m\theta + kz - \omega t) \tag{3.17}$$

$$B_z = 2ATJ_m(Tr)\sin(m\theta + kz - \omega t), E_z = 0 \tag{3.18}$$

3.3 Landau Damping

Landau damping is one of the possible explanations for the high ionization efficiency of helicon waves. Landau damping is a damping process that occurs in plasma without charged particle collisions. The process is analogous to a boat riding atop a wave. If the boat travels slower than the wave, it will be accelerated and the wave will lose energy accelerating the boat. If the boat travels faster than the wave, it will lose energy and conversely accelerate the wave. Primary electrons traveling slower than the helicon wave get accelerated, creating a larger population of electrons near the ionization energy of the gas, and therefore resulting in a higher ionization fraction.

The contribution from Landau damping to the effective collision frequency in the plasma, ν_{LD}, is derived by Chen [17]. Linearizing Eq. 3.5, gives an equation of motion in terms of the collision rate, ν.

$$\vec{E} = \frac{\vec{j} \times \vec{B}}{en_0} - \frac{im}{n_0 e^2}(\omega + i\nu)\ \vec{j} \tag{3.19}$$

Taking only the axial component of the current density in the $\hat{z}$ direction yields the following equation without damping.

$$j_z = \frac{i\epsilon_0\omega_p^2}{\omega}E_z\left(1 - \frac{i\nu}{\omega}\right) \tag{3.20}$$

Adding the Landau damping component to Eq. 3.20 gives,

$$j_z = \frac{i\epsilon_0\omega_p^2}{\omega}E_z\left(1 - \frac{i\nu}{\omega} - 2i\sqrt{\pi}\zeta^3\exp^{-\zeta^2}\right) \tag{3.21}$$

where the Landau damping frequency is

$$\nu_{LD} = 2\sqrt{\pi}\omega\zeta^3\exp^{-\zeta^2} \tag{3.22}$$

and

$$\zeta = \frac{\omega + i\nu}{kv_{th}} \tag{3.23}$$

The thermal velocity, v_{th} is a function of the Boltzmann constant, k, the electron mass, m_e and temperature, T_e.

$$v_{th} = \sqrt{\frac{2kT_e}{m_e}} \tag{3.24}$$

The damping frequency, ν_{LD}, reaches an asymptotic maximum when ζ is $\sqrt{3/2}$, corresponding to

$$\nu_{LD}(max) = 1.45\omega \tag{3.25}$$

The maximum value of the electron density of the plasma where Landau damping has a larger effect than collisional damping can be calculated using Eq. 3.25. The ion-electron collision frequency, ν_{ie}, is a function of the bulk electron density, n_0, in m^{-3}, ion charge, Z, the plasma parameter, Λ, and T_e.

$$\nu_{ie} = 2.9x10^{-12}n_0ZT_e^{3/2}\ln\Lambda \tag{3.26}$$

The plasma parameter is a function of the electron density, n_e, and the Debye length, λ_D.

$$\Lambda = 4\pi n_e \lambda_D^3 \tag{3.27}$$

The Debye length is dependent on both electron density, n_e, and electron temperature, T_e.

$$\lambda_D = \sqrt{\frac{\epsilon_0 k T_e}{n_e e^2}} \tag{3.28}$$

The maximum value of n_0 is determined by setting the maximum Landau damping frequency, Eq. 3.25, equal to the ion-electron collision frequency, Eq. 3.26. Assuming the following values based on typical measurements in the helicon thruster used for this study, $Z = 1$, $T_e = 5\,\mathrm{eV}$, and $\ln\Lambda = 15.6$. The upper limit for n_0 as a function of frequency is

$$n_0 = 3.75\text{x}10^{11}\omega = 3.75\text{x}10^{11} \times 2\pi f \tag{3.29}$$

For a frequency of 13.56 MHz, the Landau damping limit is $3.2\text{x}10^{19}\,\mathrm{m}^{-3}$. This density limit is larger than the density measurements in the helicon thruster.

3.4 Trivelpiece-Gould Modes

Trivelpiece-Gould (TG) waves are electrostatic waves that form on the surface of cylindrically bounded plasma with an axial magnetic field. This conducting layer at the thruster tube walls transfers energy into the bulk plasma as it propagates. TG waves were proposed as the mechanism contributing to high ionization efficiency of helicon waves by Shamrai [22]. Measurements supporting the presence of TG modes in a helicon plasma source was made by Blackwell *et al.* [26].

Helicon waves and TG waves are both solutions to the dispersion wave equation. For the frequency range where $k_\parallel c/\omega \gg 1$, the dispersion relation is

$$\frac{k^2c^2}{\omega^2} = \frac{\omega_p^2}{\omega(\omega_c(k_\parallel/k) - \omega(1 + i\nu/\omega))} \tag{3.30}$$

where k is the total wavenumber, $k_\parallel$ is the longitudinal wavenumber, and ν is the electron collision frequency with both ions and neutrals. Rewriting Eq. 3.30 in terms of ω can be used to find the two solutions.

$$\omega = \omega_c \left(\frac{k_\parallel}{k}\right) \frac{k^2c^2}{\omega_p^2 + k^2c^2} \left(1 - \frac{i\nu}{\omega_c(k_\parallel/k)}\right) \tag{3.31}$$

The helicon wave is given by the limit where $kc \ll \omega_p$ and is weakly damped since the term multiplied by $i\nu$ is small.

$$\omega = \frac{\omega_c k_\parallel kc^2}{\omega_p^2} - i\nu\frac{kc^2}{\omega_p^2} \tag{3.32}$$

Conversely, The TG wave is given by the limit where $kc \gg \omega_p$ and is heavily damped by collisions. This is the mechanism by which energy is transfered to electrons in the plasma.

$$\omega = \frac{\omega_c k_\parallel}{k} - i\nu \tag{3.33}$$

Conditions at the tube walls support the propagation of TG waves, while helicon waves propagate in the bulk plasma. The TG wave surface layer in the plasma is thin due to the strong damping. TG waves will form in helicon plasma when the following conditions are met [22]. The critical axial magnetic field value is defined as B_* and is a function of the antenna radius, r_0.

$$B_* = \frac{m_e c\omega^2}{e\nu k_\parallel r_0} \tag{3.34}$$

The quantity d_* is the critical non-conductive gap distance between the plasma and the antenna.

$$d_* = \frac{R\beta}{2|m|} \tag{3.35}$$

R is the radius of the plasma tube, m is the mode number, and β is a dimensionless parameter.

$$\beta = \frac{\omega_c k_\parallel c^2}{\omega_p^2} \tag{3.36}$$

3.5 Single Layer Plasma Sheath

Charged particles are accelerated out the helicon thruster exit by a plasma or Debye sheath, a layer of plasma with a higher density of positively charged ions. A single layer plasma sheath forms when the plasma interacts with a surface. The surface acquires a negative potential relative to the plasma because the electron flux is much greater than the ion flux. Though there is no surface at the thruster exit, a single layer sheath forms from expansion of the axial magnetic field and behaves the same way as a sheath created by a conductive surface [36].

The ion and electron fluxes through a plane in the plasma are given by the product of the ion or electron number density, n_i and n_e, and the thermal speed of the particle. Thermal speed is a function of the particle temperature, T, the particle mass, m, and the Boltzmann constant, k.

$$\Gamma_i = \frac{n_i}{4}\sqrt{\frac{8kT_i}{\pi m_i}} \tag{3.37}$$

$$\Gamma_e = \frac{n_e}{4}\sqrt{\frac{8kT_e}{\pi m_e}} \tag{3.38}$$

If the densities of ions and electrons are approximately equal, meaning the plasma is quasi-neutral, the ratio of the electron flux to the ion flux is proportional to $\sqrt{T_e m_i / T_i m_e}$. Electrons are far more energetic and less massive than ions, so initially, $\Gamma_e \gg \Gamma_i$. As the potential at the surface drops, the electrons get repelled while ions accelerate towards the wall until equilibrium is reached and $\Gamma_e = \Gamma_i$.

To reach particle flux equilibrium, a region of plasma near the wall must exist where the ion density is greater than the electron density. The electron density as a function of distance to the wall, z, can be expressed as the product of the electron density in the bulk plasma, n_0, and the velocity distribution function where v_e is the electron velocity. In the bulk plasma, $z = 0$, and the plasma potential, $\Phi = 0$. Assuming a Maxwellian distribution of electrons:

$$n_e(z) = n_0 \int_{-\infty}^{\infty} \left(\frac{m_e}{2\pi k T_e} \right)^{3/2} \exp\left(\frac{-\frac{1}{2} m_e v_e^2(z) + e\Phi(z)}{k T_e} \right) d\,\vec{v} \tag{3.39}$$

At the wall, Eq. 3.39 becomes

$$n_e = n_0 \exp\left(\frac{e\Phi_w}{k T_e} \right) \tag{3.40}$$

where Φ_w is the potential at the wall.

The ion density at the wall can be found assuming the ions are cold compared to the electrons and are therefore monoenergetic, not Maxwellian. Using expressions for the ion energy and conservation of ion flux, the ion density at the wall as a function of the bulk density can be found. The kinetic and potential energy of the ions is given by the velocity of the ions, v_i, and the potential, Φ. The velocity of the ions in the bulk plasma where $\Phi = 0$ is v_{i0}.

$$\frac{1}{2} m_i v_{i0}^2 = \frac{1}{2} m_i v_i(z)^2 + e\Phi(z) \tag{3.41}$$

The ion flux is the product of the ion density and the ion velocity.

$$n_0 v_{i0} = n_i(z) v_i(z) \tag{3.42}$$

Substituting Eq. 3.41 into Eq. 3.42 gives an expression for ion density.

$$n_i = n_0 \left(1 - \frac{2e\Phi_w}{m_i v_{i0}^2}\right)^{-1/2} \tag{3.43}$$

The structure of the plasma sheath is shown in Fig. 3.1, indicating the bulk plasma, the sheath region at the wall where the ion density is higher than the electron density, and the pre-sheath in between, a region of quasi-neutral plasma where the ions are accelerated due to a potential drop from $\Phi = 0$ to some lower pre-sheath potential, Φ_{ps}. The ions are accelerated from v_{i0} to the Bohm velocity:

$$v_B = \sqrt{\frac{kT_e}{m_i}} \tag{3.44}$$

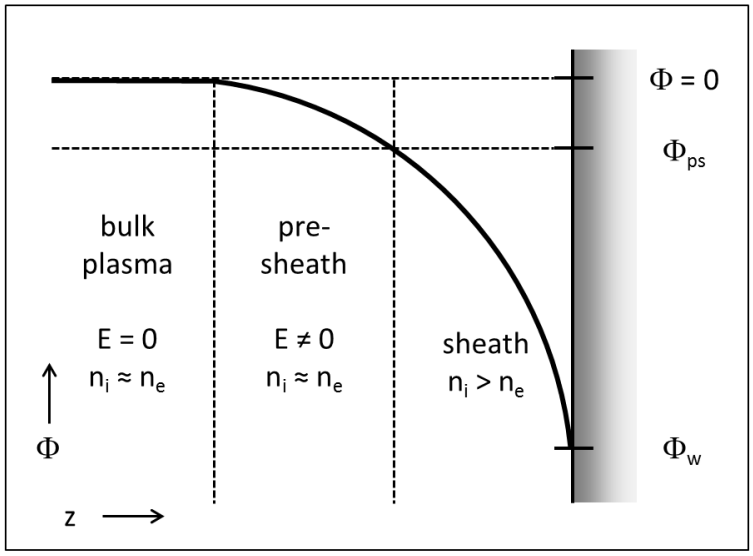

Figure 3.1: Single layer plasma sheath diagram.

Because the plasma in the pre-sheath is quasi-neutral, the ion density at the edge of the pre-sheath is equal to the electron density at $\Phi = \Phi_{ps}$. The ion energy equation for the bulk plasma and the ion energy at the edge of the pre-sheath can be used to find Φ_{ps}.

$$\frac{1}{2}m_i\left(\frac{kT_i}{m_i}\right) = \frac{1}{2}m_i\left(\frac{kT_e}{m_i}\right) + e\Phi_{ps} \tag{3.45}$$

Approximating $(T_e - T_i)$ as T_e since the ions are much colder than the electrons, yields an expression for Φ_{ps} as a function of T_e.

$$\Phi_{ps} = -\frac{1}{2}\frac{kT_e}{e} \tag{3.46}$$

This value can be substituted into Eq. 3.40 for the potential, resulting in an expression for the electron density at the boundary of the pre-sheath and sheath.

$$n_e = n_0 \exp\left(-\frac{1}{2}\right) \tag{3.47}$$

This is the sheath criterion. A single layer sheath forms when this density condition is met.

Magnetic field expansion at the exit of the helicon thruster causes a sheath to form without a surface being present in the plasma [36]. The conditions in the thruster tube are defined by the axial distance $z = 0$ and the potential, $\Phi_0 = 0$. The tube radius is r_0, the magnetic field strength is B_0, and the electron density is the bulk plasma density, n_0. The plasma expands into free space as it leaves the tube and the new values of B and n can be related to the radius of expansion, r.

$$\frac{B}{B_0} = \frac{n}{n_0} = \left(\frac{r_0}{r}\right)^2 \tag{3.48}$$

Equation 3.40 indicates that as the electron density decreases along z, the potential, Φ, must also decrease since T_e is constant. At some value of z, the exponent $e\Phi/kT_e = -\frac{1}{2}$. This is the value of the electron density at the edge of the pre-sheath for the case of a plasma contacting a surface. The sheath criterion is therefore met and a single layer sheath forms at the thruster exit. To find the expansion radius at which this occurs, the sheath criterion is substituted into Eq. 3.48.

$$\frac{n}{n_0} = \left(\frac{r_0}{r}\right)^2 = \exp\left(-\frac{1}{2}\right) \tag{3.49}$$

$$r = \exp\left(\frac{1}{4}\right) r_0 = 1.28 \tag{3.50}$$

The thruster exit sheath forms when the plasma expands to 1.28 times the tube radius.

Chapter 4: Experimental Setup

The helicon thruster experiment consists of the thruster itself, including the glass tubes and antenna, the radio frequency power system, the Helmholtz coils, and the gas feed system. The diagnostic tools include Langmuir probes and an emission spectroscopy system.

4.1 Thruster

The helicon thruster consists of a single turn helical antenna and electromagnets wrapped around the outside of a glass tube. Gaseous propellant is fed into one end of the tube. When the antenna is powered by an RF power supply, the current flowing through it causes a time varying magnetic field, which creates a curling electric field inside the tube. Free electrons in the gas get accelerated by the electric field and generate a plasma when they reach the ionization energy. The electromagnets provide an axial magnetic field, allowing for the formation of helicon waves. The thruster operates only in vacuum, and the formation of a plasma sheath at the thruster exit due to the density difference and diverging magnetic field lines, accelerates charged particles out the exit.

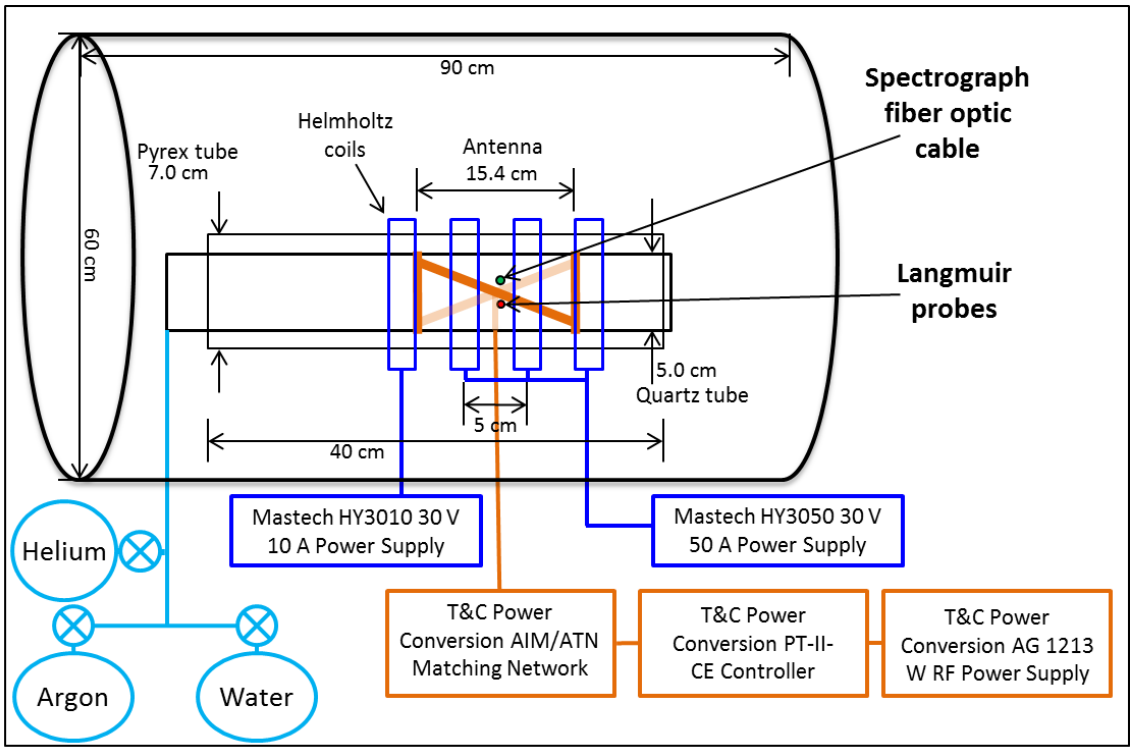

Figure 4.1: Diagram of the helicon thruster setup in the vacuum chamber. The helical antenna and RF power system are shown in orange. The Helmholtz coil magnets and power supplies are shown in blue. The gas system is shown in cyan. The green circle shows the location of the spectrograph fiber optic cable. The red circle shows the location of the Langmuir probes.

4.2 Thruster Tube Dimensions

The helicon thruster is made of a 7 cm diameter Pyrex glass outer tube and a 5 cm diameter quartz glass inner tube. Two Lexan spacers at the thruster inlet and exit are used to position the tubes concentrically. A reasonable size for the diameter of the inner glass tube was determined using the dispersion relation, discussed in detail by Chen [17]. The dispersion relation for whistler waves in Eq. 3.30 without damping can be written as follows:

$$\frac{k^2c^2}{\omega^2} = \frac{\omega_p^2}{\omega(\omega_c(k_\parallel/k) - \omega)} \tag{4.1}$$

where c is the speed of light in vacuum, k is the total wavenumber, $k_\parallel$ is the longitudinal wavenumber, ω is the frequency of the wave, ω_p is the plasma frequency, and ω_c is the electron cyclotron frequency. For low frequencies, $\omega \ll 1$, the whistler wave dispersion relation becomes:

$$\frac{k^2c^2}{\omega^2} = \frac{\omega_p^2 k}{\omega\omega_c k_\parallel} \tag{4.2}$$

Solving for k and substituting in the definitions of plasma frequency, ω_p, from Eq. 3.10, and electron cyclotron frequency, ω_c, from Eq. 3.11, gives the wavenumber as a function of the magnetic field, B.

$$k = \frac{\omega}{k_\parallel}\frac{n_0 e}{\epsilon_0 c^2 B} \tag{4.3}$$

If the confined helicon wave is treated like an electromagnetic wave in a cylindrical waveguide, the value of k can be found using Bessel functions, solutions for cylindrical harmonics. The solution for the lowest radial mode in a cylinder of radius a,

in meters, is

$$k_{\perp} \approx \frac{3.83}{a} \tag{4.4}$$

where 3.83 is the first zero of Bessel function J_1. The aspect ratio is defined as

$$G = k_{\perp}\left(\frac{\lambda}{2\pi}\right) = \frac{3.83}{a}\left(\frac{\lambda}{2\pi}\right), \tag{4.5}$$

and is set to $G = 8$, suggested by Chen [17].

To achieve ionization, $\omega/k_{\parallel}$ should be near the velocity of the ionizing electrons, which occurs at the resonant energy, or the maximum ionization cross section. For argon, the resonant energy, $E_r = 50\,\text{eV}$. Using the equation for kinetic energy,

$$\frac{\omega}{k} = \sqrt{\frac{2eE_r}{m_e}} = 4.19x10^6 = \lambda f. \tag{4.6}$$

where λ is the wavelength in m, and f is the frequency in Hz. Substituting into Eq. 4.5 for λ and using the frequency of the RF power supply, 13.56 MHz, the tube radius is 2.4 cm. The actual inner radius of the quartz glass tube is 2.3 cm.

The inner tube has two 5 mm diameter holes positioned at the antenna center and near the thruster exit for the Langmuir probe. The outer tube has corresponding 10 mm holes. The inner tube as a neck for the gas inlet that extends from one end of the tube perpendicular to the tube axis to slow the flow of gas. The glass thruster components and washers are shown in Fig. 4.2.

The helicon thruster resides in a cylindrical vacuum chamber 60 cm wide and 90 cm long. The thruster is supported by an aluminum stand held together with brass screws. Support cradles for the thruster tube that hold the thruster in the center of the magnets are made of brass.

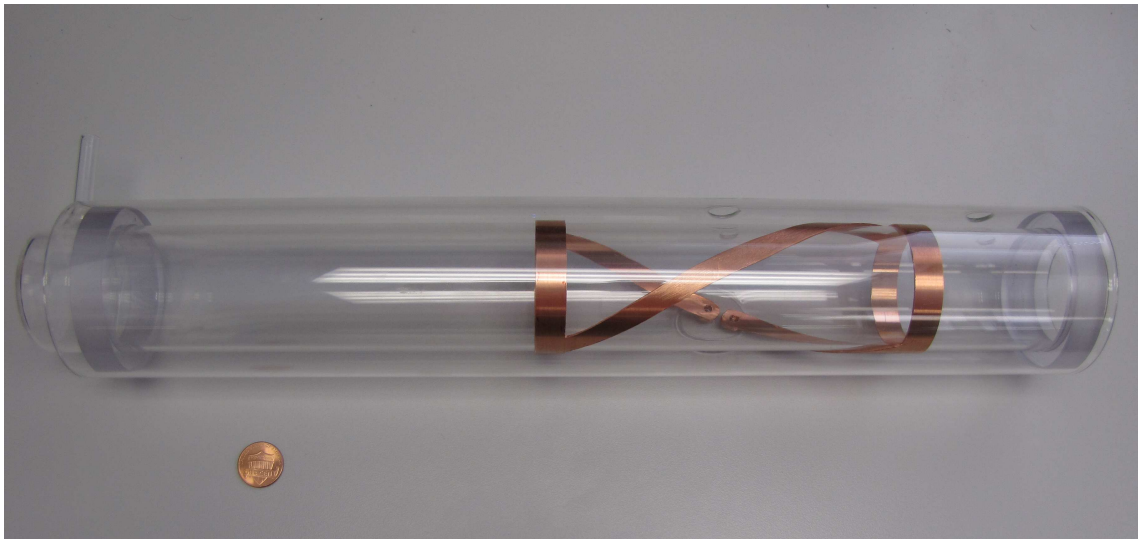

Figure 4.2: Assembled helicon thruster including the outer Pyrex tube, inner quartz glass tube, Lexan washers, and copper antenna.

4.3 Antenna

The antenna is a solid copper single turn helical antenna. The inner diameter is 5 cm and it fits snugly around the inner quartz glass tube of the thruster. The length of the antenna was optimized for argon. The inner radius of the thruster's inner quartz tube, a_{cm}, is 2.3 cm. Using the resonant energy of argon, E_r, and the RF frequency of the antenna power supply, f, the length of the antenna was found using the axial component of the wavenumber.

$$L = \frac{\pi}{k_{\|}} \tag{4.7}$$

where $k_{\|} = 2\pi f/v$. The velocity of the electrons at the resonant energy of 50 eV, v, and an RF frequency, f, of 13.56 MHz yields an antenna length of 15.4 cm.

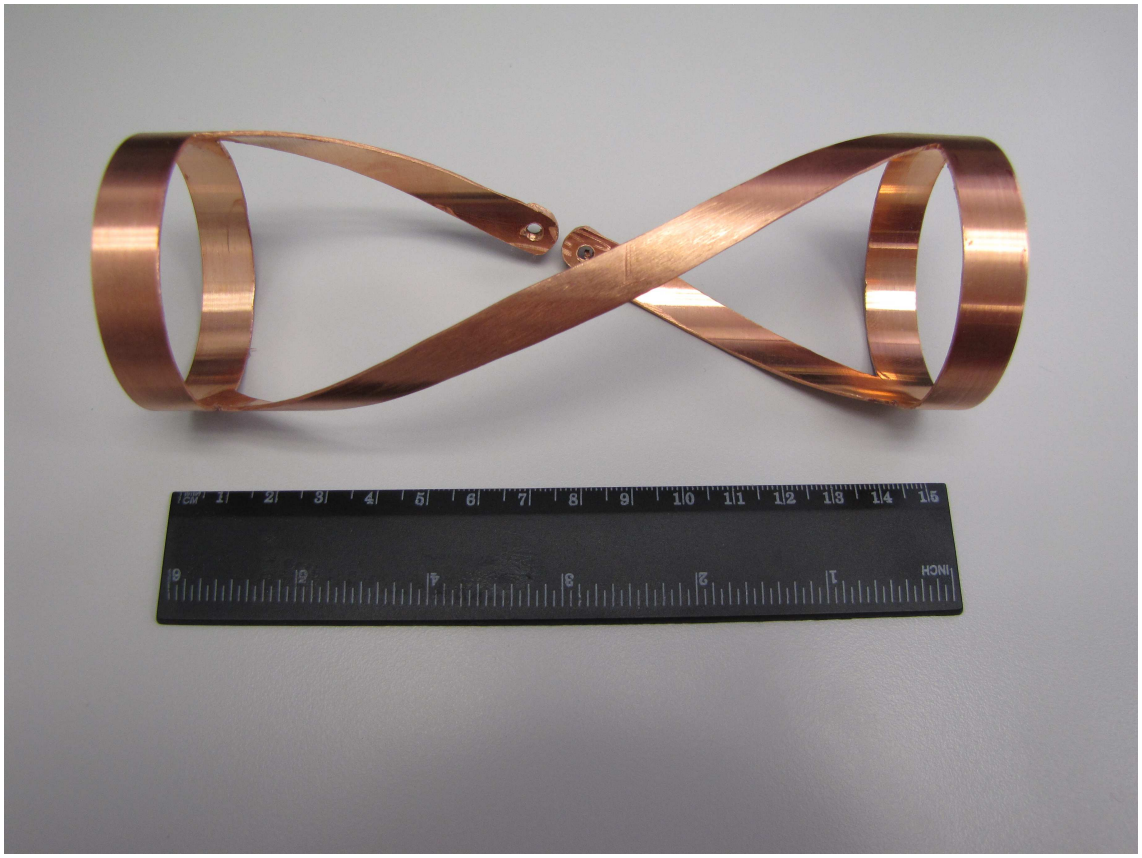

Figure 4.3: 15.4 cm length copper helical antenna.

4.4 Radio Frequency Power System

The helicon thruster antenna is powered by an RF power source operating at 13.56 MHz. An AG 1213W RF Power Source is connected to the thruster antenna via a AIM/ATN Matching Network controlled by a PT-II-CE controller to provide impedance matching. The system is tuned to a 50 Ohm impedance. The RF power supply indicates forward, reverse, requested, and load power. The matching network was tuned manually until the reverse, or power reflected back into the system, reached a minimum. The power reaching the antenna is the forward power, which

is the difference between the requested power and the reverse power. RG 393 coaxial cable connects the matching network to the helicon thruster antenna through a feedthrough at the bottom of the vacuum chamber. The feedthrough fitting that provides the bridge between the air side and the vacuum side is a Kings Electronics KN-99-34 bulkhead adapter. This fitting was used because it has a coaxial connector, a 50 Ohm impedance, and provides an air tight seal into the chamber. It does not have a high heat tolerance, so the input RF power was kept below 200 W.

4.5 Helmholtz Coils

The Helmholtz coils were built in house. The magnet assembly consists of four magnets with an inner radius of 5 cm and an outer radius of 6.2 cm. The magnets are spaced 5 cm apart. Each coil has 20 rows and 20 windings for 400 turns total of 26 gauge square cross section magnet wire with polyimide insulation. The windings are held in a aluminum housing, which is attached to a cooling assembly with clamps made from copper electrical wire and thermal paste to increase the thermal conductivity. Each cooling loop consists of three windings of 1/8 inch outer diameter copper tubing. The cooling loops are soldered to a manifold made from copper tubing. The magnets are cooled in parallel. Swagelok fittings at the ends of the manifold attach to high temperature plastic tubing, which connects to the water feedthrough in the side of the vacuum chamber. The coils are cooled by a cold water source outside the chamber. The Helmholtz coils are powered by two power supplies. The magnet closest to the thruster exit (magnet 1) is powered by a

10 A 30 V power supply. The three magnets upstream of magnet 1 (2, 3, and 4) are powered by a Mastech HY3050 30 A 50 V power supply. Ten Amps of current runs through each magnet coil, resulting in a magnetic field with a maximum strength of 175 G.

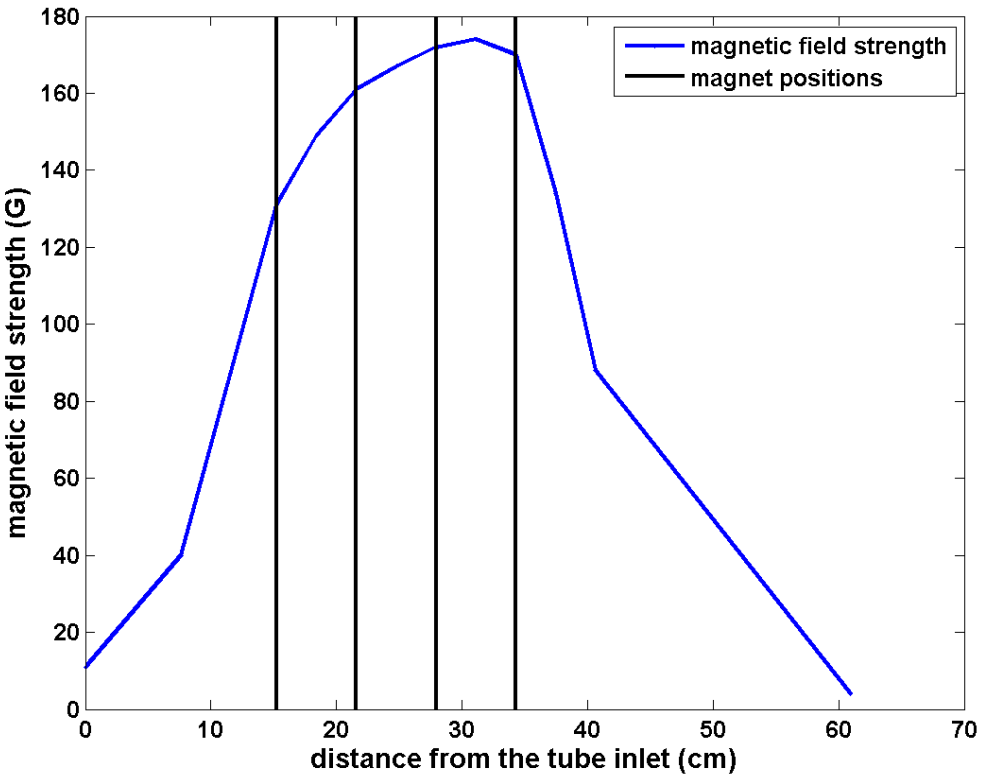

Figure 4.4: Magnetic field strength showing each magnet location. Magnet 4 is the closest magnet coil to the thruster inlet and Magnet 1 is at the thruster exit.

4.6 Gas Feed System

A helium tank, an argon tank, and a bottle of deionized water are connected to the gas feed system and operated independently. The flow of the argon was controlled by a Swagelok SS-3NTRS4 regulating valve downstream of the tank regulator. A second valve further downstream, a Swagelok SS-4BMG-VCR metering valve, allowed for fine adjustment of the main gas flow. The water vapor flow was controlled by only a Swagelok SS-3NTRS4 regulating valve downstream of the sealed bottle. A finer value was not necessary because the water was not pressurized. The helium gas required finer control than the argon or water vapor since smaller amounts had to be added. A CONCOA 560 Series 150 mm flow regulator with a needle valve was used to control the helium gas flow downstream of the helium tank regulator.

4.7 Instrumentation

The diagnostics used in the experiment consist of a single Langmuir probe, a triple Langmuir probe, and a spectrograph for emission spectroscopy. The Langmuir probes contact the plasma directly. The spectroscopy system needs only a line of sight to the plasma.

4.7.1 Single Langmuir Probe

The single Langmuir probe (LP) is an electrode placed in the plasma that can be used to measure current, from which the electron temperature, T_e, and electron

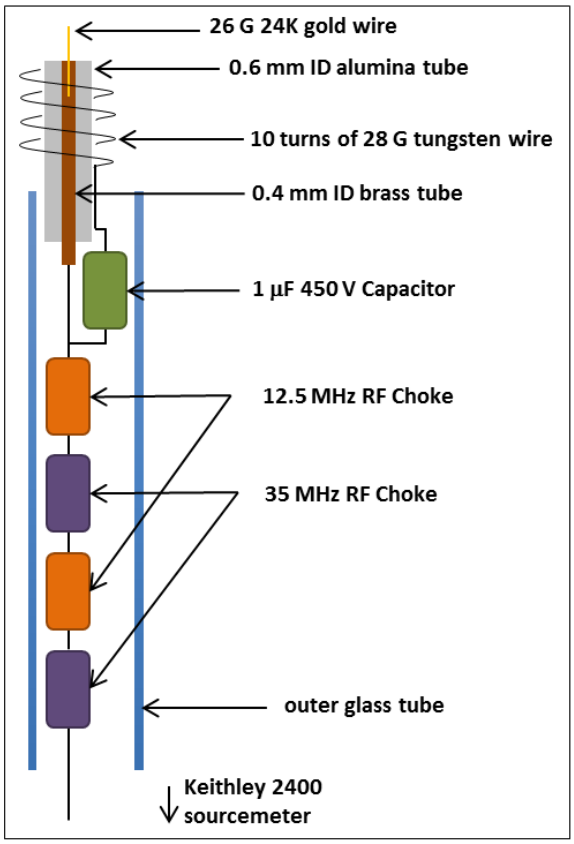

Figure 4.5: Schematic showing the RF compensated single Langmuir probe.

density, n_e, can be determined. Both ion and electron current are collected at the probe tip. For a large negative tip voltage, only ions reach the probe. As the tip voltage is increased, the electron current reaching the probe increases. At the floating potential, V_f, the ion and electron currents are equal and the total probe current is zero. The electron current increases exponentially until the probe voltage reaches the plasma potential, or space potential, V_s.

The LP built for this study was based on an RF compensated probe design by Sudit and Chen [76]. The probe tip and secondary electrode are connected to a 1 μFarrad, 450 V capacitor and four RF chokes in series. The first and third RF

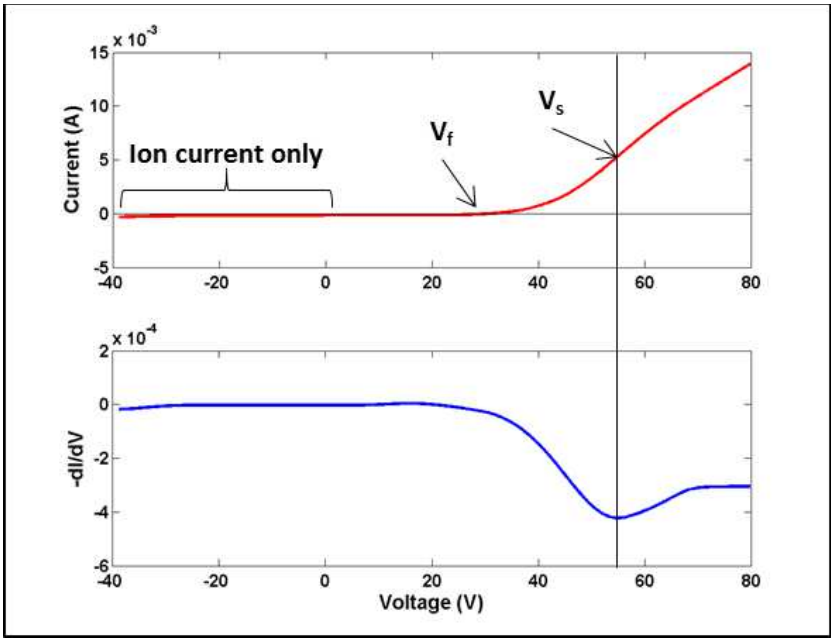

Figure 4.6: An example of a current vs. voltage curve from the single LP showing the zero crossing at the floating potential and the drop in the exponential rise of the current at the space potential. The top plot in red shows the I-V curve. The bottom plot is blue shows the negative derivative.

chokes are 12.5 MHz chokes and the second and fourth are 35 MHz chokes. The capacitor and RF chokes are housed in a glass tube with a 6.35 mm outer diameter. The probe tip is made of 26 gauge 24K gold instead of the suggested graphite or tungsten. It was discovered that the surface properties of the graphite changed because of contamination after only one use, making the current measurements difficult to analyze. The graphite tip was too fragile to withstand multiple cleaning voltage cycles. A tungsten tip was also used, but showed a shift in the data due to contamination of the surface after several tests. Cleaning the tungsten with a large negative voltage resulted in sputtering, which created an opaque film on the inside

of the glass tube. This film interfered with the operation of the spectrograph. The gold tip has shown no significant change in the electron current measurements for repeated tests at identical conditions. The gold tip is held by a brass tube with a 0.4 mm internal diameter and 0.6 mm outer diameter. The brass tube is embedded in an 5 cm long alumina ceramic tube with an outer diameter of 1.6 mm. The brass tube is soldered to the capacitor. A 28 gauge tungsten auxiliary electrode is wrapped around the ceramic tube 10 times and attached to the capacitor with silver solder. The external electrode allows the probe to draw enough current to fill the capacitor and keep $V - V_s$ constant [77]. The surface area of the external electrode must therefore be greater than the probe tip, and is 25 times larger for this probe. The end of the last RF choke is connected to a BNC cable, which is connected to the Keithley 2410 Sourcemeter. The sourcemeter performs the voltage sweep across the LP tip from -40 V to 80 V in 1.2 V steps, for a total of 100 data points. A LabVIEW script controls the sourcemeter and records the current at each voltage step. A schematic of the LP is shown in Fig. 4.5.

Figure 4.6 shows an example of the current-voltage (I-V) curve produced by the tip voltage sweep. The linear section between -40 and 0 V is the region where only ion current is measured by the probe tip. The floating and space potentials are labeled on the red curve on the top of the plot. The zero crossing on the current axis marks V_f. The point where a knee forms in the I-V curve is V_s. This value is easier to determine using the negative of the derivative of the I-V curve, shown in blue on the bottom plot. The minimum of this derivative is V_s, labeled with the vertical black line.

The single LP has some limitations. The knee occurring at V_s disappears for low density plasmas, making T_e very difficult to determine. The probe can also not distinguish between doubly or singly ionized particles, or different species. For example, both electrons and negatively charged OH ions would contribute to the electron current in water vapor plasma, and there is no easy way to distinguish between the two contributions. Because of the low density limitation of the single probe, it is used primarily for calculating n_e.

4.7.2 Triple Langmuir Probe

A triple LP was used in addition to the single LP. This was done to corroborate the results of both probes, but also to get a more accurate measurement of T_e for low density tests. The triple probe is more reliable in low density environments because the analysis does not change based on n_e. The triple probe is also advantageous because it does not require RF compensation. Since the voltage measurement on each of the probe tips is taken simultaneously and no voltage sweep is performed, there is no need to compensate for alternating current. While n_e can be deduced from a triple LP if the current to the circuit created by the probe tips and the plasma is measured, this experiment relies only on the single LP for n_e. The triple LP, diagrammed in Fig. 4.7, is based on a design by Chen and Sekiguchi [78]. It consists of three 0.5 mm diameter tungsten wires embedded in a 4 mm diameter alumina tube with four 0.9 mm diameter axially drilled holes. Three wires are threaded through the alumina tube with 1.5 mm of wire exposed to the plasma at the end

of the alumina. One of the four channels in the alumina is left empty. The probe tip is placed in the plasma in the center of the helical antenna. The location is the same placement as the single LP. Two probe tips are connected to an Acopian A28H800 power supply such that a 42 V bias is placed across them, creating a high potential and low potential tip. The high potential wire is connected to the power supply though a 20 Ω resistor. The remaining tip is left floating. The probe wires are connected to an oscilloscope which measures the voltages. As with the single LP, populations of different species of the same charge cannot be determined, which makes analysis with this diagnostic difficult for molecular plasmas.

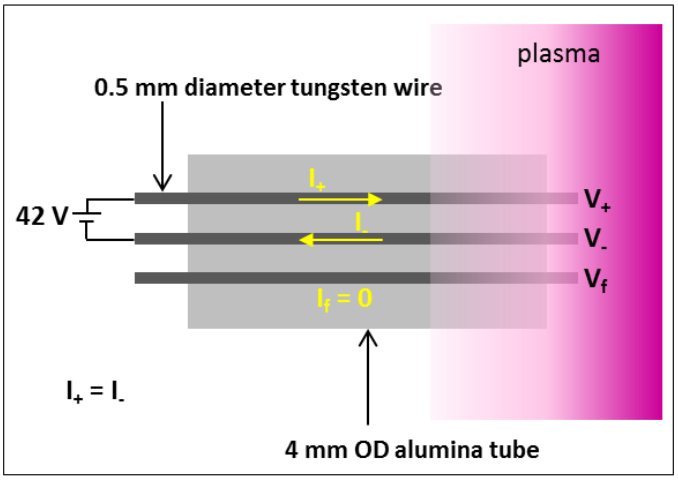

Figure 4.7: Schematic showing the triple Langmuir probe.

4.7.3 Emission Spectroscopy

Spectral data are collected using an Andor Shamrock spectrograph with a Newton CCD camera in conjunction with Andor's SOLIS software. A 600 μm silica

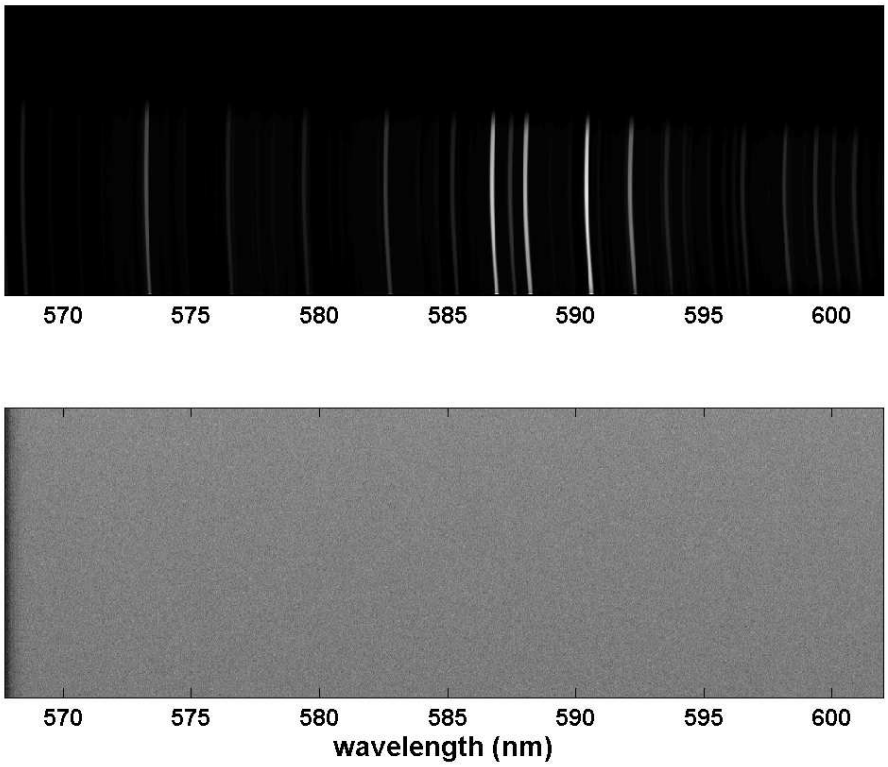

Figure 4.8: An example of a spectrum collected for a mix of argon and helium gas and a background spectrum. The background image brightness has been increased to show the trend at the left edge of the image.

core fiber optic cable passing through a vacuum chamber feedthrough is positioned at the helicon thruster antenna center, outside the outer glass tube. The CCD camera is cooled to -55 C before data collection. Spectra are taken using an 1800 line, 500 nm blaze wavelength grating with a 400-2000 nm filter to remove secondary emission lines from strong argon lines in the near UV spectrum. The spectrograph entrance slit width is 100 μm. After each spectrum is collected, the image is calibrated using a manually generated calibration file for each center wavelength. These files were created using an Ocean Optics argon-mercury calibration lamp. A background

spectrum, or a measurement of a dark chamber, is collected and calibrated for each of the spectrograph measurement conditions each time the CCD camera was powered. The background spectrum is used to remove noise and intensity gradients, like the trend on the left side of the background image shown in Fig. 4.8.

4.8 Experimental Procedure

The following steps were taken to conduct a helicon thruster test and collect data from the three diagnostic tools. The chamber was pumped down to a pressure of $5\text{x}10^{-2}$ mbar. The upper limit of safe operating pressure for the turbo pump is $1\text{x}10^{-1}$ mbar. The turbo pump was powered on and run for at least two hours so the base pressure reached $9\text{x}10^{-5}$ mbar. The main propellant gas is added until the desired pressure is reached. To ignite the thruster, the RF power supply is turned on and slowly increased until the forward power is 100 W. The amount of gas is adjusted back to the desired pressure. The system is left for a minimum of eight minutes to reach thermal equilibrium. It was discovered that test repeatability was difficult to achieve until the antenna reached its maximum temperature. Once the antenna heating equalized, the magnets were powered with a 10 A current through all coils. The magnet current drops as the magnets heat up and their resistance changes, but reaching equilibrium takes less than one minute. The gas pressure and magnet current were given a final adjustment once the system reached thermal equilibrium. If the test required helium seed gas, it was added after the system equalized. The thruster is monitored through a view port on the side of the vacuum

chamber using a video camera. After the thruster has been powered and reached the desired pressure, gas mixture, power, and magnetic field strength, the port is covered so that ambient light does not reach the spectrograph fiber optic cable. One LP test is collected for each run, then one spectrograph series is collected. Five windows of wavelength ranges in the visible spectrum are collected, centered at the following wavelengths: 460.00, 500.00, 587.56, 667.82, and 718.00 nm. The nine helium emission lines measured are 447.1, 471.3, 492.2, 501.6, 504.8, 587.6, 667.8, 706.5, and 728.1 nm. The exposure time varied depending on the main propellant. The thruster RF power and magnets are then powered down so that the chamber is completely dark. The spectrograph series is collected again to acquire a background spectrum for each of the five wavelength windows.

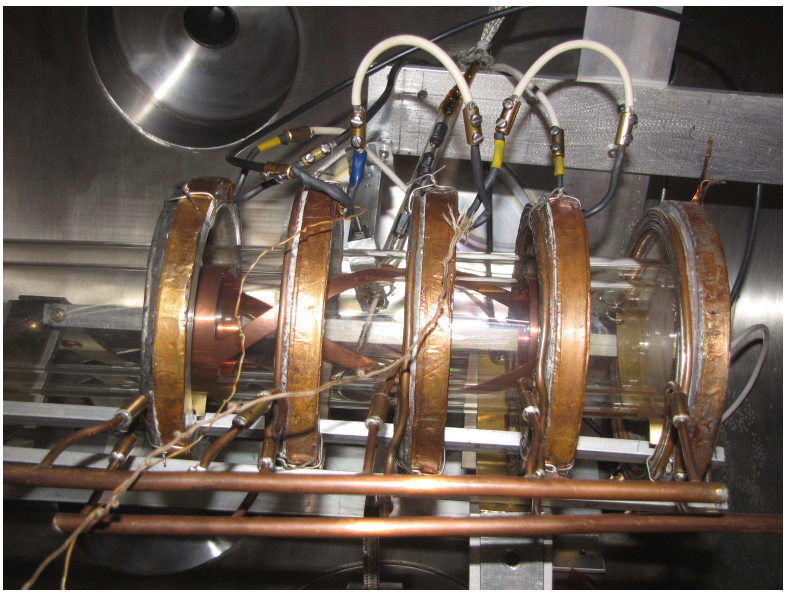

Figure 4.9: The complete experimental setup inside the vacuum chamber showing the glass tubes, antenna, Helmholtz coils with copper cooling manifold, RF power cable, single LP, and spectrograph fiber optic cable mount.

Chapter 5: Data Analysis

This chapter discusses how measurements from the single Langmuir probe and triple Langmuir probe are used to calculate the plasma parameters, electron density and electron temperature. The method for acquiring helium emission line ratios from spectroscopic measurements is also described.

5.1 Single Langmuir Probe Data Analysis

The single LP measures current as a function of probe voltage and is used to determine n_e, and in some cases, T_e of the plasma in the thruster. The voltage on the probe tip was swept from -40 V to 80 V and the current to the tip was recorded for each voltage step, resulting in a current-voltage (I-V) curve such as the one shown in Fig. 4.6. One sweep was conducted for each test. Ten runs of at each test condition were conducted and the current measurements were averaged to reduce noise in the I-V curve. The floating potential, V_f, was determined by the zero crossing of the I-V curve. The space potential, V_s, was determined by locating the minimum of the negative derivative of the I-V curve ($-dI/dV$) Both V_f and V_s are labeled on Fig. 4.6.

Orbital Motion Limited (OML) theory was used to find T_e and n_e from the

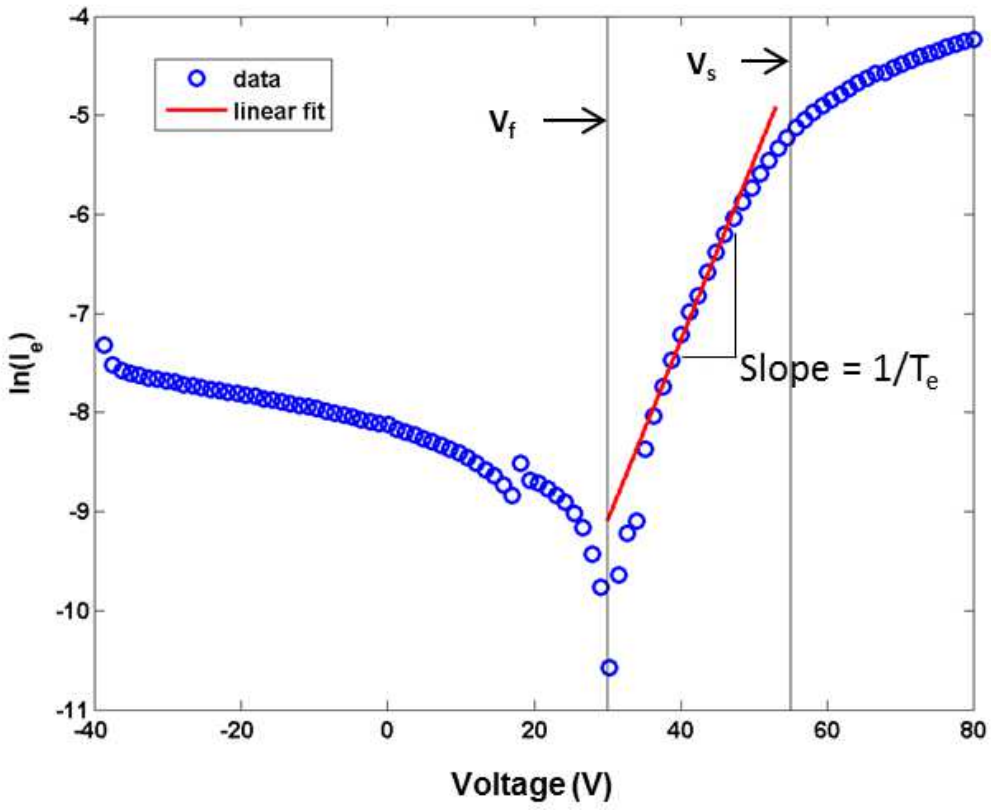

Figure 5.1: The natural log of the I_e measurements is plotted for each voltage step, shown by the blue circles. The red line shows the linear fit between V_f and V_s. T_e is found from the reciprocal of the slope.

single probe sweep. This theory is valid if the probe radius is larger than the Debye length [79]. The Debye length, given by Eq. 3.28, is on the order of 0.01 mm in the thruster. The Langmuir probe radius is 0.2 mm. For cylindrical probes, the ion current, I_i, can be found by fitting a line to the flat section of the I-V curve at large negative voltages. The square of the ion current is directly proportional to the probe voltage, V.

$$I_i^2 = A_p n_e e \frac{\sqrt{2}}{\pi} \left(\frac{e(V_{s1} - V)}{m_i} \right) \tag{5.1}$$

The probe area is A_p, e is the elementary charge, m_i is the ion mass, and V_{s1} is a shifted space potential used for the line fit, not the actual plasma space potential. The slope of this linear fit, S, can be used to find n_e.

$$n_e = \sqrt{\frac{S\pi^2 m_i}{-2e^3 A_p^2}} \tag{5.2}$$

The electron temperature can be found using V_f and V_s, however, V_s can be difficult to determine in plasmas with $n_e \lesssim 10^{16}\,\mathrm{m}^{-3}$, making the single LP an unreliable diagnostic for finding T_e in low density tests. Electron temperature can be calculated from the electron current, I_e, found by subtracting the ion current from the total current. Assuming Maxwellian electrons, $1/T_e$ is proportional to the natural log of I_e between V_f and V_s [77].

$$f(v) \propto \exp - \left(\frac{\frac{1}{2} m_e v^2 + eV}{kT_e} \right) \tag{5.3}$$

Figure 5.1 shows the region of the $\ln(I_e)$ plot between V_f and V_s. The region is not quite linear near the V_f and V_s limits, which introduces error into the T_e measurement. For this reason and the inability to ascertain V_s for low density data, the single LP is primarily used to calculate n_e.

5.2 Triple Langmuir Probe Analysis

The triple LP takes a simultaneous measurement of voltage on all three probe tips and is not affected by a low density plasma environment, so this probe was used to get a more accurate measure of T_e. Determining T_e from the voltage on the triple probe tips depends on several assumptions: the electron energy distribution

is Maxwellian, the electron mean free path is larger than the probe wire radius and the ion sheath thickness, and the separation between the wires is larger than the sheath thickness. The current in each of the wires connected to the power supply, I_+ and I_-, as well as the current in the floating wire, I_f, can be expressed as a function of the electron and ion current densities, and the probe tip area, which is the same for all three tips.

$$I_+ = Aen_e\sqrt{\frac{kT_e}{2\pi m_e}}\exp\left(\frac{-eV_+}{kT_e}\right) - AJ_i \tag{5.4}$$

$$I_{-,f} = -Aen_e\sqrt{\frac{kT_e}{2\pi m_e}}\exp\left(\frac{-eV_{-,f}}{kT_e}\right) + AJ_i \tag{5.5}$$

The ion current density is J_i, and the probe tip area is A. The voltage measured on the higher potential wire is V_+, the voltage on the lower potential wire is V_-, and the voltage on the floating tip is V_f. Adding I_- and I_f to I_+ to eliminate the J_i term, then taking the ratio of the sums yields an expression that can be used to calculate T_e. In this triple probe configuration, $I_f = 0$, and $I_+ = I_-$, so the sum ratio is equal to 1/2.

$$\frac{I_+ + I_f}{I_+ + I_-} = \frac{1 - \exp\left[\frac{-e(V_+ - V_f)}{kT_e}\right]}{1 - \exp\left[\frac{-e(V_+ - V_-)}{kT_e}\right]} = \frac{1}{2} \tag{5.6}$$

This equation can be solved for T_e from the direct measurements of the voltages on the three probe tips. The triple LP measures only T_e. The n_e measurement comes from the single LP.

5.3 Spectrograph Data Analysis

5.3.1 Processing Raw Spectra

Ten spectra were collected for each test. Two images, one of the lit plasma and one with a dark chamber, were recorded with center wavelengths of 460.00, 500.00, 587.56, 667.82, and 718.00 nm. Spectra are images 1024 x 256 pixels in size. The dark background image was subtracted from the data image to remove noise and gradients. The intensity of this new image was corrected using the efficiency curve for the 1800 line grating, shown in Fig. 5.2. The grating efficiency is a function of the wavelength and is a measure of the percentage of light that is transmitted to the spectrograph.

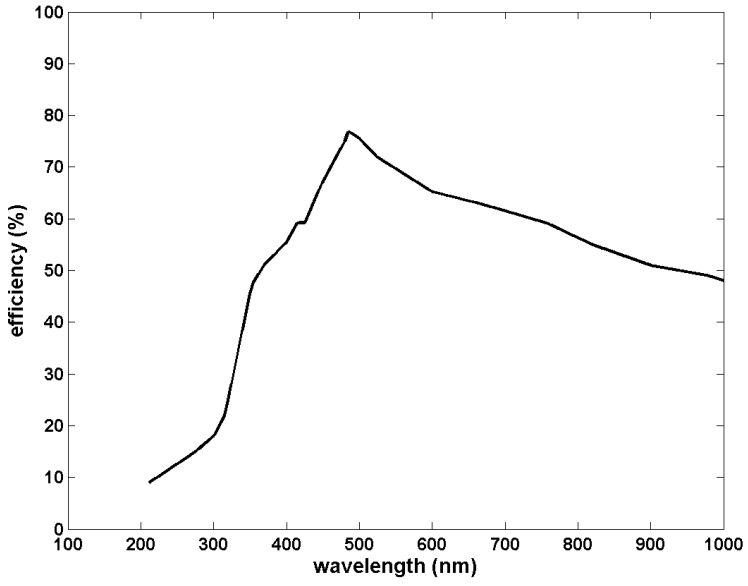

Figure 5.2: The transmission efficiency of the 1800 line, 500 nm blaze wavelength grating as a function of wavelength.

To remove emission line distortion from the fiber optic cable and entrance slit in the full image, a swath 50 pixels wide was selected from the center of the image where the emission line intensity is the strongest. This selection window was averaged along the vertical axis to get a single 1024 element array of intensity as a function of wavelength. Figure 5.3 indicates the selection window for a spectral image.

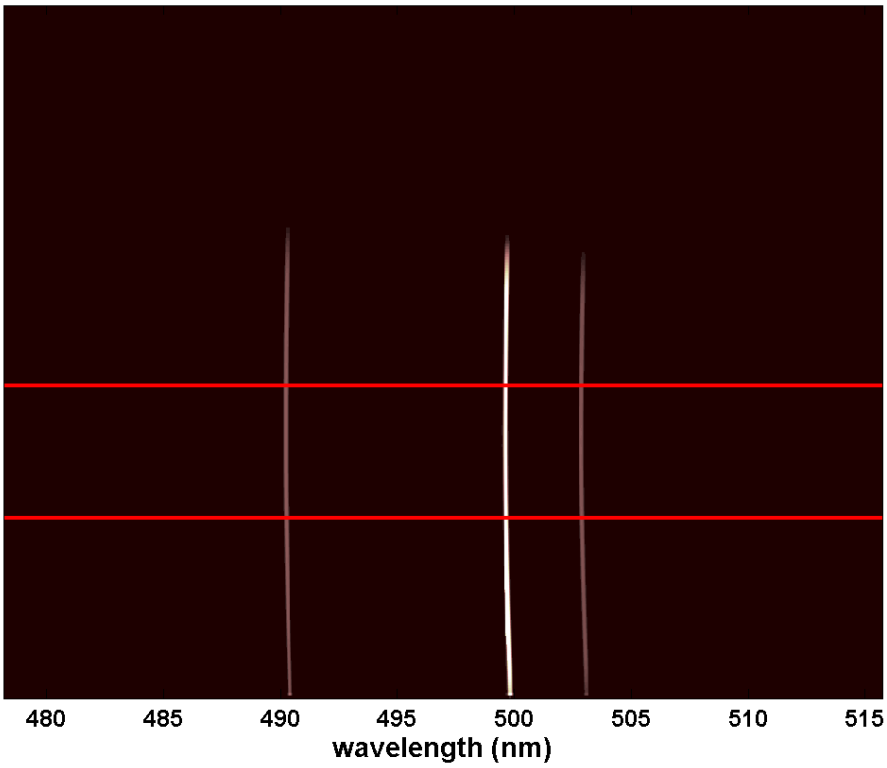

Figure 5.3: Helium spectrum image showing averaged 50 pixel wide window marked by the area between the red lines.

This array had a vertical shift, meaning the dark space between emission lines had a low but non-zero intensity value. To eliminate this shift, a 10,000 bin

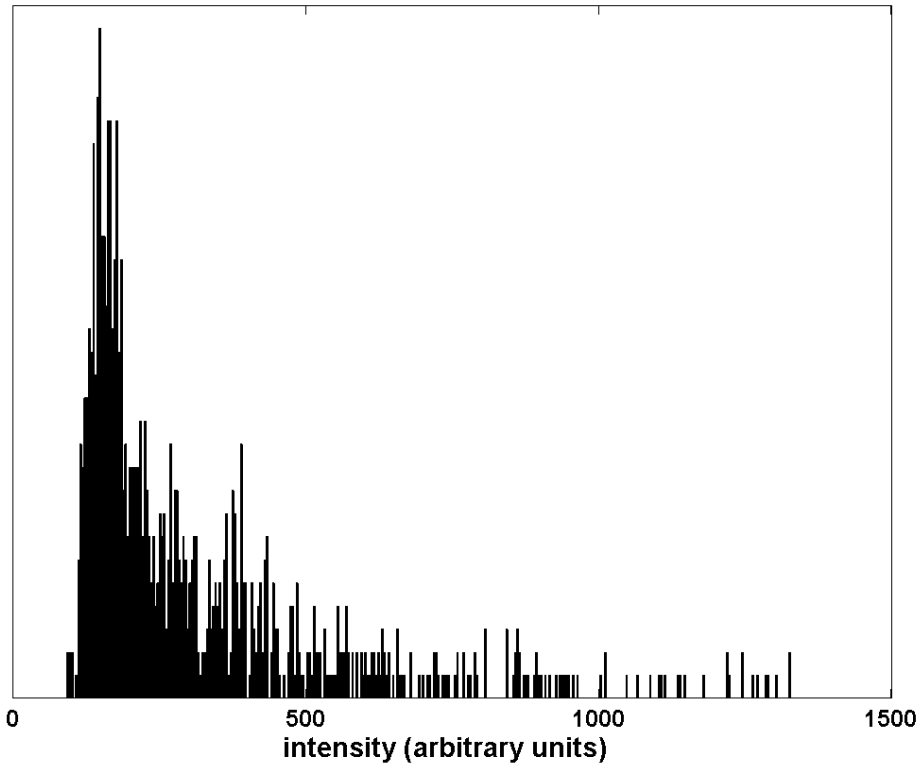

Figure 5.4: Example of a histogram plot used to find the value of the intensity shift. The high population at 149 indicates that this value should be subtracted from the intensity array to zero the spectrum.

histogram of the data was generated to find the bin with the maximum value and its corresponding intensity. An example of an intensity histogram is shown in Fig. 5.4. The non-zero value bin with the highest population indicates the value that had to be subtracted from the original array to zero the intensity shift.

5.3.2 Calculating Line Ratios

Once the spectrum was processed, the intensities of the peaks that correspond to the eight helium emission lines were calculated. An example of the processed

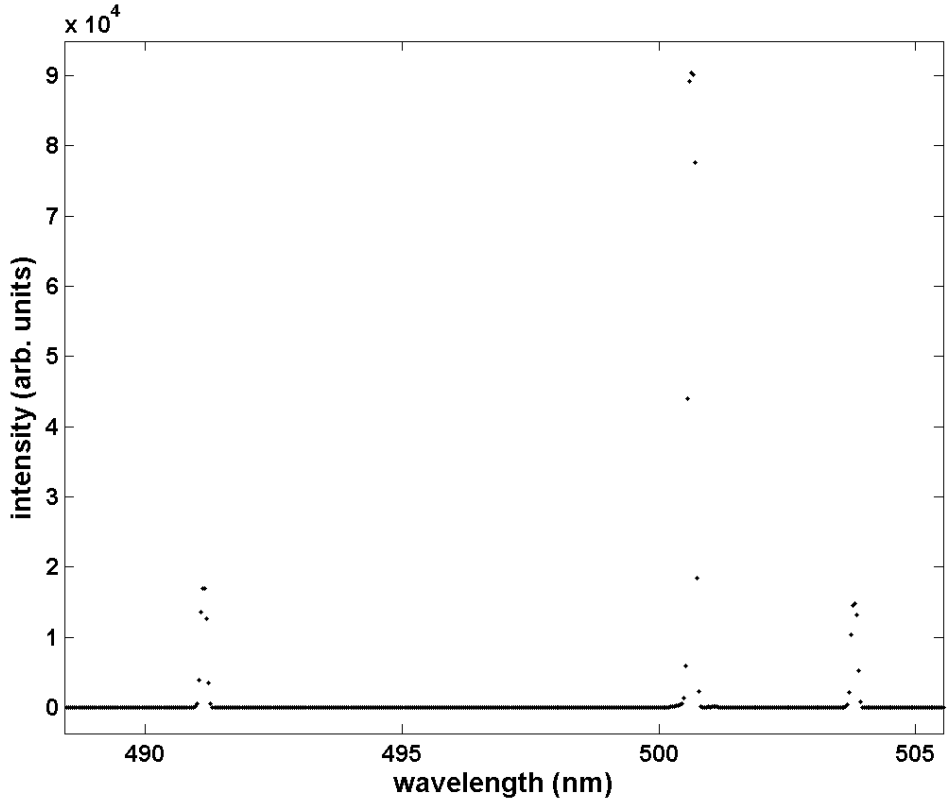

Figure 5.5: Example of measured helium emission lines after processing. This window shows the lines at 492.2, 501.6, and 504.8 nm.

spectrum from a pure helium test is shown in Fig. 5.5. Emission lines from the pure helium and water vapor/helium mixed gas tests were unobscured and required no further steps before finding the line intensities. The argon/helium mixed gas tests needed an additional step to obtain a spectrum with clearly visible helium lines. Several argon emission lines partially obscure helium lines, so each spectrum collected for the mixed gas had the corresponding spectrum for pure argon gas subtracted from it to reveal only the helium lines. Figure 5.6 shows an example of the the helium spectrum resulting from the subtraction of a pure argon test from

an argon/helium mix test. In this example, the 504.8 nm line is partially obscured by an argon line. Both the argon/helium mixed gas and pure argon gas tests were conducted at the same conditions, making it possible to eliminate the argon lines. A window between 14 and 30 pixels wide was selected around the chosen helium line, and a Gaussian curve was fit to the data points within the window using a peak fitting MATLAB program [80]. Figure 5.7 shows an example of a Gaussian fit for intensity data from a 728.1 nm wavelength emission line. The height of this Gaussian fit is the peak intensity of the given wavelength. The line ratios are calculated using these intensity values for all eight wavelengths. These ratios are compared to the line ratios calculated by the helium CRM.

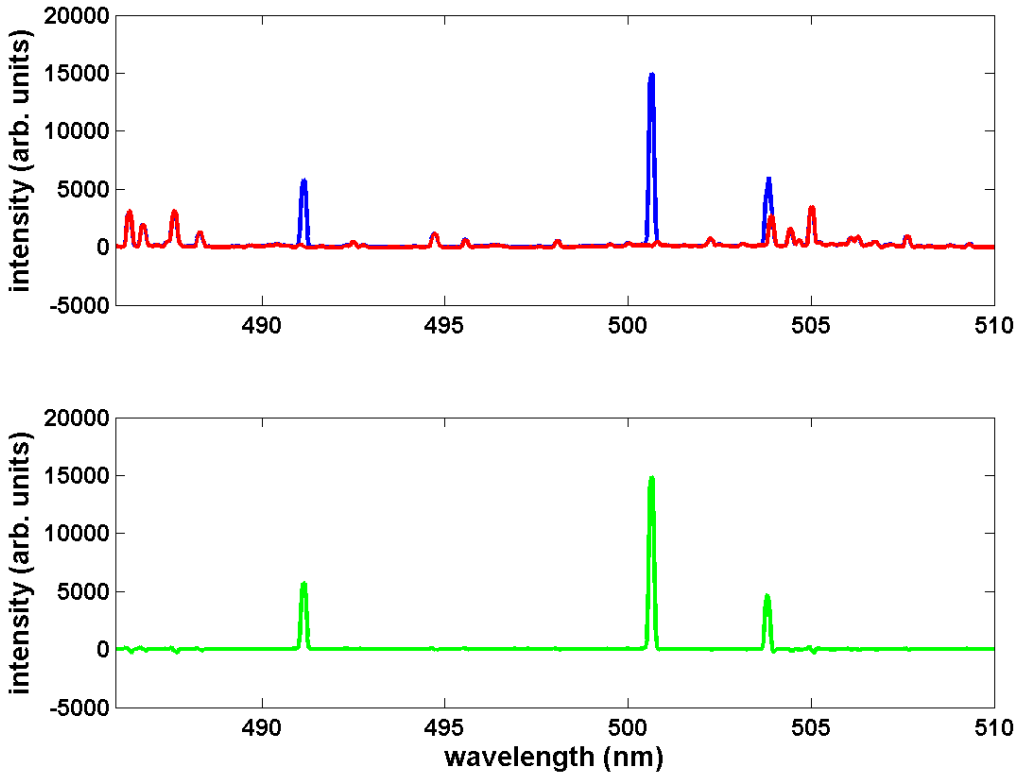

Figure 5.6: Example of a helium only spectrum, shown in green, achieved by subtracting a pure argon spectrum, shown in red, from an argon/helium mixed gas spectrum, shown in blue. The argon and argon/helium mixed gas tests were conducted at the same test conditions.

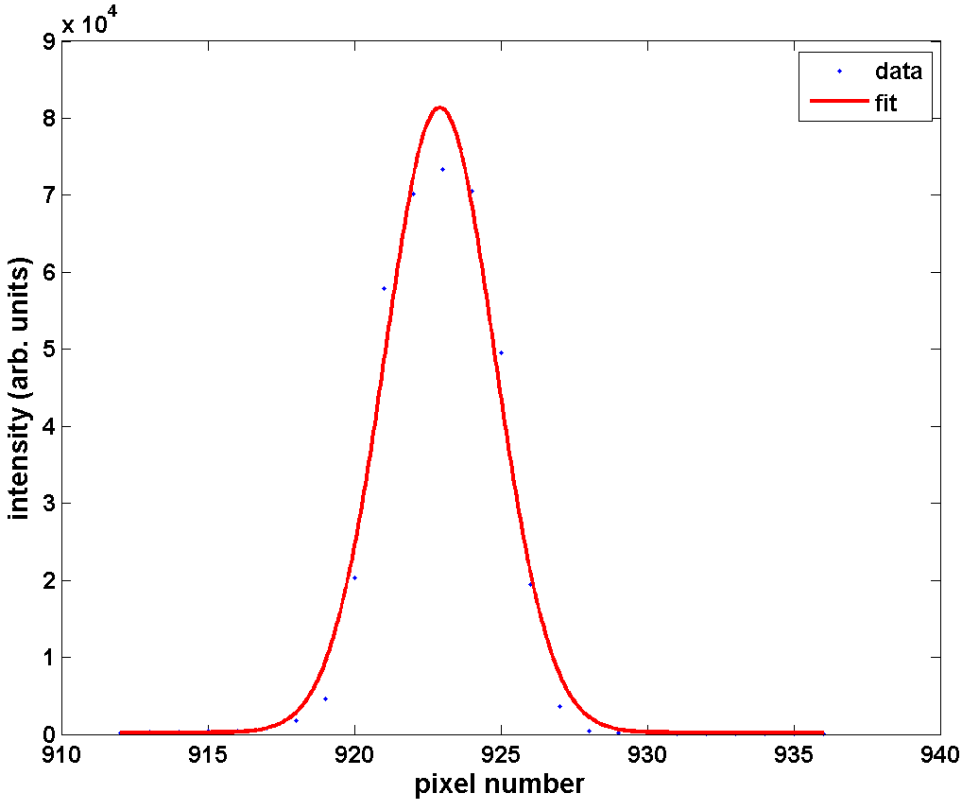

Figure 5.7: Example of a Gaussian peak fit for the 728.1 nm wavelength. The blue dots represent the spectrograph intensity measurements. The red line is the curve best fit to the data.

Chapter 6: Helium Constant Ground State Collisional Radiative Model

The emission spectroscopy analysis is accomplished using a constant ground state collisional radiative model (CGS-CRM) for helium. This is a computer model that predicts emission line intensity at certain wavelengths for a given electron temperature, T_e, and electron density, n_e. Emission line intensity is dependent on the number density of helium atoms in the particular energy state that contributes to the line. The density of atoms in excited states can be calculated by finding the rates at which states are populated and depopulated by excitation and de-excitation processes. Because neutral gas in the ground state is constantly flowing into the thruster from the tank, the ground state population is treated as a constant quantity.

6.1 CGS-CRM Energy Levels

The CGS-CRM models 72 total energy states from quantum numbers, $1 \leq n \leq 15$. The energy states listed for neutral helium, He I, in the National Institute of Standards and Technology (NIST) Atomic Spectra Database were consolidated to get the abbreviated list of energy states used the CGS-CRM [81]. The n^3P states for $2 \leq n \leq 10$, n^3D states for $3 \leq n \leq 10$, and n^3F states for $4 \leq n \leq 10$ have been approxi-

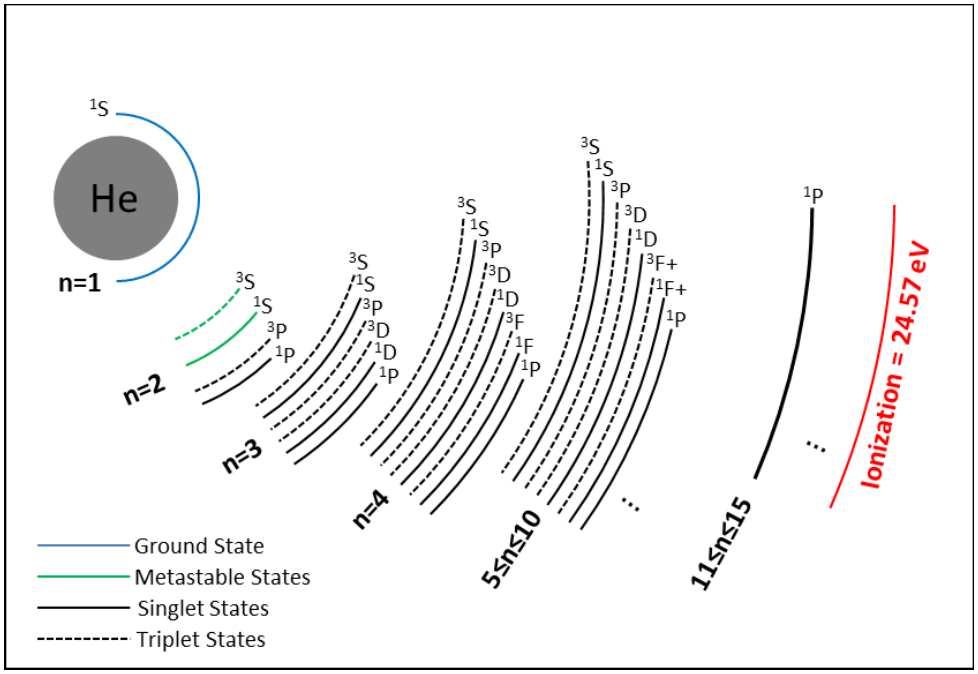

Figure 6.1: Helium energy states included in the CGS-CRM. The ground state is shown in blue. The metastable states are shown in green. The singlet states are shown with solid lines. The triplet states are shown with dashed lines.

mated as a single energy state. Angular momentum states higher than F for 5≤n≤10 are all considered degenerate and have been condensed into a single $F+$ state. All energy states with quantum numbers 11≤n≤15 are treated as if the helium atom behaves like a hydrogen atom and only the n^1P state is considered. All ions are assumed to be in their ground state. Figure 6.1 shows a diagram of the He I energy states modeled. The solid lines on the diagram show the singlet states and the dotted lines show the triplet states. Singlet-triplet ratios are more sensitive to changes in electron temperature while singlet-singlet ratios are more sensitive to changes in electron density. This energy state consolidation scheme is similar to that used in

the helium CRM presented by Goto, with the inclusion of all angular momentum sub-states for n=8,9, and 10 [71]. Table A.1 lists all the energy states.

6.2 Modeled Transitions

The population densities in each of the 71 excited neutral helium states is determined by modeling transitions between states, the rates of which depend on T_e and n_e. There are a number of transitions that can occur between excited states of helium neutrals or between helium neutrals and helium ions. Depending on the assumptions made about the plasma, these some of these transitions may be negligible. Several assumptions are made in the CGS-CRM to reduce the complexity of the model. All ions are considered to be in a single energy state, the ion ground state; only singly ionized particles are allowed; and heavy particles are considered to be stationary compared to the electrons. The following transitions are included in the CGS-CRM: electron induced excitation, electron induced de-excitation, spontaneous radiative de-excitation, electron induced ionization, photo-excitation, radiative ion-electron recombination, three-body recombination, and metastable diffusion to the tube walls. Stimulated recombination and photo-ionization are neglected because the plasma can be considered optically thin for these interactions. The optical thickness is not uniform across the plasma. It is dependent on the energy state of the absorbing particle and the optically thin plasma assumption is not true for some transitions, which are included as photo-excitation transitions. Atom-atom collisions, and atom-ion collisions are neglected because the heavy particles are assumed

to be stationary. Dielectronic radiation is a two-step process by which an electron is captured by an ion, causing a bound electron to temporarily jump to a doubly excited state in the newly neutralized particle. The interaction then results in a neutralized particle in a lower energy state and the release of a photon. Its inverse process is autoionization, where an unstable neutral state decomposes into an ion and a free electron. Both of these processes are neglected because T_e is low relative to the ionization energy, therefore the population of highly excited, or less stable, states is low. These transitions are less likely to occur in particles with only one or two bound electrons, like helium.

6.2.1 Calculation of Collision Rates

The collision rates are the product of the collision cross section and the electron velocity, shown in Eq. 6.1. The cross sections for electron induced excitation, de-excitation, and ionization can be found in a number of sources. The data used in this model come from Ralchenko's cross section fits, originally published in 2000 and updated in 2008 [82, 83]. The plot in Fig. 6.2 shows an example of the excitation cross section as a function of electron energy, E_e.

The collision rate for a transition from state i to state j, is given by

$$C_{ij} = \langle \sigma_{ij} v \rangle = \int_0^\infty \sigma_{ij} f_e(E_e) \sqrt{\frac{2E_e}{m_e}} \mathrm{d}E_e \tag{6.1}$$

where σ_{ij} is the collisional cross section in m^2 for the transition from state i to state j, E_e is the electron energy in J, m_e is the electron mass in kg, and f_e is the energy distribution. Assuming the plasma is Maxwellian, f_e is given by Eq. 6.2, which has

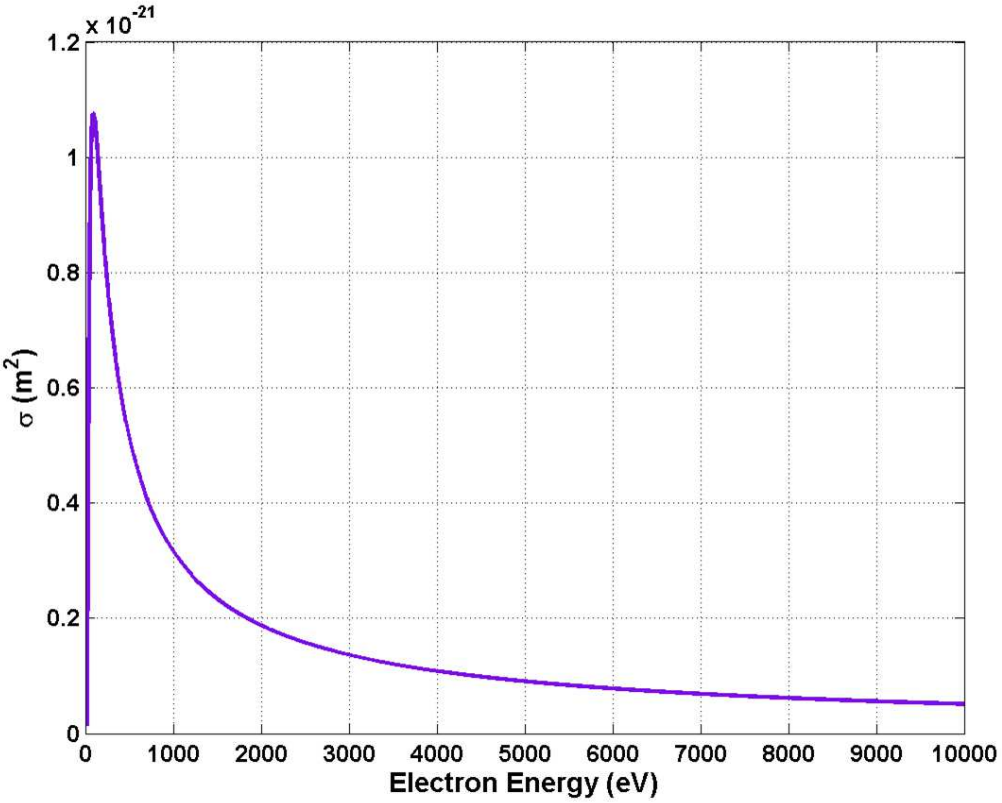

Figure 6.2: Electron collisional excitation cross section as a function of electron energy for excitation from the He I ground state to 2^1P.

a T_e dependence.

$$f_e(E_e) = \frac{2}{\sqrt{\pi}} \sqrt{\frac{E_e}{(q_e T_e)^3}} \exp\left(-\frac{E_e}{T_e}\right) \tag{6.2}$$

The rate calculations and the accuracy of the CGS-CRM are heavily dependent on the accuracy of the collision cross section data.

6.2.2 Electron Induced Excitation

Electron induced excitation occurs when an electron impacts a neutral particle and causes a bound electron in the outer shell jump from state i to a higher energy

state, j. The charge of the heavy particle does not change and the impacting electron remains free.

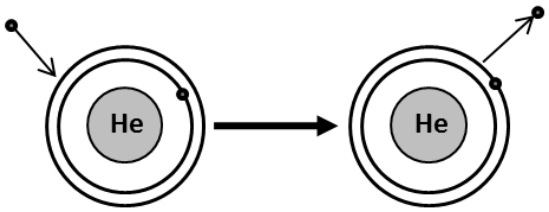

Figure 6.3: Electron induced excitation.

Collisional cross section data as a function of electron temperature for all energy states with $1 \leq n \leq 4$ were computed from tables of fit coefficients published by Ralchenko [83]. There are 2556 possible combinations of lower energy state i and upper energy state j using the 72 energy states, but only 810 are modeled. Transitions from $1 \leq n_i \leq 3$ to $n_j \geq 5$ are found by scaling the cross sections for the transition from the n_i state to the n=4 state with the same angular momentum, L, and spin, S, as follows,

$$\sigma_{n_i^{2S_i+1}L_i \rightarrow n_j^{2S_j+1}L_j}(E_e) = \left(\frac{4}{n_j}\right)^3 \sigma_{n_i^{2S_i+1}L_i \rightarrow 4^{2S_j+1}L_j}(E_e/\epsilon) \tag{6.3}$$

where ϵ is E_{ij}/E_{i4}, the ratio of the energy difference between states i and j to the energy difference between states i and the state in shell n=4 with the same angular momentum and spin as j.

Higher energy transitions from $n_i \geq 4$ to $n_j \geq 5$ are calculated using the hydrogenic approximation. The collisional cross section depends on the electron energy,

E_e, and the difference in energy between state i and state j, E_{ij}.

$$\sigma(E_e, E_{ij}) = \pi a_0^2 \left(\frac{Ry}{g_i E_e}\right) \Omega \left(\frac{E_e}{E_{ij}}\right) \tag{6.4}$$

where a_0 is the Bohr radius in m^2, Ry is the Rydberg energy in eV, g_i is the degeneracy of state i, and Ω is the collision strength. The collision strength is a function of the electron temperature and is found using tabulated fit coefficients based on the type of transition. Excitation transitions are classified by three types: dipole allowed, dipole forbidden, and spin forbidden.

6.2.2.1 Dipole Allowed Transitions

The transition types were determined using the selection rules [82]. A dipole allowed transition is a transition to an adjacent angular momentum state (ΔL=$\pm$1), regardless of quantum number, with no change in spin (ΔS=0). The equation for collision strength as a function of $x = E_e/E_{ij}$ is given by

$$\Omega(x) = \left(A_1 \ln(x) + A_2 + \frac{A_3}{x} + \frac{A_4}{x^2} + \frac{A_5}{x^3}\right) \times \left(\frac{x+1}{x+A_6}\right) \tag{6.5}$$

where A_n are the fitting coefficients. These coefficients are listed in table C.1. In scaling the collisional cross sections for transitions from $n_i \leq 3$ to $n_j \geq 5$ for dipole allowed transitions only, the scaling factor $(4/n_j)^3$ is replaced by the ratio of the oscillator strengths $(f_{n_i L_i; n_j L_j}/f_{n_i L_i; 4 L_j})$ when $(n_j\text{-}n_i) \leq 4$.

6.2.2.2 Dipole Forbidden Transitions

Forbidden transitions encompass any transition that does not obey the selection rule for the dipole allowed transitions. These transitions have a lower probabil-

ity of occurrence than allowed transitions. A dipole forbidden transition is a transition to a non-adjacent angular momentum state ($\Delta L \neq \pm 1$), regardless of quantum number, with no change in spin. The collision strength for these transitions is given by

$$\Omega(x) = \left(A_1 + \frac{A_2}{x} + \frac{A_3}{x^2} + \frac{A_4}{x^3} \right) \times \left(\frac{x^2}{x^2 + A_5} \right) \tag{6.6}$$

The fit coefficients for dipole forbidden transitions are listed in table C.2.

6.2.2.3 Spin Forbidden Transitions

A spin forbidden transition is any transition with a change in spin ($\Delta S \neq 0$) and have the lowest rate of occurrence. The following gives the collision strength for spin forbidden transitions:

$$\Omega(x) = \left(A_1 + \frac{A_2}{x} + \frac{A_3}{x^2} + \frac{A_4}{x^3} \right) \times \left(\frac{1}{x^2 + A_5} \right) \tag{6.7}$$

The spin forbidden fit coefficients are listed in table C.3.

6.2.2.4 Hydrogenic Approximation for Excitation to Higher Energy Levels

Collisional cross sections for excitation between energy states with $n_i \geq 4$ and $n_j \geq 5$ are approximated using the hydrogenic approximation. Only transitions from $n_i^1 S$ to $n_j^1 P$ are modeled where $4 \leq n_i \leq 10$ and $5 \leq n_j \leq 15$. The collisional cross section is given by

$$\sigma_{n_i \to n_j} = 4\pi a_0^2 \left(\frac{Ry}{E_{ij}} \right)^2 f_{n_i n_j} F(x) \tag{6.8}$$

where

$$F(x) = \frac{1}{x}[1 - \exp(-\xi(x+1)) \ln(x+0.2)], \tag{6.9}$$

$$\xi = \frac{1}{2}\left(f_{n_i n_j}\frac{Ry}{E_{ij}}\right)^{-0.7}, \tag{6.10}$$

and

$$x = \frac{E_e}{E_{ij}} \tag{6.11}$$

The oscillator strength, $f_{n_i n_j}$, is given by the following [84]:

$$f_{n_i n_j} = \frac{32}{3\sqrt{3}\pi}\left(\frac{n_i}{n_j^3}\right) z^{-3} g(n_i, z) \tag{6.12}$$

where

$$z = \frac{E_{ij}}{(E_{He_{ion}} - E_i)}, \tag{6.13}$$

the ratio of the energy difference between the states and the difference between the ionization energy of helium and the energy of the lower state. The quantity $g(n_i, z)$ is a correction factor approximated by

$$g(n_i, z) = g_0(n_i) + \frac{g_1(n_i)}{z} + \frac{g_2(n_i)}{z^2} \tag{6.14}$$

where g_0, g_1, and g_2 are constants that depend on the value of n_i. For $n_i \geq 3$,

$$g_0(n_i) = 0.9935 + \frac{0.2328}{n_i} - \frac{0.1296}{n_i^2} \tag{6.15}$$

$$g_1(n_i) = \frac{-1}{n_i}(0.6282 - \frac{0.5598}{n_i} + \frac{0.5299}{n_i^2}) \tag{6.16}$$

$$g_2(n_i) = \frac{1}{n_i^2}(0.3887 - \frac{1.181}{n_i} + \frac{1.470}{n_i^2}) \tag{6.17}$$

Figure 6.5 shows the log of the values of electron collision excitation rates, $\log(C_{ij})$, for $T_e = 10\,\text{eV}$. The image is a 72×72 matrix showing the rate of excitation from level i to level j in the upper triangle.

6.2.3 Electron Induced De-excitation

Electron induced de-excitation occurs when an electron collides with a neutral atom in an excited state and causes a bound electron to drop from level j to level i. The impacting electron remains free.

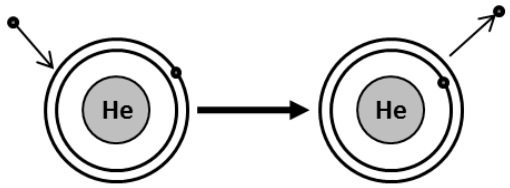

Figure 6.4: Electron induced de-excitation.

This is the inverse process of electron induced excitation. In equilibrium, the de-excitation rate is equal to the excitation rate. The change in number density between states i and j over time is equal to the difference between the rate of excitation transitions from i to j and the rate of de-excitation collisions from j to i:

$$\frac{\mathrm{d}n_{ij}}{\mathrm{d}t} = n_i n_e C_{ij} - n_j n_e C_{ji} \tag{6.18}$$

where n_i and n_j are the densities of states i and j, and n_e is the electron density. In steady state, $dn_{ij}/dt = 0$, leading to the following relationship between the rate of excitation, C_{ij}, and the rate of de-excitation, C_{ji}:

$$C_{ji} = \frac{n_i}{n_j} C_{ij} \tag{6.19}$$

The following statement is true for gases in thermodynamic equilibrium [85]. The ratio of the number of particles in any energy state to the number of particles in a

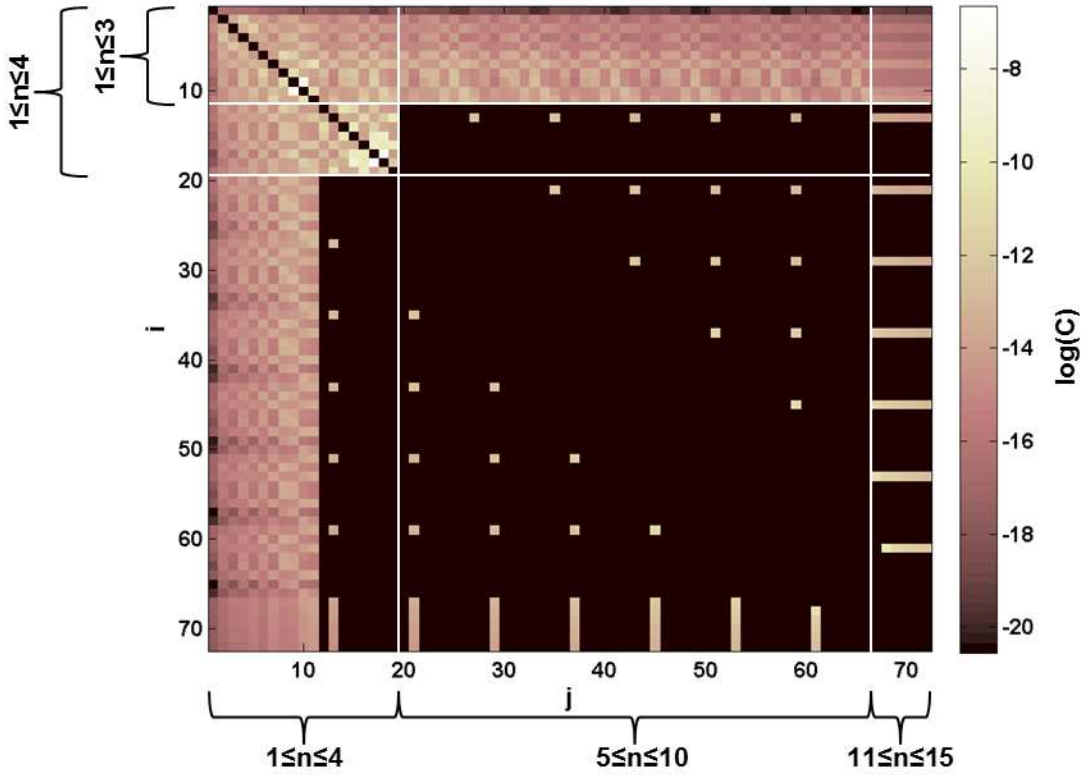

Figure 6.5: Matrix of $\log(C_{ij})$ and $\log(C_{ji})$ showing the order of magnitude of the electron induced excitation and electron induced de-excitation rates for T_e=10 eV. The matrix is indexed by lower energy state number, i, and upper energy state number, j. The ranges of quantum numbers are marked to show which transitions are included in the CGS-CRM. Black areas indicate there is no transition rate, white areas indicate the highest transition rates.

lower energy state is given by the Boltzmann relation.

$$\frac{n_j}{n_i} = \frac{g_j}{g_i}\exp\left(-\frac{(E_j - E_i)}{T_e}\right) \tag{6.20}$$

where g_j and g_i are the degeneracies of the upper and lower states, E_j and E_i are the energies of the upper and lower states in eV, and T_e is the electron temperature in eV. Therefore, the collision rate of de-excitation is related to the collision rate of

excitation by the following:

$$C_{ji} = \frac{g_i}{g_j} \exp\left(\frac{E_{ij}}{T_e}\right) C_{ij} \tag{6.21}$$

The lower triangle of the matrix in Fig. 6.5 shows the log of the rates of electron induced de-excitation, $\log(C_{ji})$, for $T_e = 10\,\mathrm{eV}$.

6.2.4 Spontaneous De-excitation

Spontaneous de-excitation occurs when a bound electron in an excited helium atom decays to a lower energy state with no electron interaction, releasing a photon. This process is the source of the emission lines. The spontaneous transition coefficient, or Einstein coefficient, is the probability that a neutral in state j will decay to level i. The transition coefficients, A_{ji}, are available from the NIST Atomic Spectra Database [81]. The database contains 697 helium emission lines for the 72 energy levels, or possible ij pairs, where i is the lower energy state and j is the upper energy state. The full list of emission lines including the transition coefficients is in table B.1.

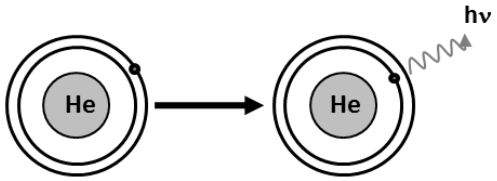

Figure 6.6: Spontaneous de-excitation.

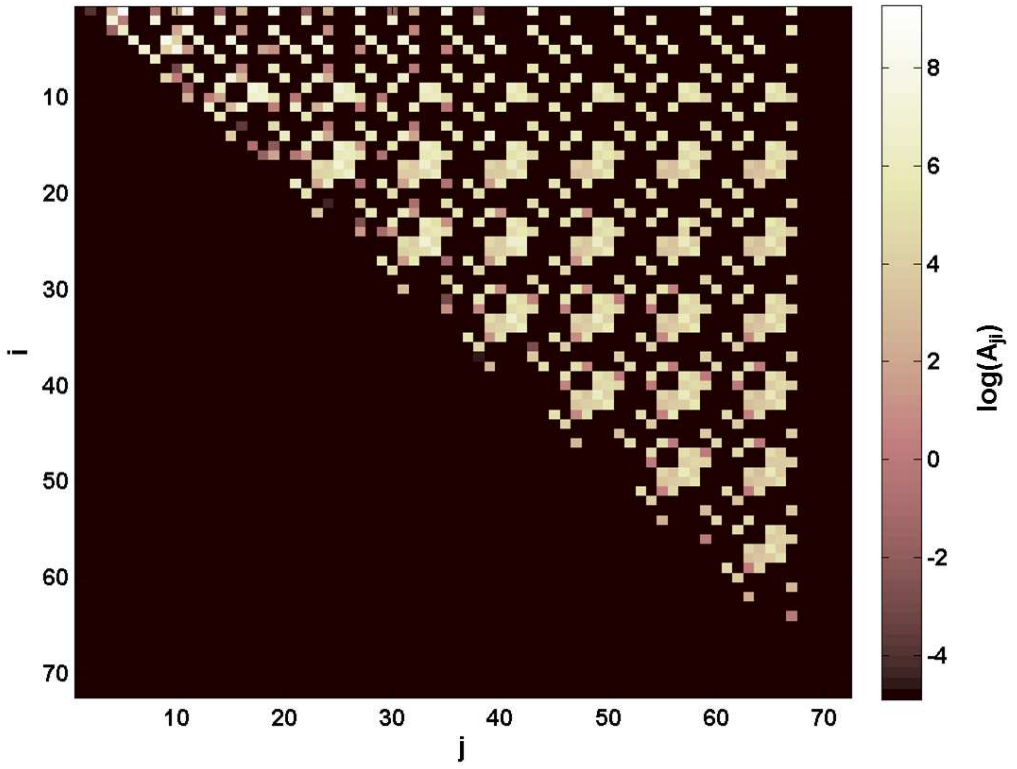

Figure 6.7: Matrix of $\log(A_{ji})$ showing the order of magnitude of the spontaneous de-excitation coefficients. The matrix is indexed by lower energy state number, i, and upper energy state number, j. Black areas indicate there is no transition probability, white areas indicate the highest transition probabilities.

Values of A_{ji} for the combined multiplet states, n^3P,D, and F, and the $F+$ states for higher values of quantum number, n, were calculated using the sub-state A_{ji} values, the wavelength, λ, and the electronic angular momenta, J [86].

$$A_{ji} = \frac{1}{\langle\lambda\rangle_{ij}^3 \sum_{J_j}(2J_j+1)} \sum_{J_i,J_j} (2J_j+1) \times \lambda(J_i,J_j)^3 \times A(J_i,J_j) \tag{6.22}$$

Figure 6.7 shows the values of $\log(A_{ji})$ for the available j to i transitions.

6.2.5 Electron Induced Ionization

Electron induced ionization occurs when a free electron collides with a neutral atom resulting in a singly charged ion and two free electrons. In the CGS-CRM, neutral atoms in the first 19 energy states (n≤4) and ^1P states for 5≤n≤15 can be ionized. The hydrogenic approximation is used for the higher quantum numbers [87].

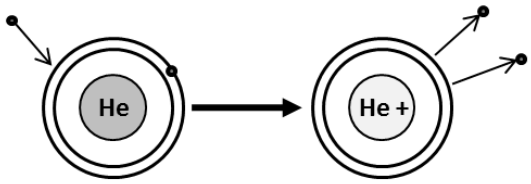

Figure 6.8: Electron induced ionization.

The ionization collisional cross sections were calculated using the empirical formula and approximations presented by Ralchenko [83]. For quantum number n≤4, the analytic expression given below was used to find the ionization cross sections in m^2.

$$\sigma_{ion}(n^{2S+1}L; E_e) = \frac{10^{-17}}{I_m E_e}\left[A_1 \ln\frac{E_e}{I_m} + \sum_{i=2}^{6} A_i \left(1 - \frac{I_m}{E_e}\right)^{i-1}\right] \tag{6.23}$$

A_i are fitting constants, I_m is the ionization energy in eV of the $n^{2S+1}L$ state, and E_e is the collision energy in eV. The ionization fitting coefficients are found in table C.4.

Energy levels above n=4 are treated like single energy states and are therefore calculated using the hydrogenic approximation. This following expression is used to

find ionization cross sections from 5≤n≤15 [87].

$$\sigma_{ion}(n; E_e) = 4\pi a_0^2 \eta \left(\frac{Ry}{I_m}\right)^2 \left(\frac{x-1}{x^2}\right) \ln(1.25\beta x) \tag{6.24}$$

where $x = E_e/I_m$, η and β are constants equal to 0.66 and 1.0 respectively, Ry is the Rydberg energy in eV, and a_0 is the Bohr radius in m.

The ionization rate for each modeled excited state of neutral helium at T_e=10 eV is shown in Fig. 6.9.

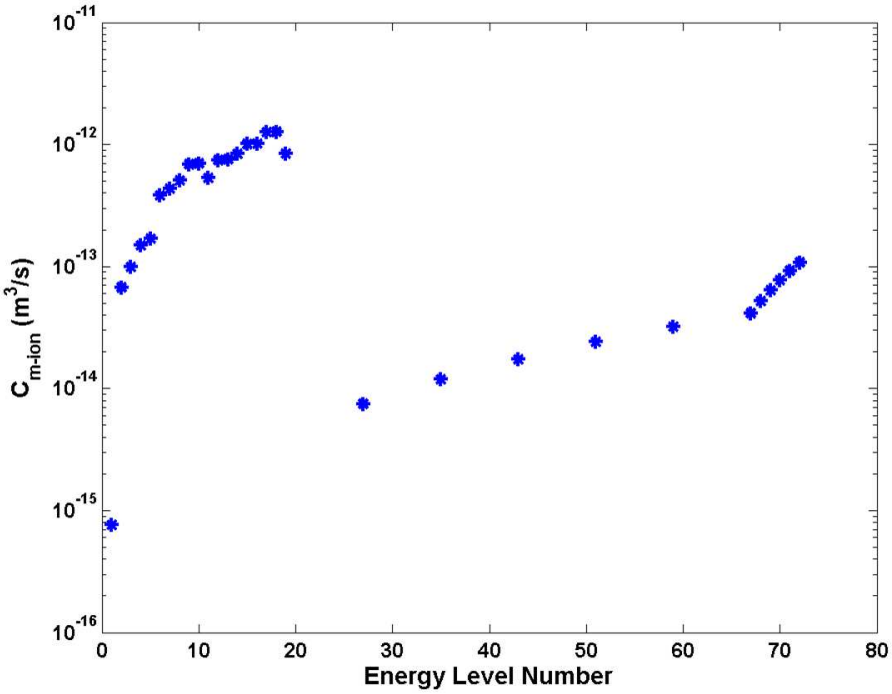

Figure 6.9: Electron induced ionization collision rates for T_e=10 eV.

6.2.6 Photo-excitation

Photo-excitation is the process by which photons get absorbed by the plasma and cause excitation of the reabsorbing particles. Photon interaction with plasma particles must be included if the plasma is optically thick, meaning that photons generated within the plasma volume are reabsorbed before they exit the plasma. The plasma volume is defined by the size of the thruster quartz tube. Optical

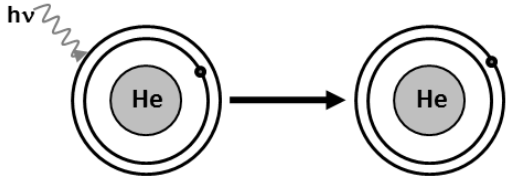

Figure 6.10: Photo-excitation.

depth is the product of the number density of absorbing particles, the absorbing particle cross section, and the length through which the radiation must travel, the tube diameter. The effective absorbing particle cross section depends on the energy state of the particle. The inclusion in a helium CRM of photo-excitation for only excitation from the ground state to n^1P states has been shown to improve the estimates of the plasma parameters, even for low electron density plasmas, since the mean free path for photon resonance from the ground state to the n^1P states is smaller than the diameter of the thruster [88]. The increase in the n^1P population directly affects the intensity value of emission lines originating from this excited state, but also affects the populations of the other emission lines through an increase

in the de-excitation rate from the n^1P states into lower states. De-excitation from the 2^1P state predominantly increases the population of the 2^1S metastable. This affects the population of upper states measured for this experiment through excitation from the metastable state and is small compared to de-excitation from higher n^1P states. While the increase in the population of the 4^1P state and higher n^1P states would contribute to energy state populations below 4^1P, the photo-excitation rate from the ground state is smaller than that for the 2^1P and 3^1P states, making the contribution to the lower states insignificant. Photo-excitation from the 2^1P state and n^1P states where n>3 have been neglected in the CGS-CRM because of their small contributions to the measured states. A parameter study for I_{2^1P} and I_{4^1P} confirmed that the influence of photo-excitation from the ground state into these states had a negligible effect on the line ratios of interest. This was also shown to be the case in a previous study [89]. The ground state photo-excitation rate, I_{3^1P}, in units of s^{-1} is an additional input to the model with n_e and T_e.

6.2.7 Radiative Ion-Electron Recombination

Radiative ion-electron recombination occurs when a free electron is captured by an ion and the particle transitions to a neutral state. A photon is released during this process. Because the model considers only singly charged ions in their ground state, all radiative recombination results in neutral particles in some excited state, m. Radiative recombination is the inverse process of photoionization, the process by which a neutral particle is ionized by a photon instead of an electron

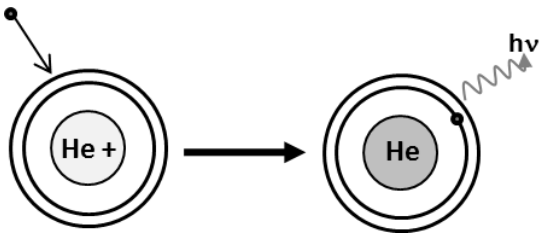

Figure 6.11: Radiative ion-electron recombination.

or heavy particle. Photoionization is neglected in the model because the plasma is optically thin for these transitions, however, radiative recombination is included because it favors transitions into ground and lower energy states. Excitation from the ground state and metastable states constitute the largest contribution to the population density of higher states. The radiative recombination rate coefficient, β_m, is calculated for the two metastable states using an empirical fit, which is a function of the degeneracy of each state and the electron temperature in Kelvin [87].

$$\beta(2^1S, 2^3S) = 5.45x10^{-19} g_{2^1S,2^3S} \sqrt{T_{eK}} \tag{6.25}$$

Equations for fits of effective radiative recombination coefficients for selected levels contributing to emission lines in the near UV to near IR spectrum are employed for states 4, 6-9, 12, 15, and 16 [90]. The coefficients listed in table 6.1 are used in the fit equation (Eq. 6.26), where $t = 10^{-4} T_{eK}/z^2$. The electron temperature, T_{eK}, is in Kelvin and β is in m^3/s. The quantity z is the ionic charge, which is 1 for the case of recombination into neutral states.

$$\beta_m = 10^{-19} \times z A_m t^{B_m} / (1 + C_m \times t^{D_m}) \tag{6.26}$$

Table 6.1: Fit coefficients for effective radiative recombination.

State Number	State m	A	B	C	D
4	2^3P	0.796	-0.525	0.148	0.719
6	3^3S	0.070	-0.509	-0.010	-0.263
7	3^1S	0.036	-0.503	0.165	0.614
8	3^3P	0.511	-0.489	0.719	0.530
9	3^3D	1.323	-0.696	1.683	0.667
12	4^3S	0.019	-0.518	-0.045	0.951
15	4^3D	0.429	-0.530	1.505	0.779
16	4^1D	0.135	-0.540	1.505	0.779

6.2.8 Three-body Recombination

Three-body recombination occurs when a singly charged ion is impacted by two free electrons. One electron is captured, neutralizing the ion, and one electron remains free. Three-body recombination is the inverse process of electron induced ionization and the rate coefficients, α_m, are derived from the ionization rates using the Saha-Boltzmann equation [91].

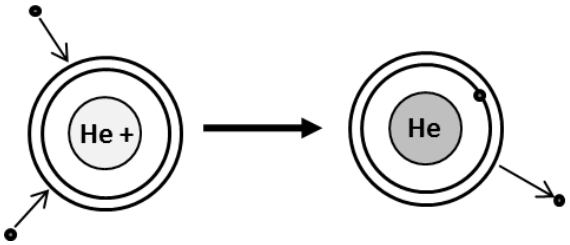

Figure 6.12: Three-body recombination.

In thermodynamic equilibrium the rate of ionization is equal to the rate of

three-body recombination,

$$C_{m-ion} n_m n_e = \alpha_m n_{ion} n_e^2 \tag{6.27}$$

The ratio of the population at excited neutral state m to the charged particle populations can be expressed via the Saha-Boltzmann equation as

$$Z_m = \frac{n_m}{n_{ion} n_e} = \frac{g_m}{2 g_{ion}} \left(\frac{h^2}{2\pi m_e q_e T_e} \right)^{3/2} \exp\left(\frac{E_{ion} - E_m}{T_e} \right) \tag{6.28}$$

By substituting Eq. 6.28 into Eq. 6.27, the three-body recombination rates can be calculated from the ionization rates using

$$\alpha_m = C_{m-ion} \frac{g_m}{4} \left(\frac{h^2}{2\pi m_e q_e T_e} \right)^{3/2} \exp\left(\frac{E_{ion} - E_m}{T_e} \right) \tag{6.29}$$

where C_{m-ion} is the electron induced ionization rate from neutral state m, g_m is the degeneracy of that state, h is Planck's constant, m_e is electron mass in kg, q_e is electron charge in C, T_e is electron temperature in eV, and $(E_{ion} - E_m)$ is the ionization energy of state m.

6.2.9 Metastable Diffusion to the Walls

The geometry of the experiment and the gas pressure in the thruster are such that the loss of metastables to the walls through diffusion should be considered. Some fraction of the metastables become ground state neutrals after contact with the tube walls, allowing for a higher population of metastables in the model with this loss mechanism included. Underestimating the total metastable population equates to an underestimate of n_e. The rate of metastable diffusion to the wall, in Eq. 6.30, is a function of the diffusion coefficient, D_m, the particle density given by the gas

pressure, n_{He0}, the tube radius, R, the tube surface area, A, and the tube volume, V. The coefficient for metastable helium diffusion in helium used in the model is $0.0146\,\mathrm{m}^2/\mathrm{s}$ at $300\,\mathrm{K}$ [92]. This transition applies to only the metastable states, $2^3\mathrm{S}$ and $2^1\mathrm{S}$.

$$\frac{\mathrm{d}n_m}{\mathrm{d}t} = -D_m \frac{n_{He0}}{R}\frac{A}{V} \tag{6.30}$$

6.3 Rate Equation

The purpose of the CGS-CRM is to compute the number densities for every helium neutral excited state, n_m, using a rate equation based on the transitions described in the previous sections. The population of helium atoms in a specific state depends on the sum of rates of excitation and de-excitation into and out of that state, leading to the main rate equation solved by the CGS-CRM.

$$\begin{aligned}\frac{\mathrm{d}n_m}{\mathrm{d}t} = &-\left[\sum_{k>m} n_m n_e C_{mk} + \sum_{j<m} A_{mj} n_m + \sum_{j<m} n_m n_e C_{mj} + n_m n_e C_{m-ion}\right] \\ &+ \sum_{j<m} n_j n_e C_{jm} + \sum_{k>m} A_{km} n_k + \sum_{k>m} n_k n_e C_{km} \\ &+ \left[n_e n_{ion}(\beta_m + \alpha_m n_e) + n_1 n_e C_{1m} + n_1 I_m - D_m \frac{n_1}{R}\frac{A}{V}\right]\end{aligned} \tag{6.31}$$

The density of the current energy state is n_m, n_j is the density of the energy states lower than the current state, n_k is the density of the energy states greater than the current energy state, n_e is the electron density, n_{ion} is the ion density, and n_1 is the density of the ground state. All densities are in units of m^{-3}. Assuming the plasma is quasi-neutral, $n_{ion} = n_e$. The ground state density, n_1, is calculated from the gas pressure measured in the thruster using the ideal gas law. The population of the ground state is assumed to be constant in this model, and is much larger

than the populations of all excited states. The rate of ionization is higher than the recombination rate and all the particles would eventually ionize if the volume of gas in the thruster was stationary. Ions that do not recombine are lost to the walls and are replaced in the observed volume by ground state neutrals flowing in from the gas tank since the rate of gas flow through the thruster is constant. The C's are the collision rate coefficients for each of the excitation, de-excitation and ionization processes in m^3/s, and the A's are the spontaneous transition probabilities in s^{-1}. The recombination coefficients for three-body and radiative recombination are α_m, in m^6/s, and β_m, in m^3/s, respectively. I_m is the photo-excitation rate for transitions from the ground state into 3^1P ($m = 11$). This component is zero for all other values of m. D_m is the metastable diffusion coefficient. This component is zero for all states above the metastable states, ($m > 3$). The index, m, ranges from 2 to 72, representing all neutral helium excited states, beginning with 2^3S. The terms in the large square brackets in equation (6.31) are processes that remove particles from state m. The remaining terms add particles to state m. The last term in the small square brackets, representing the recombination terms, electron collisional excitation and photo-excitation from the ground state into state m, and diffusion, is constant. In steady state, $dn_m/dt = 0$, so the rate equation can be expressed as a matrix equation:

$$Mx = b \tag{6.32}$$

where M is a 71×71 square matrix, x is the array of species densities, and b is the array of constants comprising recombination and ground state excitation contribu-

tions. Matrix M consists of terms for processes depleting state m on the diagonal, terms for processes adding to state m from lower states in the lower triangle, and terms for processes adding to state m from upper states in the upper triangle.

$$M = \begin{bmatrix} -(\sum n_e C_{2\to[3-72]} & & & \\ +A_{2\to1} + n_e C_{2\to1} & A_{3\to2} + n_e C_{3\to2} & \cdots & A_{72\to2} + n_e C_{72\to2} \\ +n_e C_{2\to ion}) & & & \\ & -(\sum n_e C_{3\to[4-72]} & & \\ n_e C_{2\to3} & +\sum A_{3\to[1-2]} & \cdots & A_{72\to3} + n_e C_{72\to3} \\ & +\sum n_e C_{3\to[1-2]} & & \\ & +n_e C_{3\to ion}) & & \\ \vdots & \vdots & \ddots & \vdots \\ & & & -(\sum A_{72\to[1-71]} \\ n_e C_{2\to72} & n_e C_{3\to72} & \cdots & +\sum n_e C_{72\to[1-71]} \\ & & & +n_e C_{72\to ion}) \end{bmatrix}$$

The constant term, b, is an array of the recombination and ground state excitation contributions.

$$b = \begin{bmatrix} -n_e[n_{ion}(\beta_2 + \alpha_2 n_e) + n_1 C_{1\to 2}] - D_2 \frac{n_1}{R} \frac{A}{V} \\ -n_e[n_{ion}(\beta_3 + \alpha_3 n_e) + n_1 C_{1\to 3}] - D_3 \frac{n_1}{R} \frac{A}{V} \\ \vdots \\ -n_e[n_{ion}(\beta_{11} + \alpha_{11} n_e) + n_1 C_{1\to 11}] + n_1 I_{11} \\ \vdots \\ -n_e[n_{ion}(\beta_{72} + \alpha_{72} n_e) + n_1 C_{1\to 72}] \end{bmatrix}$$

The array of population densities, x, is the quantity the CGS-CRM calculates for a given T_e and n_e.

$$x = \begin{bmatrix} n_2 \\ n_3 \\ \vdots \\ n_{72} \end{bmatrix}$$

Figure 6.13 shows an example of the output of the CGS-CRM: the population densities for the 72 energy states for an electron temperature of 10 eV and an electron density of $10^{17}\mathrm{m}^{-3}$. The ground state population is several orders of magnitude higher than the next most populous states, the metastable states.

6.4 CGS-CRM Output

The values of excited state population densities can be used to find the intensities of emission lines using the following relation:

$$I_{ij} = n_j A_{ji} \tag{6.33}$$

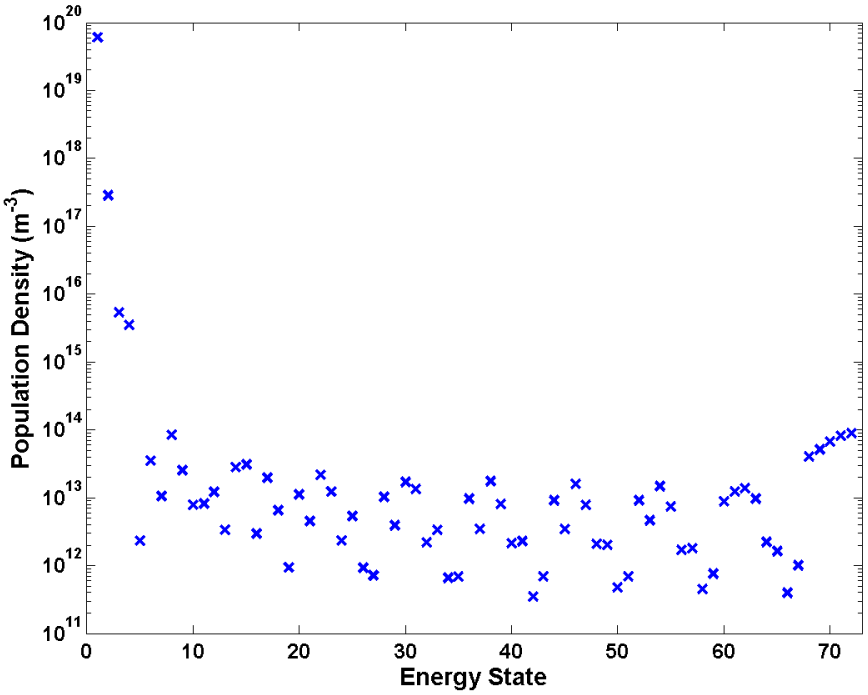

Figure 6.13: Population densities for all 72 helium states for $n_e = 10^{17}\,\mathrm{m}^{-3}$; $T_e = 10\,\mathrm{eV}$; $I_{3^1P} = 70\,\mathrm{s}^{-1}$.

where I_{ij} is the intensity of the emission line corresponding to the transition from upper energy state j to lower energy state i, n_j is the density of the upper excited energy state, and A_{ji} is the transition probability for spontaneous de-excitation from energy state j to energy state i. There are 697 emission lines modeled, corresponding to the number of spontaneous transition coefficients available for helium. The emission lines are plotted as a function of wavelength, λ_{ij}:

$$\lambda_{ij} = \frac{hc}{q_e(E_j - E_i)} \tag{6.34}$$

where h is Planck's constant in Joule-seconds, c is the speed of light in m/s, q_e is the elementary charge in C, and E_i and E_j are the energies in Joules of the lower and

upper states. An example of a simulated spectrum from the CGS-CRM including only emission lines in the visible spectrum for n_e=$10^{17}\,\mathrm{m}^{-3}$ and T_e=10 eV is shown in Fig. 6.14. The simulated emission lines are given a Gaussian shape to resemble the line broadening in the experimental data using the following formula.

$$I_{ij}(\lambda) = I_{ij0}\left(\frac{1}{\sigma_G\sqrt{2\pi}}\right)\exp-\frac{(\lambda-\lambda_{ij})^2}{2\sigma_G^2} \tag{6.35}$$

where I_{ij0} is the initial intensity of the ij line, σ_G is the variance, and λ_{ij} is the wavelength of the emission line. The variance dictates the width of the Gaussian curve and was set to 10^{-10} in the CGS-CRM.

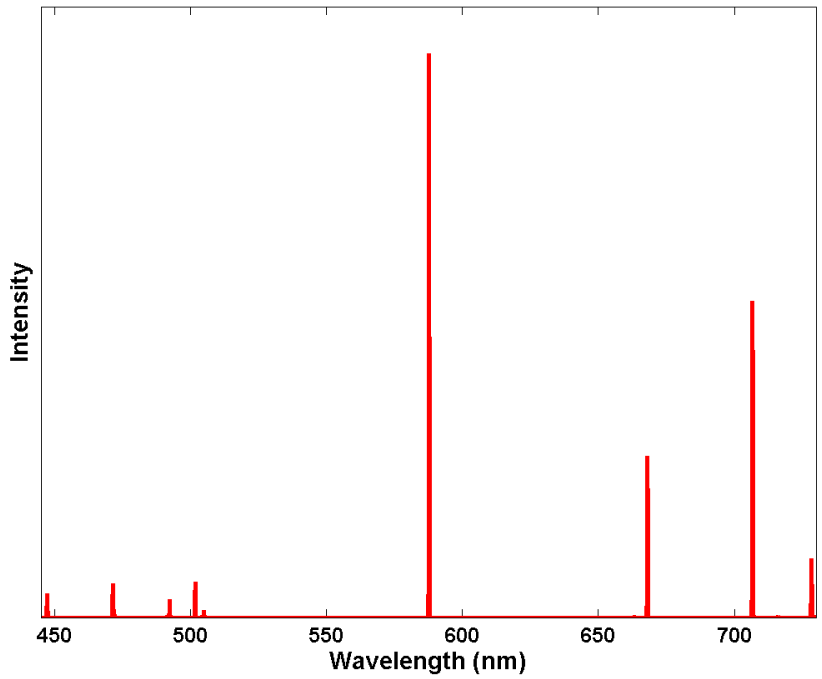

Figure 6.14: Example of a simulated helium spectrum output from the CGS-CRM for $n_e = 10^{17}\,\mathrm{m}^{-3}$, T_e=10 eV, and I_{3^1P}=$70\,\mathrm{s}^{-1}$ showing emission lines 447.1, 471.3, 492.2, 501.6, 504.8, 587.6, 667.8, 706.5, and 728.1 nm.

Since the intensity of emission lines measured by the spectrograph is in arbitrary units, the ratios of pairs of selected helium emission lines are used to compare to the spectral data. Nine helium emission lines are measured, resulting in 20 possible singlet-triplet line ratio pairs and 10 singlet-singlet line ratio pairs. The measured emission lines and their corresponding transitions are listed in Table 6.2. The line ratios acquired from the measured lines are listed in Table 6.3 and organized by transition type.

Table 6.2: Measured helium emission lines with their corresponding transitions.

Wavelength (nm)	Transition	$j \rightarrow i$	Transition Type
447.1	$4^3D \rightarrow 2^3P$	$15 \rightarrow 4$	triplet
471.3	$4^3S \rightarrow 2^3P$	$12 \rightarrow 4$	triplet
492.2	$4^1D \rightarrow 2^1P$	$16 \rightarrow 5$	singlet
501.6	$3^1P \rightarrow 2^1S$	$11 \rightarrow 3$	singlet
504.8	$4^1S \rightarrow 2^1P$	$13 \rightarrow 5$	singlet
587.6	$3^3D \rightarrow 2^3P$	$9 \rightarrow 4$	triplet
667.8	$3^1D \rightarrow 2^1P$	$10 \rightarrow 5$	singlet
706.5	$3^3S \rightarrow 2^3P$	$6 \rightarrow 4$	triplet
728.1	$3^1S \rightarrow 2^1P$	$7 \rightarrow 5$	singlet

A CGS-CRM line ratio estimate is calculated for a range of n_e from 10^{15} to $10^{19}\,\mathrm{m}^{-3}$, and a range of T_e from 1 to 30 eV. The CGS-CRM line ratio matrix can be visualized as a surface, shown in Fig. 6.15. To compare the output of the

Table 6.3: Helium emission line ratios from the measured lines.

Singlet-Triplet Ratios			Singlet-Singlet Ratios
492.2/447.1	504.8/587.6		492.2/501.6
492.2/471.3	504.8/706.5		492.2/504.8
492.2/587.6	667.8/447.1		492.2/667.8
492.2/706.5	667.8/471.3		492.2/728.1
501.6/447.1	667.8/587.6		501.6/504.8
501.6/471.3	667.8/706.5		501.6/667.8
501.6/587.6	728.1/447.1		501.6/728.1
501.6/706.5	728.1/471.3		504.8/667.8
504.8/447.1	728.1/587.6		504.8/728.1
504.8/471.3	728.1/706.5		667.8/728.1

model to the spectroscopic line ratio measurements, a curve of constant line ratio is determined from the surface plot by finding the intersection of the surface and a plane located at the measured line ratio on the z-axis. The plane is shown as a gray mesh on the surface plot in Fig. 6.15. This curve gives all the possible combinations of T_e and n_e that result in the desired line ratio value. An example of a constant line ratio curve is shown in Fig. 6.16. The circles represent the values from an average of ten thruster runs. The vertical bars represent one standard deviation for those ten tests. There were no solutions for T_e and n_e for high densities and temperatures for this particular line ratio. This curve of constant line ratio is found for all line

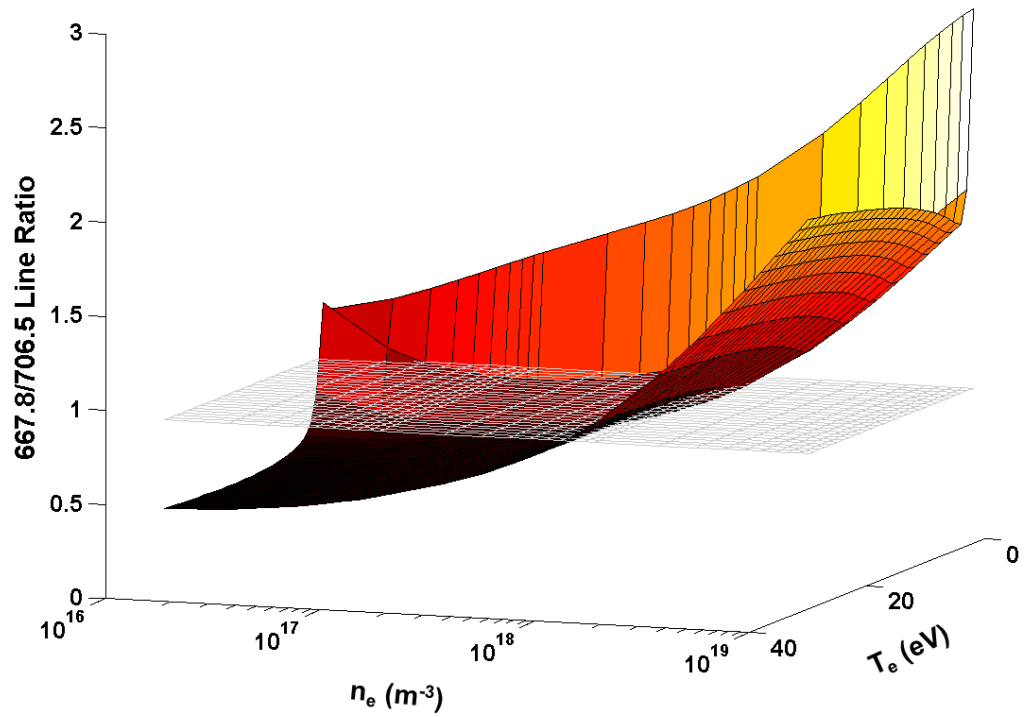

Figure 6.15: 667.8/706.5 line ratio from CGS-CRM as a function of T_e and n_e. The gray mesh plane shows the average measured value of the 687.8/706.5 line ratio for ten thruster runs. The intersection of the solid surface and the mesh is the curve of constant line ratio that gives the possible solutions for n_e and T_e.

ratios.

To determine the closest fit to the line ratio measurements for a given model input of T_e, n_e, and I_{3^1P}, the method of least squares was used to compare the measurements to line ratios calculated by the CGS-CRM [88]. Line ratios for values of n_e between 10^{15} to $10^{19}\,\mathrm{m}^{-3}$, T_e between 1 and 30 eV, and I_{3^1P} between 0 and $10{,}000\,\mathrm{s}^{-1}$ were generated. The sum of the least squares of the difference between

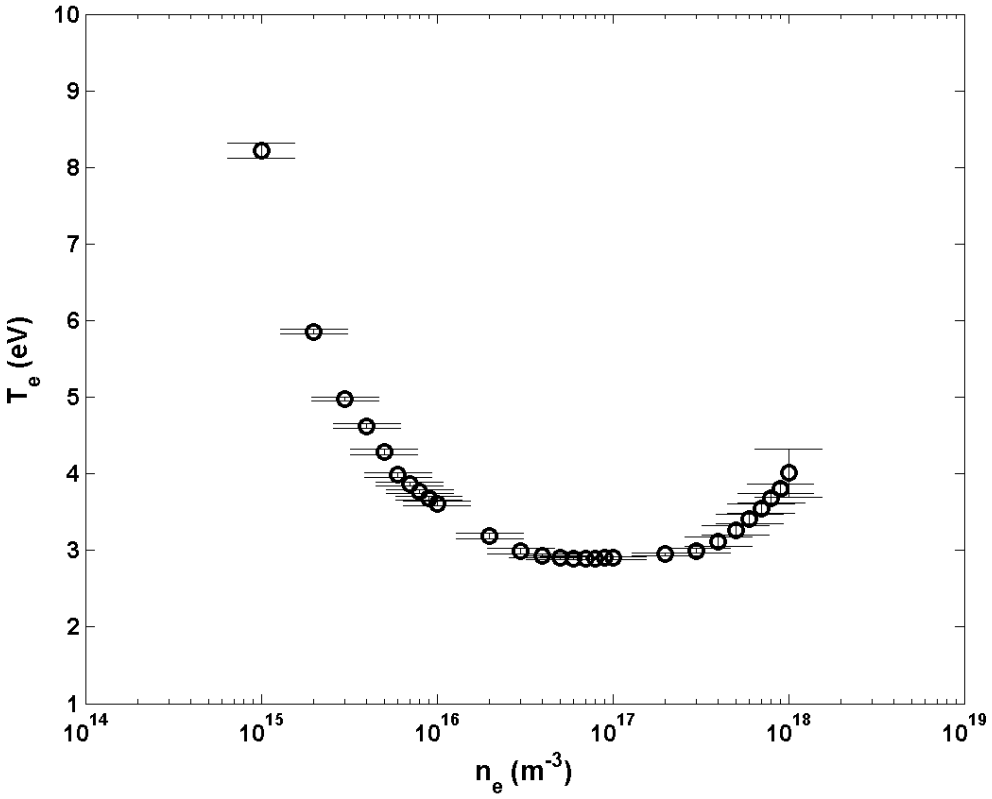

Figure 6.16: A curve of constant 667.8/706.5 line ratio for an average of ten helicon thruster runs with helium gas. The circles represent the values from the average line ratio and the bars represent one standard deviation for the tests.

the measured ratio and the model value was found for each set of input parameters using

$$f(n_e, T_e, I_{3^1P}) = \sum_p \left(\frac{LR(p) - LR_{meas}(p)}{LR_{meas}(p)} \right)^2, \tag{6.36}$$

where p is the index of the line ratio, including the 20 singlet-triplet ratios and 10 triplet-triplet ratios listed in table 6.3, LR is the ratio calculated by the CGS-CRM, and LR_{meas} is the measured ratio for an average of ten thruster tests.

6.5 Corona Model

The corona model is a simplification of a collisional radiative model that predicts T_e for the low electron density limit ($n_e \to 0$). In corona equilibrium, radiative processes occur much more frequently than collisional processes, so collisional interactions between excited energy states can be neglected. This occurs when $n_e \lesssim 10^{16}\,\mathrm{m}^{-3}$. Many of the assumptions used for the CGS-CRM apply to the corona model: the electron velocity distribution is Maxwellian, there is no heavy particle interaction, and the plasma is optically thin. The rate equation, Eq. 6.31, can be simplified such that the rate of change of the particle density in a particular state, n_m, is a function of only the rate of electron induced excitation from the ground state into state m and spontaneous de-excitation from state m into all lower states.

$$\frac{\mathrm{d}n_m}{\mathrm{d}t} = n_1 n_e C_{1m} - \sum_{j<m} A_{mj} n_m \tag{6.37}$$

In steady state, the excitation from the ground state is equal to the spontaneous de-excitation out of the current state. This relation can be solved for n_m and substituted into Eq. 6.33 for n_j to get the following equation for intensity,

$$I_{ij} = C_{1j} B_{ij} n_e n_1 \tag{6.38}$$

where C_{1j} is the rate of electron induced excitation from the ground state to state j, B_{ij} is the branching ratio, n_e is the electron density, and n_1 is the ground state density. The branching ratio is the ratio of the spontaneous de-excitation coefficient

of the $j \rightarrow i$ transition to the sum of the coefficients to all levels lower than j.

$$B_{ij} = \frac{A_{ji}}{\sum_{i<j} A_{ji}} \tag{6.39}$$

When calculating the ratio of emission line intensities, the electron and ground state densities cancel and the line ratio becomes a function of only the excitation from the ground state and the branching ratio. For example, the transition from level 16 to level 5 yields the helium emission line at 492.2 nm, and the transition from 13 to 5 yields the 504.8 nm line, resulting in the following equation for their line ratio:

$$\frac{I_{492.2}}{I_{504.8}} = \frac{C_{1\rightarrow 16} B_{16\rightarrow 5}}{C_{1\rightarrow 13} B_{13\rightarrow 5}} \tag{6.40}$$

6.5.1 Comparison of CGS-CRM to Previously Published Helium CRMs

Boivin *et al.* published line ratio data from a 5±1 eV helicon RF plasma source experiment, which they compared to their own CRM and two established models [68]. Figures 6.17, 6.18, and 6.19 were originally published in the Boivin paper. This allows for a comparison of the CGS-CRM with existing CRMs and other helicon plasma source data. Spectroscopic measurements were collected from the Auburn Steady State Research Facility (ASTRAL), a helical plasma source similar to the helicon thruster used for this study. ASTRAL was tested with both pure helium and an argon/helium mix. The gas pressure ranged from 0.5 to 100 mTorr compared to 1.88 mTorr in the helicon thruster in this study. The magnetic field strength and RF power were also higher, up to 1300 G and 2 kW, compared to 175 G and 100 W. The curves plotted in black show the various CRMs used in the study, and the circles highlighted in green and plus signs highlighted in pink show the data from their

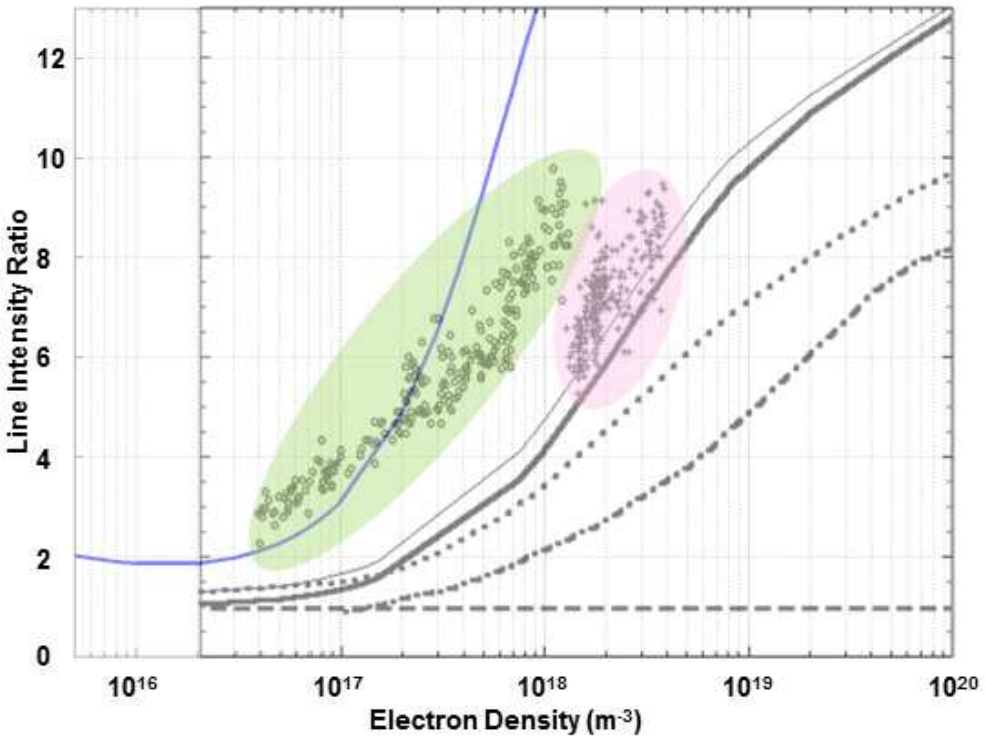

Figure 6.17: Plot showing ASTRAL 5 eV helicon plasma source data and CRM estimates for 492.2/504.8 line ratio [68]. The horizontal black dashed line shows the Boivin corona model. The thick solid black line shows the Boivin CRM for the no metastable condition. The thin solid black line shows the Boivin CRM for equilibrium conditions. The black dotted line shows the Sasaki CRM. The black dash-dot line shows the Brosda CRM. The circles highlighted in green show Boivin's line ratio data for pure helium. The plus signs highlighted in pink show Boivin's data for the argon/helium mix. The solid blue line shows the CGS-CRM.

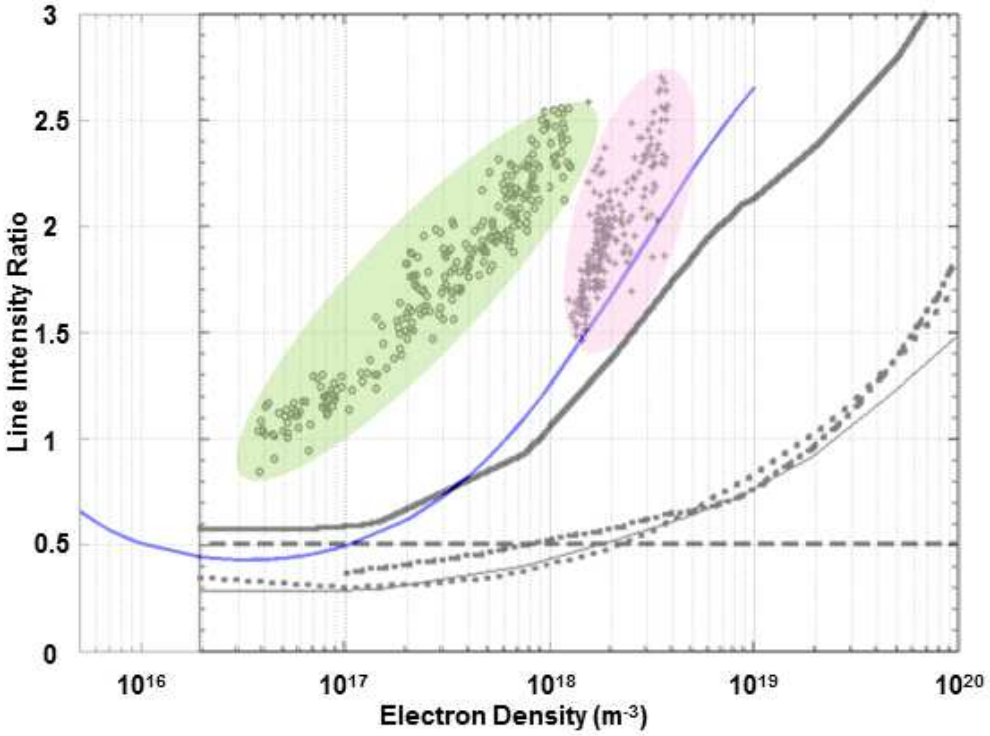

Figure 6.18: Plot showing ASTRAL 5 eV helicon plasma source data and CRM estimates for 492.2/471.3 line ratio [68]. The horizontal black dashed line shows the Boivin corona model. The thick solid black line shows the Boivin CRM for the no metastable condition. The thin solid black line shows the Boivin CRM for equilibrium conditions. The black dotted line shows the Sasaki CRM. The black dash-dot line shows the Brosda CRM. The circles highlighted in green show Boivin's line ratio data for pure helium. The plus signs highlighted in pink show Boivin's data for the argon/helium mix. The solid blue line shows the CGS-CRM.

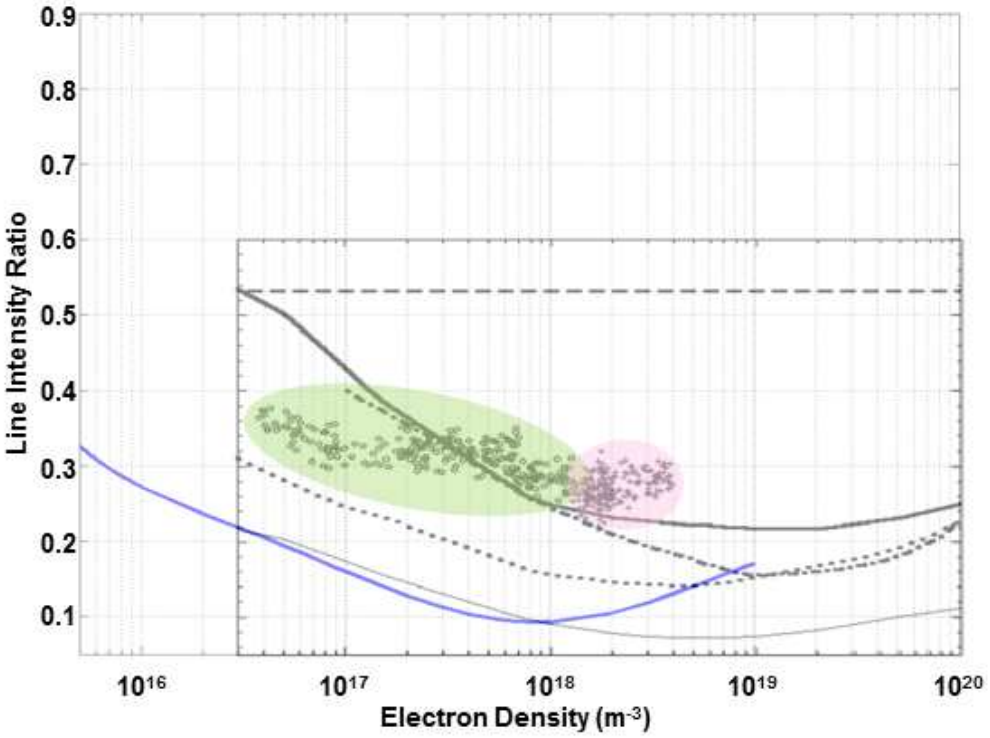

Figure 6.19: Plot showing ASTRAL 5 eV helicon plasma source data and CRM estimates for 504.8/471.3 line ratio [68]. The horizontal black dashed line shows the Boivin corona model. The thick solid black line shows the Boivin CRM for the no metastable condition. The thin solid black line shows the Boivin CRM for equilibrium conditions. The black dotted line shows the Sasaki CRM. The black dash-dot line shows the Brosda CRM. The circles highlighted in green show Boivin's line ratio data for pure helium. The plus signs highlighted in pink show Boivin's data for the argon/helium mix. The solid blue line shows the CGS-CRM.

helicon plasma source with both helium and an argon/helium mixed gas respectively. Boivin's data comparison includes three CRMs, a model developed by Brosda, shown by the dash-dot line, a model developed by Fujimoto/Sasaki, shown by the dotted line, and a model developed by Boivin that uses two different assumptions to arrive at the line ratio values [68, 72, 93]. These models differ from the CGS-CRM in a number of ways. The Brosda CRM includes interactions with only the first 19 levels, up to n=4. The Fujimoto/Sasaki CRM is the basis for the CGS-CRM. It includes interactions between higher levels, up to n=25. Both of these CRMs do not include recombination. The Boivin model assumes that the only the populations of the ground state and the first metastable state contribute to the higher state populations, and these populations were calculated using an equilibrium ionization balance. This model includes a recombination term. Two limiting cases of this model are shown in the plots: one with the first metastable state contribution (the thin solid black line), and one where the metastable contribution was neglected (the thick solid black line). In addition to the CRM, Boivin also included a corona model line ratio estimate, marked by the black horizontal dashed line. None of these CRMs include photo-excitation or metastable diffusion. The Brosda and Fujimoto/Sasaki CRMs do not use a constant value for the ground state population. Both the ground state and the first metastable state populations are constant in Boivin's CRM. The metastable populations in the CGS-CRM are computed in within the model by the same transitions as the higher states. The solid blue line on figures 6.17, 6.18, and 6.19 shows the line ratios calculated by the CGS-CRM as a function of n_e for 5 eV. It is the only CRM to have some agreement with the 492.2/504.8 line

ratio for helium and the 492.2/471.3 line ratio for the argon/helium mix, however it does not match for the 504.8/471.3 line ratio while the Boivin and Brosda CRMs agree with the data between $10^{17}<n_e<10^{18}$. Some variation can be attributed to the CRMs in Boivin's study using different sources for the collisional cross sections and not including photo-excitation or metastable diffusion. These effects are small and metastable diffusion may be negligible in Boivin's experiment because of the larger tube geometry. The majority of the difference between the CGS-CRM and the Brosda and Fujimoto/Sasaki CRMs is likely attributed to larger contributions to upper states from the ground state being kept constant. The contributions from both the metastable states and possibly higher states is likely the main source of differences between the CGS-CRM and the Boivin CRM.

Chapter 7: Results

The results from thruster tests with pure helium, pure argon, argon/helium mixed gas, and water vapor/helium mixed gas are presented. Emission spectroscopy analysis was completed for all propellants. Single and triple LP analysis was applied to the helium, argon, and argon/helium mix tests.

7.1 Helium

Measurements of n_e and T_e were collected from the Langmuir probes with spectroscopic measurements of the nine emission lines for ten runs of pure helium gas. The results from the corona model and the CGS-CRM are presented. Ten tests of the thruster were conducted at 100 W RF power and $2.5\text{x}10^{-3}$ mbar of gas pressure.

7.1.1 Langmuir Probe Results

Both the single and triple LPs were used to collect measurements from the ten thruster tests. The triple LP measured 9.4 eV for T_e with one standard deviation of 0.10 eV. The single LP measured $2.4\text{x}10^{16}\,\text{m}^{-3}$ for n_e with one standard deviation of $0.15\text{x}10^{16}\,\text{m}^{-3}$. The I-V curve from the single LP had the low electron density

curve shape, and was therefore not used to get a second T_e measurement.

7.1.2 Emission Spectrograph Results

Table 7.1: Average and one standard deviation of measured emission line ratios from ten helium tests.

Singlet-Triplet		Singlet-Singlet	
He Line Ratio	Measurement	He Line Ratio	Measurement
492.2/447.1	1.048±0.017	492.2/501.6	0.184±0.003
492.2/471.3	0.947±0.011	492.2/504.8	1.156±0.003
492.2/587.6	0.184±0.004	492.2/667.8	0.228±0.004
492.2/706.5	0.189±0.005	492.2/728.1	0.242±0.006
501.6/447.1	5.701±0.174	501.6/504.8	6.285±0.099
501.6/471.3	5.150±0.127	501.6/667.8	1.240±0.021
501.6/587.6	0.998±0.024	501.6/728.1	1.317±0.017
501.6/706.5	1.025±0.013	504.8/667.8	0.197±0.003
504.8/447.1	0.907±0.017	504.8/728.1	0.163±0.004
504.8/471.3	0.819±0.011	667.8/728.1	1.062±0.017
504.8/587.6	0.159±0.003		
504.8/706.5	0.163±0.004		
667.8/447.1	4.598±0.136		
667.8/471.3	4.154±0.102		
667.8/587.6	0.805±0.012		
667.8/706.5	0.826±0.012		
728.1/447.1	4.330±0.160		
728.1/471.3	3.911±0.122		
728.1/587.6	0.758±0.017		
728.1/706.5	0.778±0.002		

The nine emission line intensities were collected and processed as described in Chapter 5. Table 7.1 lists the intensity ratio values for the line ratios organized by transition type. The table shows the average ratios and one standard deviation from the ten tests. Figure 7.1 shows an example of the full spectra collected during

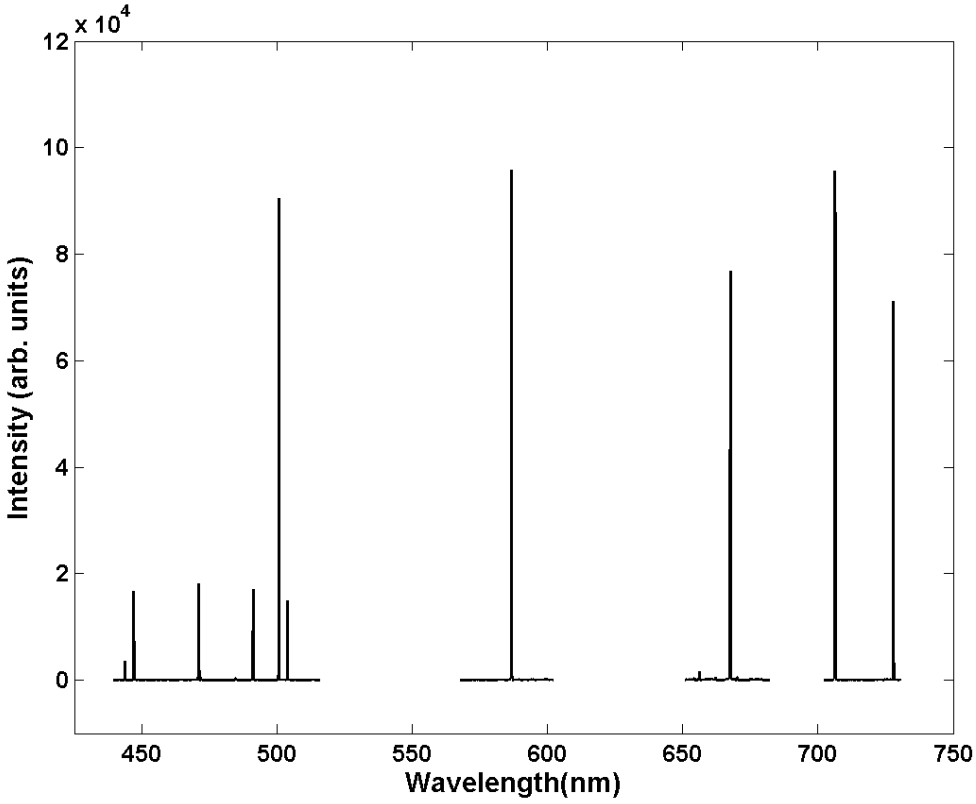

Figure 7.1: Helium emission lines showing five observed windows centered at 460.00, 500.00, 587.56, 667.82, and 718.00 nm.

a helium test for all five collection windows.

7.1.3 Corona Model Results

The single LP measured 2.4x10^{16} m^{-3} for n_e and returned an I-V curve characteristic of low electron density plasma. This indicates that the plasma is near the upper limit of the corona model regime, so analysis was completed on the helium test results to determine T_e using the corona model. The results for the 30 line ratios are shown in Fig. 7.2. Line ratios that do not appear on the plot do not have a solution within the 1 to 30 eV range. Singlet-triplet ratios that return estimates within 2 eV of the measured T_e are 504.8/471.3, 504.8/706.5, 728.1/471.3, and 728.1/706.5. The 492.2/471.3 and 492.2/706.5 ratios give estimates within 4 eV. These particular ratios may have the least amount of influence from upper level transitions and metastable states. The corona model is not expected to return a reasonable T_e estimate for all line ratios. The 501.6 nm emission line is heavily influenced by photo-excitation, which is not included in the corona model. Ratios with this line should not be considered.

Since the corona model estimates depend on only the collisional excitation rate from the ground state and the spontaneous de-excitation coefficients, uncertainties in either of these two quantities may affect the T_e estimate significantly. Corona model predictions of T_e were found using four databases containing ground state excitation cross sections in addition to the 2008 Ralchenko fits. This comparison is shown in Fig. 7.3. The results of the corona model using the updated Ralchenko cross

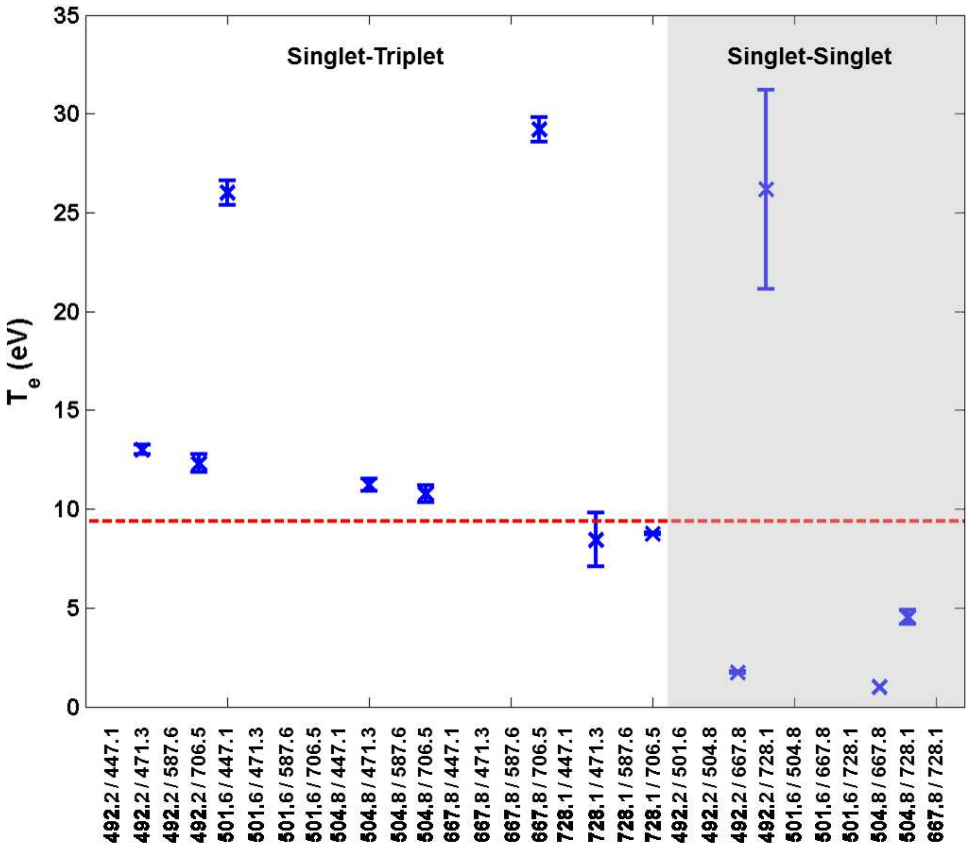

Figure 7.2: T_e estimates from the corona model showing the average and one standard deviation from ten helium tests. The triple LP measurement, 9.4 eV, shown as a red dashed line.

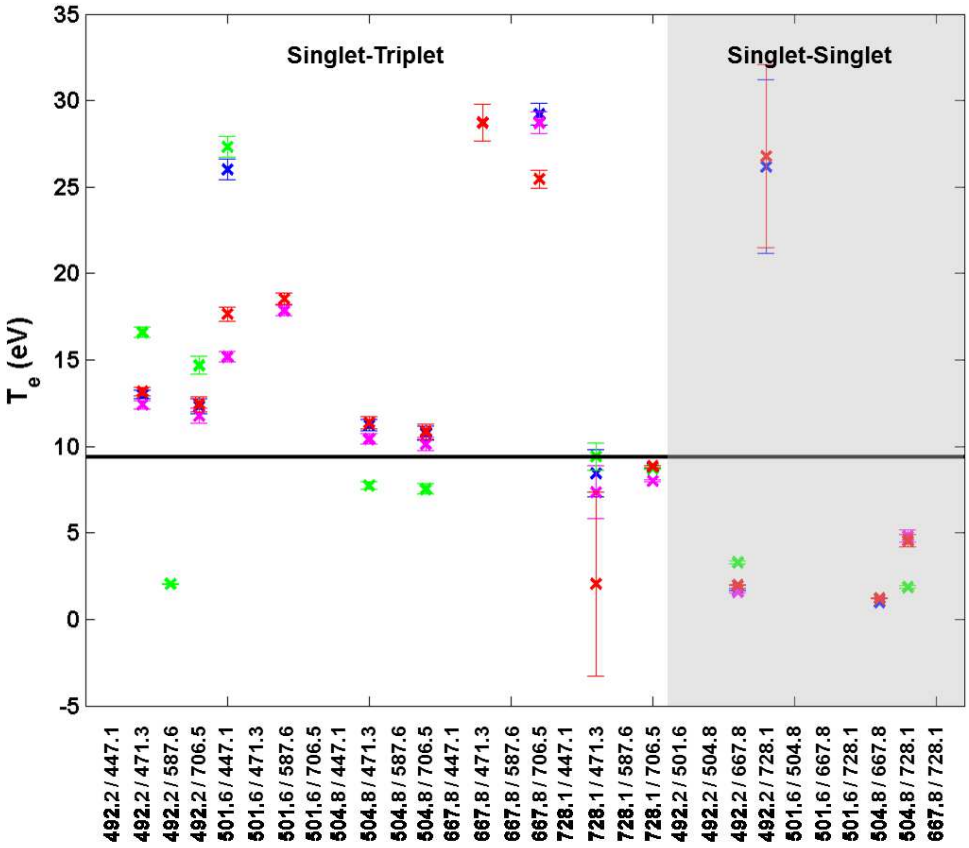

Figure 7.3: T_e estimates from the corona model using helium ground state electron induced excitation cross sections from four sources. The blue ×'s are Ralchenko 2008 cross sections. The magenta ×'s are Biagi 8.9 database cross sections. The green ×'s are Convergent Close Coupling (CCC) cross sections. The red ×'s are IST-Lisbon (2018) cross sections. Each point shows the T_e estimate for the average line ratio from ten tests and one standard deviation.

sections are shown by the blue × symbol, identical to the plot in Fig 7.2 [83]. The remaining cross section databases were acquired from the Plasma Data Exchange Project's LxCat [94]. Cross section values from the following databases were used with the corona model: Biagi 8.9, Convergent Close-Coupling (CCC), and IST-Lisbon [95–98]. Each point on the figure represents the T_e estimate from the corona model for the line ratio listed on the x-axis. The T_e predictions vary by only 1 eV for 728.1/706.5, which returned the closest estimate to the measured T_e, but vary by more than 4 eV for 504.8/471.3, 504.8/706.5, and 728.1/471.3. The largest variation of 12 eV is in the 501.6/447.1 ratio. Several ratios produce solutions for some cross section values, but not others: 492.2/587.6, 667.8/471.3, 667.8/706.5, 492.2/728.1, and 504.8/667.8. The amount of variation in T_e from changing the ground state excitation cross section source is on the order of the expected value of T_e. This suggests that the cross section values might not be accurate enough to predict plasma parameters in the temperature and density range over which the helicon thruster operates.

7.1.4 CGS-CRM Results

The least squares sum, f, from Eq. 6.36, was minimized for $n_e = 10^{16}\,\mathrm{m}^{-3}$, $T_e = 30\,\mathrm{eV}$, and $I_{3^1P} = 70$. The prediction for n_e is 2.4 times lower than the LP measurement, well within an order of magnitude, but the temperature estimate is higher than the measured value and beyond the upper limit of the parameter sweep for the CGS-CRM.

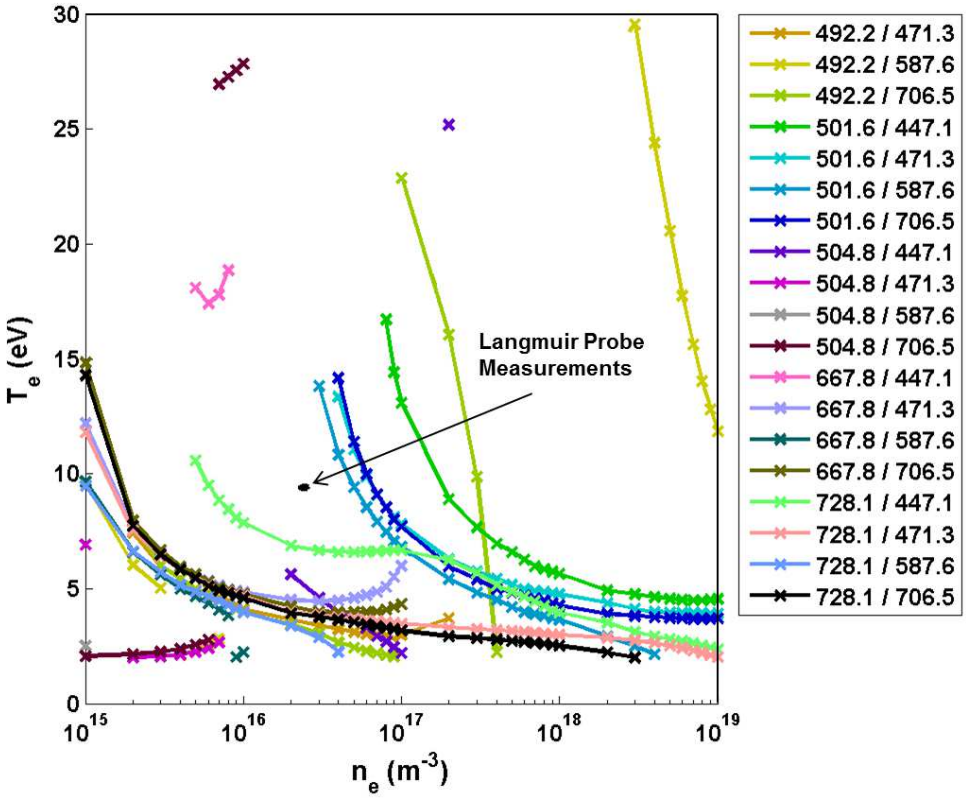

Figure 7.4: Singlet-triplet curves of constant line ratio for an average of ten helium tests. The black ellipse shows the Langmuir probe measurements for the ten tests.

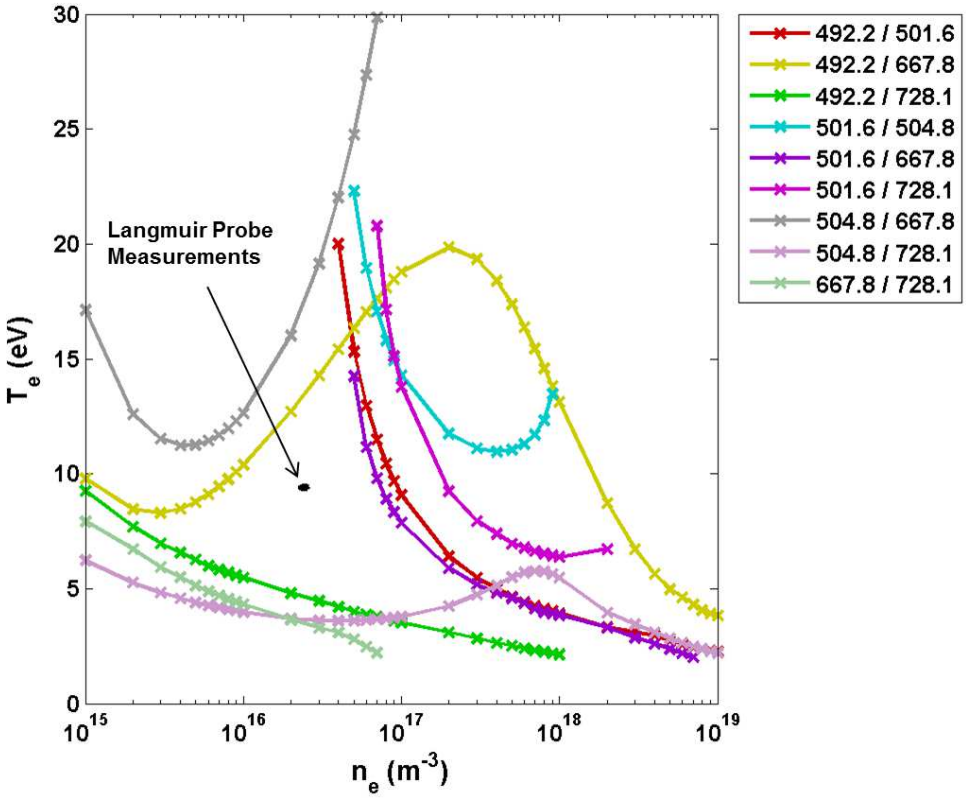

Figure 7.5: Singlet-singlet curves of constant line ratio for an average of ten helium tests. The black ellipse shows the Langmuir probe measurements for the ten tests.

To determine the accuracy of the individual line ratios, curves of constant line ratio are plotted. Figure 7.4 shows the constant line ratio curves for the singlet-triplet ratios and Fig. 7.5 shows the constant line ratio curves for the singlet-singlet ratios, both plotted with the helium LP data. The curves indicate the sets of n_e and T_e values for which the CGS-CRM returns the average measured line ratio value. They can be visualized as the intersections of the surface plots like the one shown in figure 6.15 and a plane on the z-axis at the measured line ratio value. Ideally, all the line ratio curves would intersect at a single value for T_e and n_e. The standard deviation of the constant line ratio values is not shown on the plot to reduce the complexity of the graph. There is no overlap between the LP measurements and one standard deviation for the constant line ratio curves. Most of the line ratio curves on the singlet-triplet ratio plot converge to a T_e estimate of about 4 eV for the measured n_e, about 5 eV lower than the LP measurement. The singlet-singlet ratio plot does not have a clear convergence to a single value of n_e.

7.2 Argon and Argon/Helium Mixed Gas

Langmuir probe measurements of n_e and T_e were collected with spectroscopic measurements for ten runs of argon/helium mixed gas at a mix ratio of 83% argon and 17% helium, as well as pure argon. The tests demonstrate that adding the helium gas to the argon does not significantly change the performance of the thruster. Ten tests of the thruster were conducted at 100 W RF power and 1.2x10^{-3} mbar of gas pressure for the argon/helium mix, and 1.0x10^{-3} mbar of gas pressure for the

pure argon.

7.2.1 Langmuir Probe Results

Measurements were made for both the pure argon and the argon/helium mix with the single and triple LPs and the spectrograph. To show that adding the helium to the argon does not significantly affect the plasma parameters, and therefore the performance of the thruster, both pure argon and the argon/helium mix were measured with the LPs. These measurements are listed in table 7.2. The difference between the T_e measurements for the mixed gas is less than 10%. All measurements are consistent within 1 eV. The T_e measurement from both LPs and the n_e measurement is slightly higher for the mixed gas over the pure argon, but this can probably be attributed to the higher gas pressure. Both the single and triple LP predict T_e within 1 eV, validating the measurement. In addition, spectra from the pure argon and the argon/helium mix show that the argon emission line intensities are nearly identical, illustrated in figure 5.6, further indicating that the helium is not having an effect on the overall thruster performance with the argon propellant.

Table 7.2: LP measurements for argon and argon/helium mix.

Gas	Single LP T_e (eV)	Triple LP T_e (eV)	Single LP n_e ($10^{17}\mathrm{m}^{-3}$)
100% Ar	5.45±0.14	5.46±0.03	1.14±0.07
83% Ar + 17% He	5.87±0.12	5.51±0.03	1.17±0.05

7.2.2 Emission Spectrograph Results

The line intensity measurements for the argon/helium mix are listed in Table 7.1. The table shows the average and one standard deviation from ten tests. Figure 7.6 shows an example of the full spectra collected for the argon/helium mix runs. The argon lines are numerous and the additional step of filtering them out to get unobscured helium lines was necessary.

Table 7.3: Average and one standard deviation of measured emission line ratios from ten argon/helium mixed gas tests.

Singlet-Triplet		Singlet-Singlet	
He Line Ratio	Measurement	He Line Ratio	Measurement
492.2/447.1	0.483±0.170	492.2/501.6	0.456±0.011
492.2/471.3	0.671±0.183	492.2/504.8	1.356±0.079
492.2/587.6	0.059±0.003	492.2/667.8	0.149±0.013
492.2/706.5	0.079±0.005	492.2/728.1	0.179±0.010
501.6/447.1	1.059±0.358	501.6/504.8	2.976±0.162
501.6/471.3	1.470±0.383	501.6/667.8	0.327±0.032
501.6/587.6	0.130±0.008	501.6/728.1	0.393±0.025
501.6/706.5	0.174±0.013	504.8/667.8	0.110±0.011
504.8/447.1	0.363±0.155	504.8/728.1	0.059±0.005
504.8/471.3	0.501±0.172	667.8/728.1	1.206±0.058
504.8/587.6	0.044±0.003		
504.8/706.5	0.059±0.005		
667.8/447.1	3.309±1.362		
667.8/471.3	4.577±1.506		
667.8/587.6	0.401±0.024		
667.8/706.5	0.533±0.024		
728.1/447.1	2.727±1.045		
728.1/471.3	3.776±1.139		
728.1/587.6	0.332±0.012		
728.1/706.5	0.442±0.012		

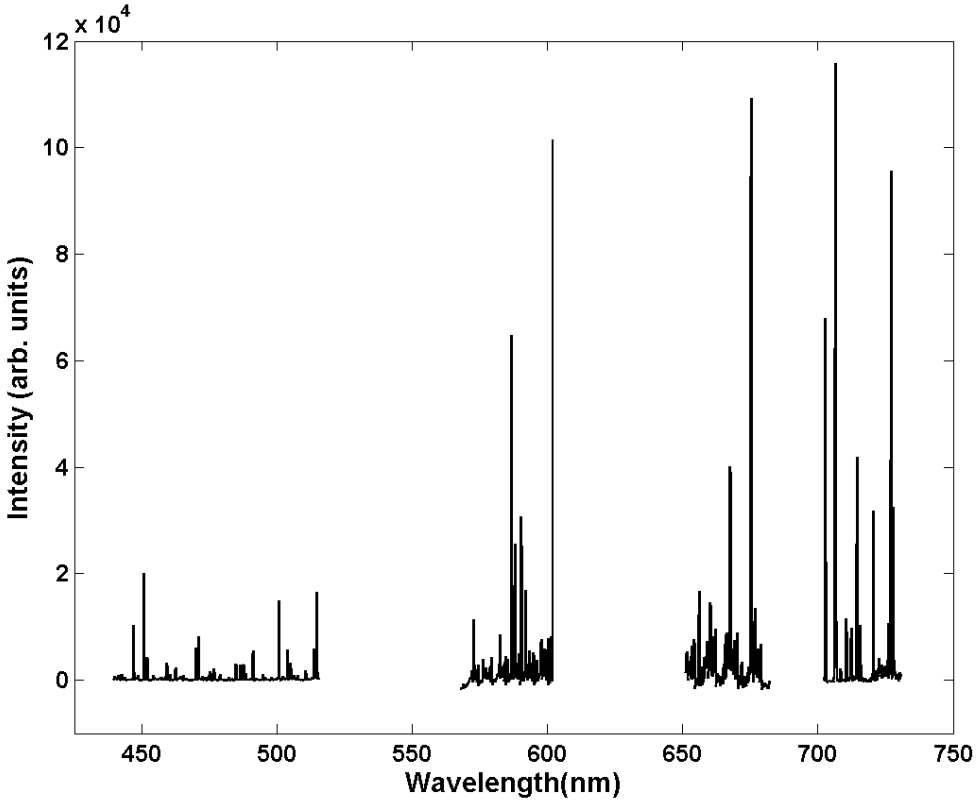

Figure 7.6: Argon/helium mix emission lines showing five observed windows centered at 460.00, 500.00, 587.56, 667.82, and 718.00 nm.

7.2.3 CGS-CRM Results

The minimum least squares sum for the argon/helium tests occurred for $n_e = 7\text{x}10^{16}\,\text{m}^{-3}$, $T_e = 25\,\text{eV}$, and $I_{3^1P} = 107$. The LP measured $10^{17}\,\text{m}^{-3}$, around 60% higher than the CGS-CRM estimate. The estimate is once again within the order of magnitude of the LP measurement. The T_e estimate from the CGS-CRM is 4 times greater than the LP measurement.

Figure 7.7 shows the constant line ratio curves for the singlet-triplet ratios, showing a convergence of the curves around 5 eV. This is a similar estimate to the singlet-triplet curves for the helium tests, but agrees well with the argon/helium LP measurement. The LP data falls within one standard deviation for only the 728.1/447.1 line ratio curve. Figure 7.8 shows the constant line ratio curves for the singlet-singlet ratios. Like the helium results, there is no clear convergence at a single n_e value.

7.3 Water Vapor/Helium Mixed Gas

Only the spectrograph was used to collect measurement for the water vapor/helium mix plasma tests. Ten tests were conducted at 100 W RF power and $2.5\text{x}10^{-3}\,\text{mbar}$. The mixed gas consisted of 80% water vapor and 20% helium.

7.3.1 Emission Spectrograph Results

Figure 7.9 shows the full spectral measurement for one water vapor/helium mixed gas test. Two Balmer series hydrogen lines at 486.1 and 656.5 nm are visible

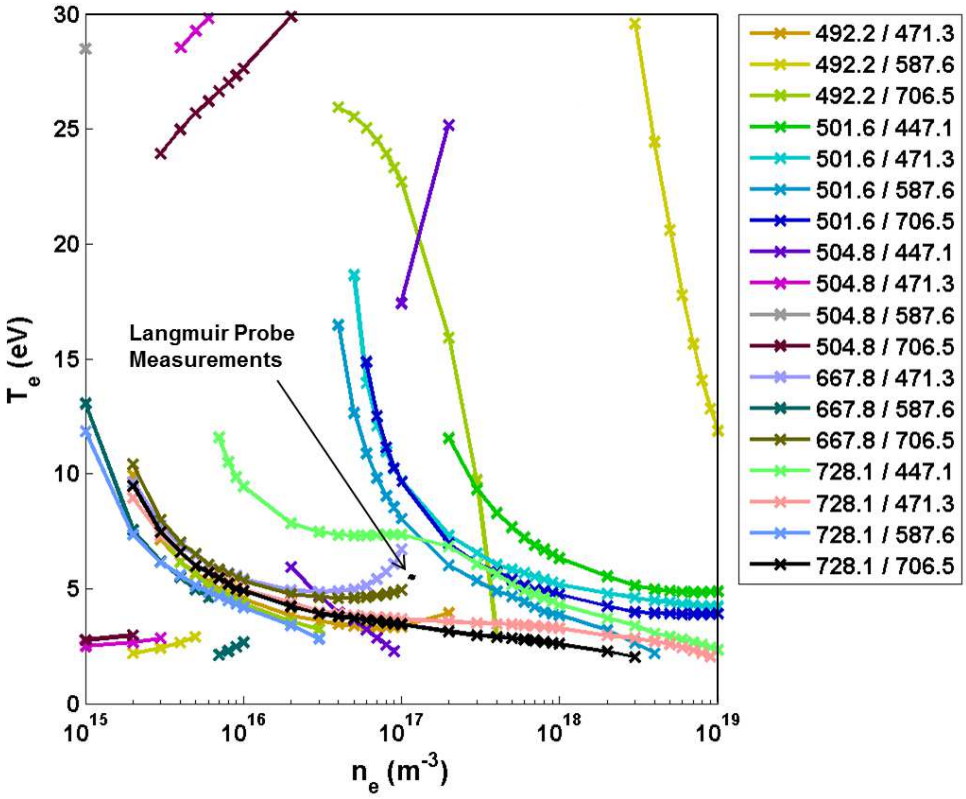

Figure 7.7: Singlet-triplet curves of constant line ratio for an average of ten argon/helium mix tests. The black ellipse shows the Langmuir probe measurements for the ten tests.

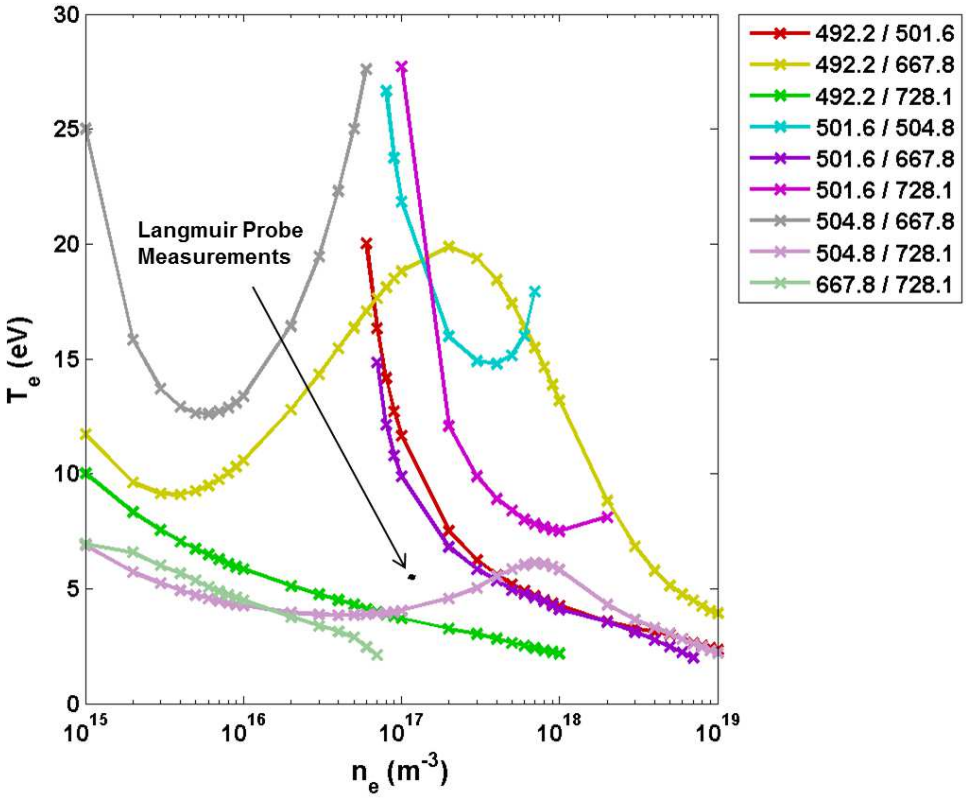

Figure 7.8: Singlet-singlet curves of constant line ratio for an average of ten argon/helium mix tests. The black ellipse shows the Langmuir probe measurements for the ten tests.

Table 7.4: Average and one standard deviation of measured emission line ratios from ten water vapor/helium mixed gas tests.

Singlet-Triplet		Singlet-Singlet	
He Line Ratio	Measurement	He Line Ratio	Measurement
492.2/447.1	0.794±0.018	492.2/501.6	0.347±0.024
492.2/471.3	0.696±0.015	492.2/504.8	1.157±0.015
492.2/587.6	0.172±0.008	492.2/667.8	0.193±0.007
492.2/706.5	0.114±0.005	492.2/728.1	0.183±0.008
501.6/447.1	2.300±0.165	501.6/504.8	3.355±0.297
501.6/471.3	2.018±0.155	501.6/667.8	0.561±0.052
501.6/587.6	0.500±0.060	501.6/728.1	0.531±0.061
501.6/706.5	0.330±0.039	504.8/667.8	0.167±0.006
504.8/447.1	0.687±0.019	504.8/728.1	0.098±0.004
504.8/471.3	0.602±0.015	667.8/728.1	0.946±0.023
504.8/587.6	0.149±0.006		
504.8/706.5	0.098±0.004		
667.8/447.1	4.112±0.133		
667.8/471.3	3.606±0.112		
667.8/587.6	0.891±0.026		
667.8/706.5	0.587±0.015		
728.1/447.1	4.352±0.188		
728.1/471.3	3.815±0.149		
728.1/587.6	0.942±0.010		
728.1/706.5	0.621±0.003		

and are significantly more intense than the helium lines. This indicates that power going into the gas is dissociating the water vapor into hydrogen and OH.

7.3.2 CGS-CRM Results

The minimum of the least squares function was achieved for the water vapor/helium plasma at $n_e = 3\text{x}10^{16}\,\text{m}^{-3}$, $T_e = 30\,\text{eV}$, and $I_{3^1P} = 81$. This density estimate is in between the helium and the argon/helium mix estimates. The tem-

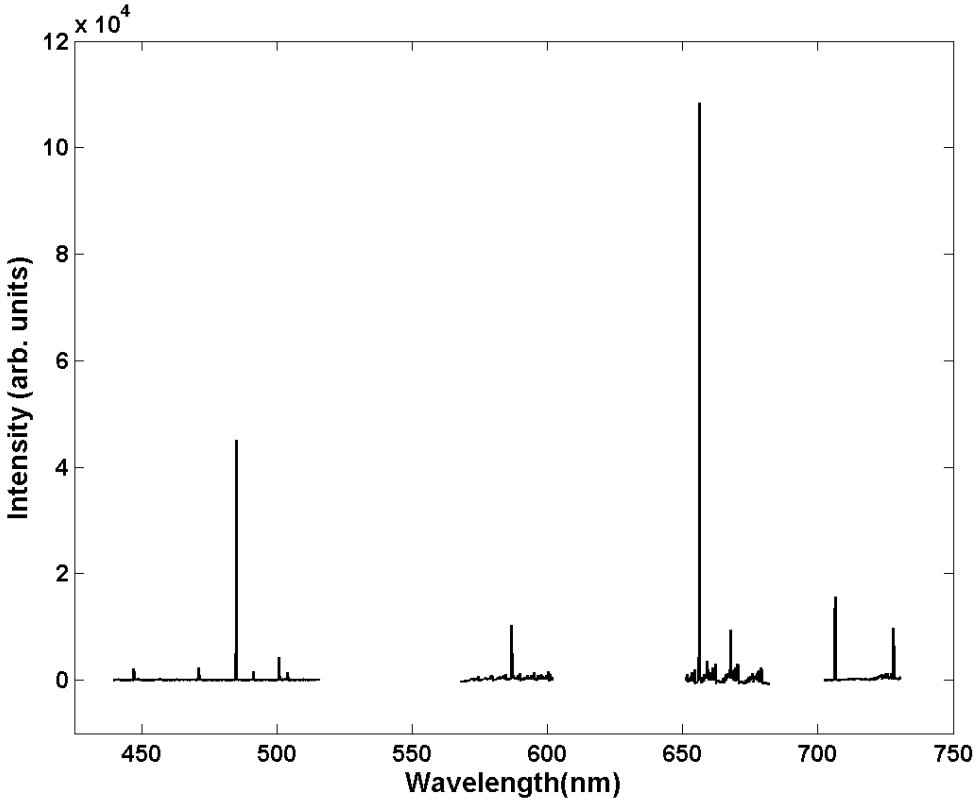

Figure 7.9: Water vapor/helium mix emission lines showing five observed windows centered at 460.00, 500.00, 587.56, 667.82, and 718.00 nm.

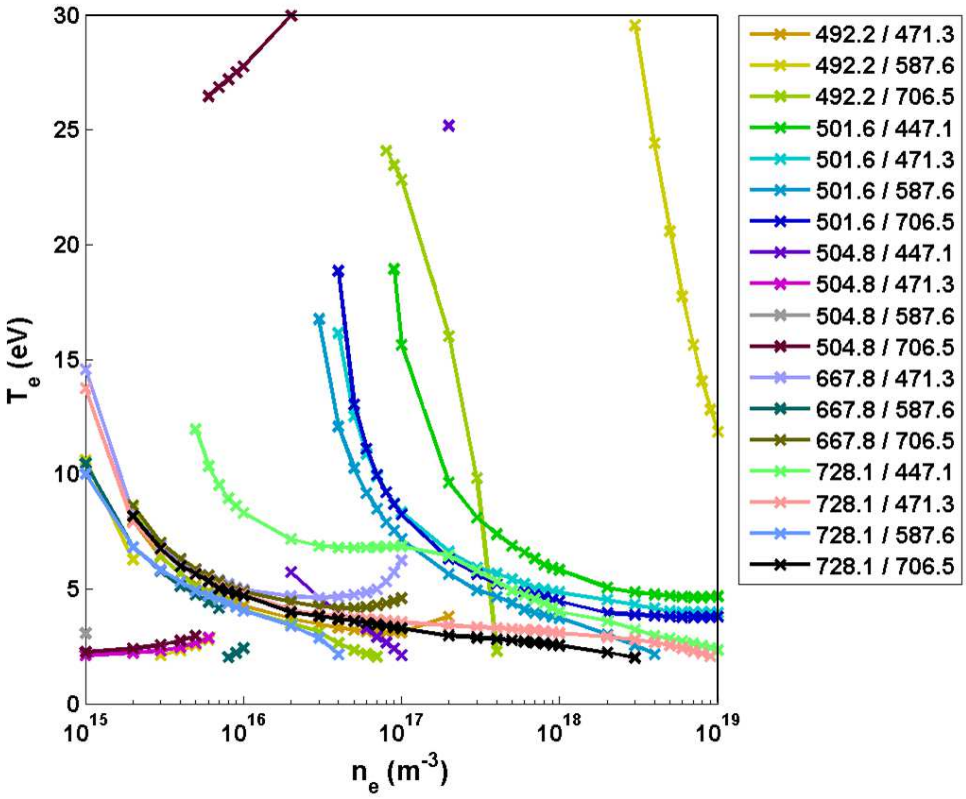

Figure 7.10: Singlet-triplet curves of constant line ratio for an average of ten water vapor/helium mix tests.

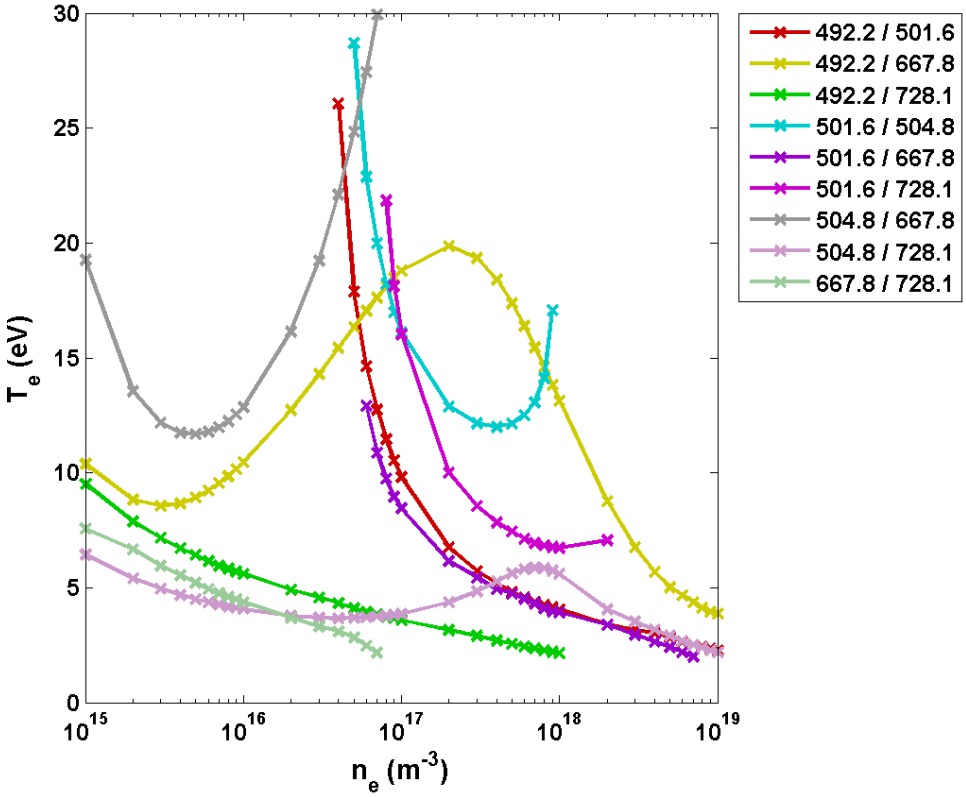

Figure 7.11: Singlet-singlet curves of constant line ratio for an average of ten water vapor/helium mix tests.

perature estimate is high, as the helium and argon/helium estimates were, and not realistic for the thruster operating conditions.

There is almost no variation between the helium, argon/helium mix, and water vapor/helium mix constant line ratio curves for singlet-singlet ratios 492.2/667.8, 492.2/728.1, 504.8/667.8, 504.8/728.1, and 667.8/728.1. The 492.2/501.6, 501.6/504.8, 501.6/667.8, and 501.6/728.1 curves, shown in red, cyan, dark purple, and magenta in Figs. 7.5, 7.8, and 7.11, shift to the right on the plot from the helium tests to the argon/helium tests. As the measured n_e increases, these ratios from the CGS-CRM estimate higher n_e values for a constant T_e value. Since these line ratio curves for the water vapor test fall in between the helium and argon/helium mix tests, it can be assumed that n_e for water vapor/helium falls in between n_e for helium and argon/helium, which is what the CGS-CRM predicted using the least squares analysis. These ratios may be better predictors of n_e than the other singlet-singlet ratios. All of these ratios depend on the 501.6 nm line, suggesting that the accuracy of the photo-excitation is critical to determining n_e.

The CGS-CRM is a less reliable predictor of T_e. The constant line ratio curves on the singlet-triplet plots in Figs. 7.4, 7.7, 7.10 show a shift toward higher T_e from the helium to the argon/helium plots even though the LPs measured a lower T_e for the argon/helium mix. Most of the curves converge around 4 to 5 eV for n_e between 10^{16} and $10^{19}\,\mathrm{m}^{-3}$ with a discontinuity around $10^{17}\,\mathrm{m}^{-3}$. This estimate is 5 eV lower than the measured T_e for helium, but only 1 eV lower than the measured T_e for the argon/helium mix. The difference in T_e measurements between the helium and mixed gas tests of around 4 eV is not reflected in the line ratio curves from the

CGS-CRM. Of the line ratios that returned the closest helium T_e estimates from the corona model, the 728.1/471.3 and 728.1/706.5 ratios give the closest prediction, 5 eV lower. The water vapor/helium constant singlet-triplet line ratio curves fall in between the curves for the helium and argon/helium mixed gas, as was the case with the singlet-singlet line ratios. It may therefore be assumed that the value of T_e for the water vapor / helium mix plasma is between 6 and 9 eV. This trend cannot be confirmed with the least squares analysis since the minimum predicted values of T_e were beyond the temperature range for both helium and the water vapor/vapor helium mix.

Chapter 8: Conclusion

The helium line ratio spectroscopy technique is an attractive diagnostic for the helicon thruster because it is non-invasive and unaffected by the RF, electric, and magnetic fields present in the experiment. Helium gas seeding of the main propellant is advantageous because this eliminates the need to develop a complicated model for large atoms or molecules to determine the electron density and temperature. This technique can be applied to any type of propellant for a range of conditions that satisfy the CGS-CRM assumptions, provided that the helium emission lines are unobscured. The addition of 17% helium to the argon does not appear to significantly affect the LP measurements or the argon emission line ratios, demonstrating that the performance of the thruster is not changed by adding enough helium gas to achieve measurable helium emission lines.

The CGS-CRM predicted the order of magnitude of the Langmuir probe measurement of electron density for the helium and argon/helium mix. In each case, the n_e estimate from the model was lower than the LP measurement. The shift in the constant line ratio curves from the lower density helium tests to the higher density argon/helium tests was in the direction of higher electron density, indicating that CGS-CRM is correctly modeling the electron density trend.

The emission line ratios that showed the most variation with density were those including the 501.6 nm line. The intensity of this line is increased substantially by photo-excitation from the ground state, indicating that this transition has a high impact on the density estimate. Increasing the accuracy of the photo-excitation transitions in the model may yield a better n_e estimate. Measuring the 396.5 nm helium line would allow a direct way of finding the photo-excitation rate for the 4^1P state, which was not included in the CGS-CRM. This emission line results from the 4^1P to 2^1S transition. The addition of this line in the analysis may allow for a better prediction of n_e.

The rate of metastable particle loss to the thruster walls has a significant impact on the model's n_e prediction since the number of metastables increases with electron density to first order. Allowing for a higher metastable diffusion rate would be one way of increasing the n_e estimate from the CGS-CRM. A diffusion coefficient for 300 K was used in the model, but if the temperature of the bulk plasma in the thruster is higher, the metastable diffusion rate would also increase. Measuring the temperature as well as the gas pressure in the thruster would allow for a more accurate calculation of metastable diffusion.

The CGS-CRM T_e predictions do not match those measured by the LPs for helium and the argon/helium mix. The argon/helium gas results from the single and triple LPs are consistent with each other for T_e, corroborating the measurement. The CGS-CRM estimates T_e to be only about 1 eV lower than the LP measurement of 5 to 6 eV for the argon/helium mix, but the T_e estimate is around 5 eV lower than the helium LP measurement. The small changes in the constant line ratio curves

between all three propellant tests does not reflect the increase of several eV between the helium and argon/helium tests.

One possible source of the discrepancy between the LP measurements and the model prediction may be the accuracy of the collisional cross sections. The variability in the available cross section data translates to discrepancies in the helium corona model estimates between 1 and 12 eV. The cross sections included in the corona model are from the ground state only. If there are similar uncertainties in the cross sections for excitations from higher states, the error in the T_e prediction from the CGS-CRM could be on the order of the expected value of T_e. Cross section uncertainties may make finding an accurate T_e for low temperature helicon plasma difficult.

Chapter A: Neutral Helium Energy Levels

Table A.1: Neutral helium energy levels used in the CGS-CRM.

Level	Energy (eV)	n	L	2S+1	J
1	0.0000000	1	S	1	0
2	19.81961467579	2	S	3	1
3	20.6157749605	2	S	1	0
4	20.96408703092	2	P	3	4
5	21.2180228438	2	P	1	1
6	22.718466552	3	S	3	1
7	22.920317489	3	S	1	0
8	23.0070732743	3	P	3	4
9	23.07365083636	3	D	3	7
10	23.07407492587	3	D	1	2
11	23.0870186592	3	P	1	1
12	23.5939588380	4	S	3	1
13	23.6735707147	4	S	1	0
14	23.7078913522	4	P	3	4
15	23.73609031338	4	D	3	7
16	23.73633515877	4	D	1	2
17	23.737006930976	4	F	3	10
18	23.737009846100	4	F	1	3
19	23.7420701927	4	P	1	1
20	23.9719715402	5	S	3	1
21	24.0112151115	5	S	1	0
22	24.0282251854	5	P	3	4
23	24.042662363158	5	D	3	7
24	24.042803533268	5	D	1	2
25	24.043154205615	5	F	3	24
26	24.043155769890	5	F	1	8
27	24.0458005280	5	P	1	1
28	24.1689983436	6	S	3	1

Level	Energy (eV)	n	L	2S+1	J
29	24.1911603953	6	S	1	0
30	24.20081557465	6	P	3	4
31	24.209163230277	6	D	3	7
32	24.209249913835	6	D	1	2
33	24.2094549475880	6	F	3	40
34	24.2094558858411	6	F	1	13
35	24.21100279720	6	P	1	1
36	24.2845661562	7	S	3	1
37	24.2982860253	7	S	1	0
38	24.30428932074	7	P	3	4
39	24.309541016382	7	D	3	7
40	24.309597500413	7	D	1	2
41	24.3097274103799	7	F	3	58
42	24.3097280162896	7	F	1	18
43	24.31070829795	7	P	1	1
44	24.35810426286	8	S	3	1
45	24.36718019651	8	S	1	0
46	24.37116599948	8	P	3	4
47	24.374680998653	8	D	3	7
48	24.374719663112	8	D	1	2
49	24.3748070357373	8	F	3	80
50	24.3748074489121	8	F	1	25
51	24.37546681602	8	P	1	1
52	24.40777549754	9	S	3	1
53	24.41408819584	9	S	1	0
54	24.41686900426	9	P	3	4
55	24.419335683323	9	D	3	7
56	24.41936323553	9	D	1	2
57	24.4194247647087	9	F	3	80
58	24.4194250586257	9	F	1	25
59	24.41988943262	9	P	1	1
60	24.44289351540	10	S	3	1
61	24.44746013717	10	S	1	0
62	24.44947700985	10	P	3	4
63	24.451273930039	10	D	3	7
64	24.4512942224546	10	D	1	2
65	24.4513391627618	10	F	3	80
66	24.4513393790593	10	F	1	25
67	24.45167857741	10	P	1	1

Level	Energy (eV)	n	L	2S+1	J
68	24.475208	11	P	1	1
69	24.493108	12	P	1	1
70	24.507043	13	P	1	1
71	24.518101	14	P	1	1
72	24.527024	15	P	1	1

Chapter B: Neutral Helium Emission Lines

Table B.1: Neutral helium emission line transitions used in the CGS-CRM.

λ_{ij} (nm)	i	j	A_{ji} (s^{-1})	f_{ij}	g_i	g_j	Trans. type
50.55006682	1^1S	15^1P	0	0	1	3	A
50.56846377	1^1S	14^1P	0	0	1	3	A
50.59128113	1^1S	13^1P	0	0	1	3	A
50.62006431	1^1S	12^1P	0	0	1	3	A
50.65708541	1^1S	11^1P	0	0	1	3	A
50.70583184	1^1S	10^1P	15929000	0.001841935	1	3	A
50.77183931	1^1S	9^1P	21826000	0.002530404	1	3	A
50.8643675	1^1S	9^1P	31031000	0.003610713	1	3	A
50.99985928	1^1S	7^1P	46224000	0.005407237	1	3	A
51.01332879	1^1S	7^3P	0.0107	3.75701E-12	1	9	S
51.20988637	1^1S	6^1P	73174000	0.008630468	1	3	A
51.21359425	1^1S	6^1D	264.8	5.20604E-08	1	5	F
51.23144294	1^1S	6^3P	0.0153	5.41821E-12	1	9	S
51.56171452	1^1S	5^1P	125820000	0.01504438	1	3	A
51.56814181	1^1S	5^1D	431.36	8.59848E-08	1	5	F
51.59942911	1^1S	5^3P	0.0264	9.48385E-12	1	9	S
52.22133926	1^1S	4^1P	243560000	0.029872522	1	3	A
52.23395667	1^1S	4^1D	748.48	1.53075E-07	1	5	F
52.29662494	1^1S	4^3P	0.052	1.91885E-11	1	9	S
53.70302335	1^1S	3^1P	566340000	0.073458935	1	3	A
53.73314883	1^1S	3^1D	1299	2.81133E-07	1	5	F
53.88963157	1^1S	3^3P	0.121	4.74119E-11	1	9	S
58.43347004	1^1S	2^1P	1798900000	0.276248732	1	3	A
59.14126861	1^1S	2^3P	66.3543	3.13142E-08	1	9	S
62.55634746	1^1S	2^3S	0.0001272	2.23872E-14	1	3	S
267.7925633	2^3S	10^3P	441740	0.001424734	3	9	A
269.6919974	2^3S	9^3P	602340	0.00197037	3	9	A
272.4000267	2^3S	8^3P	849960	0.002836499	3	9	A

λ_{ij} (nm)	i	j	A_{ji} (s^{-1})	f_{ij}	g_i	g_j	Trans. type
276.4621294	2^3S	7^3P	1250800	0.00429961	3	9	A
282.9915201	2^3S	6^3P	1938901	0.006983488	3	9	A
294.5966844	2^3S	5^3P	3200600	0.012492721	3	9	A
318.8668928	2^3S	4^3P	5636100	0.025773148	3	9	A
323.2205045	2^1S	10^1P	510150	0.002396987	1	3	A
325.9215019	2^1S	9^1P	696270	0.003326394	1	3	A
329.7724255	2^1S	8^1P	984320	0.004814319	1	3	A
335.5521166	2^1S	7^1P	1453700	0.007361472	1	3	A
344.8578945	2^1S	6^1P	2269100	0.012136792	1	3	A
345.0261149	2^1S	6^1D	3.9163	3.49461E-08	1	5	F
355.5423721	2^3P	10^3D	759710	0.00239954	9	15	A
356.3988706	2^3p	10^3S	483610	0.00030697	9	3	A
358.8287926	2^3p	9^3D	1810700	0.005825302	9	15	A
360.0333521	2^3p	9^3S	672430	0.000435572	9	3	A
361.4674812	2^1S	5^1P	3802200	0.022343095	1	3	A
361.7835906	2^1S	5^1D	8.2983	8.14152E-08	1	5	F
363.5269146	2^3P	8^3D	2606200	0.008605543	9	15	A
365.3024182	2^3P	8^3S	974410	0.000649792	9	3	A
370.6052176	2^3P	7^3D	3952800	0.013565172	9	15	A
373.3927109	2^3P	7^3S	1489500	0.001037766	9	3	A
382.0689025	2^3P	6^3D	6435100	0.023471243	9	15	A
383.4638535	2^1P	10^1D	964700	0.003544366	3	5	A
383.9191133	2^1P	10^1S	374250	0.000275657	3	1	A
386.8571019	2^3P	6^3S	2446500	0.001829674	9	3	A
387.2886199	2^1P	9^1D	1338600	0.005016695	3	5	A
387.9278318	2^1P	9^1S	517530	0.000389193	3	1	A
388.9753118	2^3S	3^3P	9474700	0.064473235	3	9	A
392.7658477	2^1P	8^1D	1937100	0.007466497	3	5	A
393.706177	2^1P	8^1S	744750	0.000576876	3	1	A
396.5852903	2^1S	4^1P	6950700	0.049166768	1	3	A
397.3141434	2^1S	4^1D	22.842	2.70284E-07	1	5	F
401.0392243	2^1P	7^1D	2961200	0.011899778	3	5	A
402.5119378	2^1P	7^1S	1128100	0.00091334	3	1	A
402.7326176	2^3P	5^3D	11600000	0.047009866	9	15	A
412.1975755	2^3P	5^3S	4452700	0.003780609	9	3	A
414.2502528	2^1P	6^1P	3.069	7.89535E-09	3	3	F
414.4930068	2^1P	6^1D	4881200	0.020953589	3	5	A
417.0149146	2^1P	6^1S	1829800	0.001590136	3	1	A
438.4512648	2^1P	5^1P	5.317	1.53235E-08	3	3	F

λ_{ij} (nm)	i	j	A_{ji} (s^{-1})	f_{ij}	g_i	g_j	Trans. type
438.9164464	2^1P	5^1D	8988900	0.043268085	3	5	A
443.8801856	2^1P	5^1S	3268900	0.003218552	3	1	A
447.2731724	2^3P	4^3D	2457800	0.01228541	9	15	A
471.4460602	2^3P	4^3S	9520600	0.0105744	9	3	A
491.212141	2^1P	4^1P	10.28	3.7186E-08	3	3	F
492.198928	2^1P	4^1F	62.19	5.2702E-07	3	7	F
492.3307942	2^1P	4^1D	19863000	0.120297404	3	5	A
501.7079873	2^1S	3^1P	13372000	0.151379935	1	3	A
504.3496398	2^1S	3^1D	102.2000	1.94865E-06	1	5	F
504.9148978	2^1P	4^1S	6771200	0.008626397	3	1	A
587.6065475	2^3P	3^1D	16630.0000	4.78235E-05	9	5	S
587.7246751	2^3P	3^1D	70702000	0.610206684	9	15	A
663.3737176	2^1P	3^1P	23.7490	1.56679E-07	3	3	F
667.9999522	2^1P	3^1D	63705000	0.710270529	3	5	A
668.1526185	2^1P	3^3D	15100	0.000505297	3	15	S
706.712936	2^3P	3^3S	27852000	0.069513615	9	3	A
716.2537329	3^3S	10^3P	95686.0000	0.002207761	3	9	A
728.3361348	2^1P	3^1S	18299000	0.048508571	3	1	A
730.0052473	3^3S	9^3P	129130	0.003094917	3	9	A
750.192483	3^3S	8^3P	179420	0.004541363	3	9	A
781.8292981	3^3S	7^3P	257480	0.007078436	3	9	A
809.6344563	3^1S	10^1P	137910	0.004065778	1	3	A
826.7977455	3^1S	9^1P	187220	0.005755999	1	3	A
836.4040339	3^3S	6^3P	381260	0.011995639	3	9	A
852.0381236	3^1S	8^1P	262520	0.008571372	1	3	A
858.4975344	3^3P	10^3D	419270	0.007720924	9	15	A
863.5083046	3^3P	10^3S	274710	0.001023611	9	3	A
877.912415	3^3P	9^3D	577570	0.011122551	9	15	A
885.1579455	3^3P	9^3S	383760	0.001502549	9	3	A
886.610026	2^3S	2^1P	1.4420	1.69934E-08	3	3	S
891.7224526	3^1S	7^1P	382600	0.013682778	1	3	A
899.9441193	3^3D	10^1F	75367	0.003111286	15	51	S
899.9442606	3^3D	10^3F	335040	0.043662758	15	161	A
899.9995759	3^1D	10^1P	12389	9.02653E-05	5	3	A
900.2212315	3^1D	10^1F	284060	0.035201196	5	51	A
900.2213729	3^1D	10^3F	75160	0.029402885	5	161	S
901.1623169	3^3D	10^3P	26573	0.000194109	15	9	A
906.577727	3^3P	8^3D	827010	0.016983151	9	15	A
908.7919886	3^1P	10^1D	368070	0.007595508	3	5	A

λ_{ij} (nm)	i	j	A_{ji} (s^{-1})	f_{ij}	g_i	g_j	Trans. type
911.3532057	3^1P	10^1S	220000	0.000913111	3	1	A
917.7011576	3^3P	8^3S	559950	0.002356564	9	3	A
921.2582387	3^1D	9^1P	17331	0.000132308	5	3	A
921.2858157	3^3D	9^1F	109800	0.004750274	15	51	S
921.286017	3^3D	9^3F	473810	0.064710754	15	161	A
921.5762291	3^1D	9^1F	399610	0.051897652	5	51	A
921.5764304	3^1D	9^3F	109500	0.044893284	5	161	S
923.0389611	3^3D	9^3P	37167	0.000284838	15	9	A
930.5721089	3^1P	9^1D	510300	0.011041372	3	5	A
934.2710898	3^1P	9^1S	305620	0.001333076	3	1	A
946.6192248	3^3S	5^3P	568680	0.022918623	3	9	A
951.9181644	3^3P	7^3D	1243900	0.028163207	9	15	A
952.7051087	3^1D	8^1P	25364	0.000207078	5	3	A
952.8773786	3^3D	8^1F	170140	0.007874229	15	51	S
952.8776812	3^3D	8^3F	704570	0.102939425	15	161	A
953.1880538	3^1D	8^1F	589760	0.08193724	5	51	A
953.1883566	3^1D	8^3F	169700	0.074429283	5	161	S
955.5516093	3^3D	8^3P	54371	0.000446556	15	9	A
960.608054	3^1S	6^1P	582860	0.024189485	1	3	A
961.9144327	3^1S	6^1D	1.2600	8.73901E-08	1	5	F
962.8343058	3^1P	8^1D	737440	0.017081548	3	5	A
968.5048848	3^1P	8^1S	442710	0.002075154	3	1	A
970.5280708	3^3P	7^3S	865100	0.00407202	9	3	A
1002.595215	3^1D	7^1P	39418	0.000356407	5	3	A
1003.046349	3^3D	7^1F	287330	0.010690108	15	37	S
1003.04684	3^3D	7^3F	1122500	0.132060228	15	117	A
1003.390605	3^1D	7^1F	928920	0.103752544	5	37	A
1003.391097	3^1D	7^3F	286600	0.101223463	5	117	S
1007.479221	3^3D	7^3P	84429	0.000770839	15	9	A
1014.120857	3^1P	7^1D	1124800	0.028903614	3	5	A
1023.59127	3^1P	7^1S	677310	0.003546239	3	1	A
1031.405924	3^3P	6^3D	1994500	0.053014015	9	15	A
1067.059086	3^3P	6^3S	1447100	0.008233849	9	3	A
1083.331281	2^3S	2^3P	10217000	0.539281941	3	9	A
1090.520105	3^1D	6^1P	66614	0.000712579	5	3	A
1091.59816	3^3D	6^1F	552950	0.016462996	15	25	S
1091.599062	3^3D	6^3F	1980100	0.186293596	15	79	A
1092.005896	3^1D	6^1F	1608300	0.143759216	5	25	A
1092.006798	3^1D	6^3F	321920	0.090929414	5	79	S

λ_{ij} (nm)	i	j	A_{ji} (s^{-1})	f_{ij}	g_i	g_j	Trans. type
1099.965835	3^3D	6^3P	427580	0.004653457	15	9	A
1101.609406	3^1S	5^1P	924960	0.050483347	1	3	A
1103.078469	3^1P	6^1P	0.8465	1.54415E-08	3	3	F
1104.550661	3^1S	5^1D	2.5140	2.29909E-07	1	5	F
1104.801436	3^1P	6^1D	1845700	0.056289447	3	5	A
1109.890636	3^1D	6^1S	0.4515	1.66762E-09	5	1	F
1122.901763	3^1P	6^1S	1116800	0.00703698	3	1	A
1197.071044	3^3P	5^1D	339.0000	4.04591E-06	9	5	S
1197.234227	3^3P	5^3D	3478100	0.124565485	9	15	A
1253.094426	3^3S	4^3P	709330	0.050094015	3	9	A
1275.91853	3^1D	5^1P	127540	0.001867636	5	3	A
1278.841045	3^3D	5^1F	1321700	0.032405198	15	15	S
1278.843108	3^3D	5^3F	4133900	0.317577527	15	47	A
1279.400692	3^1D	5^1F	3247500	0.23907394	5	15	A
1279.402757	3^1D	5^3F	770070	0.177632032	5	47	S
1284.946554	3^3P	5^3S	2731600	0.022537962	9	3	A
1293.143668	3^1P	5^1P	1.4230	3.56736E-08	3	3	F
1297.198497	3^1P	5^1D	3361500	0.141332943	3	5	A
1297.390123	3^1P	5^3D	330.3	4.16743E-05	3	15	S
1298.843514	3^3D	5^3P	818770	0.012424402	15	9	A
1323.006655	3^1D	5^1S	0.7417	3.89231E-09	5	1	F
1341.535881	3^1P	5^1S	2057200	0.018501567	3	1	A
1449.230119	4^3S	10^3P	34680	0.003275848	3	9	A
1506.656198	4^3S	9^3P	46126	0.004709166	3	9	A
1508.778367	3^1S	4^1P	1405700	0.143917451	1	3	A
1519.382175	3^1S	4^1D	5.6132	9.71322E-07	1	5	F
1593.40724	4^1S	10^1P	57048	0.006514242	1	3	A
1595.253831	4^3S	8^3P	62580	0.007162507	3	9	A
1661.277779	4^1S	9^1P	76907	0.009545975	1	3	A
1667.839332	4^3P	10^3D	179770	0.01249462	9	15	A
1686.855855	4^3P	10^3S	168710	0.002398966	9	3	A
1700.133695	3^3P	4^1D	818.6	1.97067E-05	9	5	S
1700.704696	3^3P	4^3D	6608700	0.477607647	9	15	A
1733.213265	4^1D	10^1P	14055	0.000379782	5	3	A
1733.441904	4^3D	10^1F	46897	0.007182758	15	51	S
1733.442428	4^3D	10^3F	205060	0.099147799	15	161	A
1734.035502	4^1D	10^1F	173470	0.079760741	5	51	A
1734.036027	4^1D	10^3F	46800	0.067930783	5	161	S
1735.666223	4^3F	10^1F	6150	0.000674539	21	51	S

λ_{ij} (nm)	i	j	A_{ji} (s^{-1})	f_{ij}	g_i	g_j	Trans. type
1735.666749	4^3F	10^3F	457300	0.15833945	21	161	F
1735.673306	4^1F	10^1F	148670	0.048919286	7	51	F
1735.673832	4^1F	10^3F	7159	0.00743644	7	161	S
1735.77595	4^3F	10^1D	1098	1.18083E-05	21	5	S
1735.783034	4^1F	10^1D	1978.6	6.38366E-05	7	5	A
1735.825264	4^3F	10^3D	2733.2	8.81869E-05	21	15	A
1735.832348	4^1F	10^3D	462.07	4.47265E-05	7	15	S
1737.967232	4^3D	10^3P	27341	0.000742844	15	9	A
1742.712181	4^3P	9^3D	246580	0.018711413	9	15	A
1745.444877	4^3S	7^3P	85957	0.01177778	3	9	A
1748.167927	4^1P	10^1D	17528	0.001338431	3	5	A
1757.669941	4^1P	10^1S	139220	0.002149333	3	1	A
1766.419132	4^1S	8^1P	106610	0.014960819	1	3	A
1771.497055	4^3P	9^3S	237470	0.003724063	9	3	A
1813.817497	4^1D	9^1P	19866	0.000587892	5	3	A
1814.400205	4^3D	9^1F	68164	0.011437966	15	51	S
1814.400986	4^3D	9^3F	289440	0.153323377	15	161	A
1815.050555	4^1D	9^1F	243560	0.122696522	5	51	A
1815.051336	4^1D	9^3F	68040	0.108204834	5	161	S
1816.837291	4^3F	9^1F	9116	0.001095559	21	51	S
1816.838073	4^3F	9^3F	677320	0.256969505	21	161	F
1816.845052	4^1F	9^1F	220190	0.079387874	7	51	F
1816.845834	4^1F	9^3F	10611	0.012077275	7	161	S
1817.0019	4^3F	9^1D	1590	1.87373E-05	21	5	S
1817.009663	4^1F	9^1D	2866.1	0.000101327	7	5	A
1817.07527	4^3F	9^3D	3958.2	0.000139947	21	15	A
1817.083034	4^1F	9^3D	668.92	7.09522E-05	7	15	S
1821.21256	4^3D	9^3P	38633	0.001152603	15	9	A
1830.585321	4^1P	9^1D	242890	0.020337005	3	5	A
1844.954594	4^1P	9^1S	194770	0.003312995	3	1	A
1856.065101	3^1D	4^1P	296300	0.009181592	5	3	A
1859.421046	4^3P	8^3D	350620	0.030289324	9	15	A
1869.037254	3^3D	4^1F	4855100	0.118655955	15	7	S
1869.045468	3^3D	4^3F	12220000	0.895957969	15	21	A
1870.232906	3^1D	4^1F	8978000	0.659094499	5	7	A
1870.24113	3^1D	4^3F	2830600	0.623406982	5	21	S
1892.740706	3^1P	4^1P	2.5290	1.35825E-07	3	3	F
1906.825721	4^3P	8^3S	350520	0.006368867	9	3	A
1909.458181	3^1P	4^1D	7115900	0.648257501	3	5	A

λ_{ij} (nm)	i	j	A_{ji} (s^{-1})	f_{ij}	g_i	g_j	Trans. type
1910.178474	3^1P	4^3D	894.4	0.000244624	3	15	S
1939.886232	4^1D	8^1P	29506	0.000998764	5	3	A
1941.145201	4^3D	8^1F	105230	0.020210786	15	51	S
1941.146456	4^3D	8^3F	429010	0.260116141	15	161	A
1941.889603	4^1D	8^1F	358290	0.206601083	5	51	A
1941.89086	4^1D	8^3F	105100	0.191318464	5	161	S
1943.934925	4^3F	8^1F	14525	0.001998385	21	51	S
1943.936185	4^3F	8^3F	1077900	0.468163685	21	161	F
1943.94381	4^1F	8^1F	350420	0.144636232	7	51	F
1943.94507	4^1F	8^3F	16900	0.022020703	7	161	S
1944.202522	4^3F	8^1D	2445	3.29884E-05	21	5	S
1944.211409	4^1F	8^1D	4409.4	0.000178479	7	5	A
1944.320406	4^3F	8^3D	6087.4	0.000246427	21	15	A
1944.329295	4^1F	8^3D	1028.6	0.000124919	7	15	S
1945.957568	4^1S	7^1P	152070	0.025898833	1	3	A
1952.275499	4^3D	8^3P	57358	0.001966419	15	9	A
1954.846263	3^3D	4^3P	645290	0.022180946	15	9	A
1956.15426	3^1D	4^3P	57.84	5.97249E-06	5	9	S
1959.762491	4^1P	8^1D	350630	0.033647544	3	5	A
1983.399233	4^1P	8^1S	285120	0.005604997	3	1	A
2043.056668	4^3S	6^3P	115240	0.021633859	3	9	A
2058.691673	2^1S	2^1P	1974600	0.376384444	1	3	A
2060.738626	4^3P	7^3D	520620	0.055241324	9	15	A
2068.142471	3^1D	4^1S	1.3064	1.67539E-08	5	1	F
2112.579997	3^3P	4^3S	6511900	0.145231712	9	3	A
2113.781191	3^1P	4^1S	4592500	0.102540783	3	1	A
2149.985908	4^3P	7^3S	552110	0.012753349	9	3	A
2158.601469	4^1D	7^1P	46870	0.001964445	5	3	A
2161.36892	4^3D	7^1F	176580	0.030504116	15	37	S
2161.371203	4^3D	7^3F	679310	0.37108209	15	117	A
2162.291849	4^1D	7^1F	560850	0.290908043	5	37	A
2162.294134	4^1D	7^3F	102850	0.168693503	5	117	S
2164.828106	4^3F	7^1F	25784	0.003191745	21	37	S
2164.830396	4^3F	7^3F	1910800	0.74795973	21	117	F
2164.839125	4^1F	7^1F	621140	0.230671054	7	37	F
2164.841415	4^1F	7^3F	30000	0.035229779	7	117	S
2165.321555	4^3F	7^1D	4095	6.85327E-05	21	5	S
2165.332579	4^1F	7^1D	7389.2	0.000370994	7	5	A
2165.535177	4^3F	7^3D	10208	0.000512616	21	15	A

λ_{ij} (nm)	i	j	A_{ji} (s^{-1})	f_{ij}	g_i	g_j	Trans. type
2165.546203	4^1F	7^3D	1721.6	0.000259364	7	15	S
2182.057142	4^3D	7^3P	91121	0.003902569	15	9	A
2184.639726	4^1P	7^1D	533410	0.063608949	3	5	A
2184.857178	4^1P	7^3D	43.3	1.54936E-05	3	15	S
2229.06762	4^1P	7^1S	443670	0.011016254	3	1	A
2306.975602	4^1S	6^1P	220450	0.05276744	1	3	A
2314.524634	4^1S	6^1D	0.4302	1.72748E-07	1	5	F
2472.966051	4^3P	6^1D	69.9	3.56032E-06	9	5	S
2473.393694	4^3P	6^3D	810930	0.123955921	9	15	A
2596.499477	5^3S	10^3P	16011	0.004854727	3	9	A
2612.022817	4^1D	6^1P	81901	0.005026238	5	3	A
2619.207594	4^3D	6^1F	334640	0.057360788	15	25	S
2619.212786	4^3D	6^3F	1180800	0.639591087	15	79	A
2620.563064	4^1D	6^1F	956840	0.49254648	5	25	A
2620.568261	4^1D	6^3F	195020	0.317231171	5	79	S
2624.289226	4^3F	6^1F	54890	0.006746616	21	25	S
2624.294438	4^3F	6^3F	4060500	1.577106761	21	79	F
2624.305419	4^1F	6^1F	1319900	0.486698955	7	25	F
2624.310631	4^1F	6^3F	63850	0.074399342	7	79	S
2625.433828	4^3F	6^1D	7805	0.000192032	21	5	S
2625.450035	4^1F	6^1D	14102	0.0010409	7	5	A
2625.915833	4^3F	6^3D	19466	0.001437338	21	15	A
2625.932046	4^1F	6^3D	3279.9	0.000726557	7	15	S
2643.96779	4^1P	6^1P	0.2977	3.11958E-08	3	3	F
2653.888099	4^1P	6^1D	868540	0.152845427	3	5	A
2654.38061	4^1P	6^3D	75.7500	4.00062E-05	3	15	S
2667.904686	4^3D	6^3P	159750	0.010227781	15	9	A
2688.839522	4^3P	6^3S	959110	0.034651784	9	3	A
2725.976051	4^1D	6^1S	0.2463	5.48655E-09	5	1	F
2760.787688	4^1P	6^1S	754430	0.028735078	3	1	A
2786.805505	5^3S	9^3P	20818	0.00727147	3	9	A
2814.859343	5^1S	10^1P	29201	0.010405933	1	3	A
2855.028278	4^3S	5^3P	120680	0.044241113	3	9	A
2930.732493	5^3P	10^3D	92978	0.019954	9	15	A
2989.962369	5^3P	10^3S	113840	0.005085735	9	3	A
3032.326673	5^1D	10^1P	13169	0.001089193	5	3	A
3033.796015	5^3D	10^1F	28255	0.013255486	15	51	S
3033.79762	5^3D	10^3F	122930	0.182059931	15	161	A
3033.81602	5^1S	9^1P	38969	0.016131237	1	3	A

λ_{ij} (nm)	i	j	A_{ji} (s^{-1})	f_{ij}	g_i	g_j	Trans. type
3034.844347	5^1D	10^1F	103980	0.146443969	5	51	A
3034.845954	5^1D	10^3F	28220	0.125468541	5	161	S
3037.451585	5^3F	10^1F	9281.5	0.001393022	47	51	S
3037.453195	5^3F	10^3F	639430	0.302962501	47	161	F
3037.463226	5^1F	10^1F	207310	0.097492204	15	51	F
3037.464835	5^1F	10^3F	10351	0.015366965	15	161	S
3037.787649	5^3F	10^1D	1396	2.05457E-05	47	5	S
3037.799292	5^1F	10^1D	3338.2	0.000153942	15	5	A
3037.938693	5^3F	10^3D	4303.8	0.000190043	47	15	A
3037.950337	5^1F	10^3D	586.43	8.11384E-05	15	15	S
3047.684522	5^3D	10^3P	24069	0.002010935	15	9	A
3057.61278	5^1P	10^1D	97739	0.022831281	3	5	A
3086.799553	5^1P	10^1S	95913	0.004566903	3	1	A
3105.8615	5^3S	8^3P	27073	0.011745472	3	9	A
3170.057334	5^3P	9^3D	126810	0.031840886	9	15	A
3266.609623	5^3P	9^3S	162190	0.008648603	9	3	A
3287.958272	5^1D	9^1P	18869	0.001834853	5	3	A
3290.77883	5^3D	9^1F	40966	0.022612497	15	51	S
3290.781397	5^3D	9^3F	173090	0.30161527	15	161	A
3292.014891	5^1D	9^3F	40930	0.214126225	5	161	S
3295.080372	5^3F	9^1F	13914	0.002457565	47	51	S
3295.082946	5^3F	9^3F	974580	0.543409063	47	161	F
3295.09407	5^1F	9^1F	316200	0.174994774	15	51	F
3295.096644	5^1F	9^3F	15538	0.027146554	15	161	S
3295.621858	5^3F	9^1D	2062	3.57178E-05	47	5	S
3295.635561	5^1F	9^1D	4934.7	0.000267835	15	5	A
3295.863235	5^3F	9^3D	6360.7	0.000330587	47	15	A
3295.876941	5^1F	9^3D	866.26	0.000141071	15	15	S
3313.256811	5^3D	9^3P	34487	0.00340538	15	9	A
3318.96808	5^1P	9^1D	135420	0.037272315	3	5	A
3330.852763	4^1S	5^1P	293230	0.146315113	1	3	A
3357.888681	4^1S	5^1D	0.7019	5.93243E-07	1	5	F
3366.506159	5^1P	9^1S	135650	0.007682561	3	1	A
3403.807551	5^1S	8^1P	52980	0.027606533	1	3	A
3559.574323	2^1S	2^3P	0.0297	5.07059E-08	1	9	S
3578.246644	5^3P	8^1D	10.1	1.07706E-06	9	5	S
3578.645977	5^3P	8^3D	178340	0.057066817	9	15	A
3701.993455	4^3P	5^1D	123.98	1.41514E-05	9	5	S
3703.554554	4^3P	5^3D	1279200	0.438402836	9	15	A

λ_{ij} (nm)	i	j	A_{ji} (s^{-1})	f_{ij}	g_i	g_j	Trans. type
3727.019982	5^1D	8^1P	28583	0.00357134	5	3	A
3730.894869	5^3S	7^3P	33712	0.021104762	3	9	A
3732.834702	5^3D	8^1F	62917	0.044686167	15	51	S
3732.839345	5^3D	8^3F	255280	0.57237238	15	161	A
3734.421926	5^1D	8^1F	213190	0.454634545	5	51	A
3734.426574	5^1D	8^3F	62870	0.423248906	5	161	S
3738.370504	5^3F	8^1F	22588	0.005135272	47	51	S
3738.375161	5^3F	8^3F	1625700	1.166763544	47	161	F
3738.388136	5^1F	8^1F	527740	0.375938125	15	51	F
3738.392793	5^1F	8^3F	25267	0.056820732	15	161	S
3739.360281	5^3F	8^1D	3268	7.28782E-05	47	5	S
3739.377922	5^1F	8^1D	7824.8	0.000546763	15	5	A
3739.796385	5^3F	8^3D	10083	0.000674726	47	15	A
3739.814031	5^1F	8^3D	1372.8	0.000287843	15	15	S
3758.476323	5^3P	8^3S	244210	0.017239096	9	3	A
3769.445343	5^1P	8^1D	195260	0.069321124	3	5	A
3769.888494	5^1P	8^3D	15.18	1.61714E-05	3	15	S
3774.213023	5^3D	8^3P	52292	0.006700203	15	9	A
3857.875353	5^1P	8^1S	202030	0.015025871	3	1	A
4003.234778	4^3D	5^1P	20.05	9.63419E-07	15	3	S
4006.40209	4^1D	5^1P	163300	0.023577359	5	3	A
4037.714682	4^3D	5^1F	756590	0.184918564	15	15	S
4037.735252	4^3D	5^3F	2333600	1.787134983	15	47	A
4040.936812	4^1D	5^1F	1829400	1.343515591	5	15	A
4040.957414	4^1D	5^3F	441430	1.015796958	5	47	S
4049.803705	4^3F	5^1F	170450	0.029935435	21	15	S
4049.824398	4^3F	5^3F	12577000	6.921124653	21	47	F
4049.842267	4^1F	5^1F	4087900	2.15386442	7	15	F
4049.862961	4^1F	5^3F	198220	0.327247704	7	47	S
4054.468535	4^3F	5^1D	18330	0.001075548	21	5	S
4054.507186	4^1F	5^1D	33200	0.005844332	7	5	A
4056.341133	4^3F	5^3D	45778	0.00806578	21	15	A
4056.37982	4^1F	5^3D	7702.3	0.00407136	7	15	S
4082.050945	4^1P	5^1P	0.4519	1.12888E-07	3	3	F
4122.731121	4^1P	5^1D	1525400	0.647815264	3	5	A
4124.66732	4^1P	5^3D	150.7	0.000192181	3	15	S
4139.802701	5^1S	7^1P	72156	0.055616244	1	3	A
4244.076353	4^3D	5^3P	327100	0.052996457	15	9	A
4247.636401	4^1D	5^3P	15.51	7.5514E-06	5	9	S

λ_{ij} (nm)	i	j	A_{ji} (s^{-1})	f_{ij}	g_i	g_j	Trans. type
4295.959194	3^3S	3^3P	1073700	0.89119587	3	9	A
4406.413268	5^3P	7^1D	20.71	3.34909E-06	9	5	S
4407.29801	5^3P	7^3D	258080	0.12525544	9	15	A
4420.452788	6^3S	10^3P	8432.3	0.007410534	3	9	A
4510.487905	4^1D	5^1S	0.3811	2.32457E-08	5	1	F
4606.598957	4^1P	5^1S	1496100	0.158653202	3	1	A
4627.923298	5^1D	7^1P	46719	0.009000482	5	3	A
4642.464082	5^3D	7^1F	104230	0.08307091	15	37	S
4642.474615	5^3D	7^3F	399110	1.005854006	15	117	A
4644.919372	5^1D	7^1F	329550	0.788783936	5	37	A
4644.929916	5^1D	7^3F	60786	0.46007265	5	117	S
4651.029668	5^3F	7^1F	3141100	0.801922707	47	37	S
4651.04024	5^3F	7^3F	3141100	2.535821167	47	117	F
4651.056961	5^1F	7^1F	1021100	0.816828195	15	37	F
4651.067533	5^1F	7^3F	46600	0.117878465	15	117	S
4653.307951	5^3F	7^1D	5736	0.000198086	47	5	S
4653.33527	5^1F	7^1D	13745	0.001487308	15	5	A
4654.294627	5^3F	7^3D	17703	0.001834834	47	15	A
4654.321959	5^1F	7^3D	2409	0.000782345	15	15	S
4694.947817	4^3P	5^3S	2022600	0.22279167	9	3	A
4699.988369	5^1P	7^1D	295440	0.163064819	3	5	A
4700.994943	5^1P	7^3D	24.05	3.98394E-05	3	15	S
4738.971525	5^3D	7^3P	85943	0.017361155	15	9	A
4759.140771	6^1S	10^1P	13169	0.013414665	1	3	A
4836.69348	5^3P	7^3S	399760	0.046733023	9	3	A
4910.550172	5^1P	7^1S	324210	0.039067365	3	1	A
4950.294831	6^3P	10^3D	54294	0.033243855	9	15	A
5001.974412	6^3S	9^3P	10521	0.01183886	3	9	A
5114.257876	6^1D	10^1P	11910	0.002802057	5	3	A
5119.590465	6^3D	10^1F	17954	0.023986078	15	51	S
5119.595038	6^3D	10^3F	77923	0.328639804	15	161	A
5121.423607	6^1D	10^1F	65928	0.264423551	5	51	A
5121.428183	6^1D	10^3F	17940	0.22714812	5	161	S
5121.66742	6^3P	10^3S	83143	0.010898729	9	3	A
5125.76479	6^3F	10^1F	9568.4	0.002433035	79	51	S
5125.769374	6^3F	10^3F	718560	0.576804458	79	161	F
5125.784673	6^1F	10^1F	235400	0.189149851	25	51	F
5125.789257	6^1F	10^3F	10548	0.026756305	25	161	S
5126.721881	6^3F	10^1D	1443	3.59863E-05	79	5	S

λ_{ij} (nm)	i	j	A_{ji} (s^{-1})	f_{ij}	g_i	g_j	Trans. type
5126.741771	6^1F	10^1D	4084.5	0.000321885	25	5	A
5127.152094	6^3F	10^3D	5084	0.000380427	79	15	A
5127.171987	6^1F	10^3D	605.85	0.000143259	25	15	S
5159.265958	6^3D	10^3P	20847	0.004991365	15	9	A
5159.745925	6^1P	10^1D	60761	0.040418385	3	5	A
5160.181698	6^1P	10^3D	4.49	8.96179E-06	3	15	S
5243.409667	6^1P	10^1S	71005	0.009755374	3	1	A
5417.850219	5^3S	6^3P	31456	0.041526698	3	9	A
5420.574129	6^1S	9^1P	22206	0.029344778	1	3	A
5673.09985	6^3P	9^1D	4.0240	1.07864E-06	9	5	S
5673.815145	6^3P	9^3D	73352	0.059001049	9	15	A
5886.087802	6^1D	9^1P	17374	0.005414436	5	3	A
5896.660901	6^3D	9^1F	25918	0.045934752	15	51	S
5896.669144	6^3D	9^3F	109280	0.611416968	15	161	A
5899.092889	6^1D	9^1F	91988	0.489497502	5	51	A
5899.101139	6^1D	9^3F	25920	0.435422849	5	161	S
5904.853296	6^3F	9^1F	14565	0.004914965	79	51	S
5904.861561	6^3F	9^3F	1135400	1.209527584	79	161	F
5904.879682	6^1F	9^1F	376370	0.401343223	25	51	F
5904.887947	6^1F	9^3F	16096	0.054184593	25	161	S
5906.592419	6^3F	9^1D	2190	7.24953E-05	79	5	S
5906.61882	6^1F	9^1D	6201.9	0.000648756	25	5	A
5907.36781	6^3F	9^3D	7717.8	0.000766645	79	15	A
5907.394218	6^1F	9^3D	919.64	0.000288675	25	15	S
5950.47079	6^1P	9^1D	84180	0.074474739	3	5	A
5951.257745	6^1P	9^3D	6.3590	1.6882E-05	3	15	S
5969.22598	6^3D	9^3P	30467	0.009764852	15	9	A
5971.718206	6^1D	9^3P	1.9830	1.90828E-06	5	9	S
5990.738134	6^3P	9^3S	120880	0.021679164	9	3	A
6105.031236	6^1P	9^1S	102180	0.019031328	3	1	A
6132.745106	6^3S	8^3P	12413	0.020996964	3	9	A
6205.801413	5^1S	6^1P	88145	0.152673389	1	3	A
6260.731384	5^1S	6^1D	0.1397	4.10337E-07	1	5	F
6727.072759	6^1S	8^1P	28896	0.05881118	1	3	A
6849.023959	5^3P	6^1D	31.36	1.22521E-05	9	5	S
6852.30518	5^3P	6^3D	366070	0.429472089	9	15	A
7129.462643	6^3P	8^1D	7.732	3.27327E-06	9	5	S
7131.048104	6^3P	8^3D	100810	0.128087798	9	15	A
7365.091514	5^3D	6^1P	8.075	1.31334E-06	15	3	S

λ_{ij} (nm)	i	j	A_{ji} (s^{-1})	f_{ij}	g_i	g_j	Trans. type
7371.273055	5^3D	6^1P	83990	0.041049937	5	3	A
7433.398385	5^1D	6^1F	187730	0.25918264	15	25	S
7433.4402	5^3D	6^3F	659360	2.876648482	15	79	A
7437.516489	3^1S	3^1P	251650	0.626069771	1	3	A
7439.695168	5^1D	6^1F	534650	2.218188862	5	25	A
7439.737054	5^1D	6^3F	109610	1.437047421	5	79	S
7455.297471	6^3D	8^1P	2.306	3.84298E-07	15	3	S
7455.382895	5^3F	6^1F	95850	0.042483749	47	25	S
7455.424958	5^3F	6^3F	8182500	11.46063591	47	79	F
7455.453023	5^1F	6^1F	2668000	3.705367715	15	25	F
7455.495086	5^1F	6^3F	108800	0.477492293	15	79	S
7459.185473	6^1D	8^1P	26987	0.013506329	5	3	A
7464.628168	5^3F	6^1D	11710	0.001040625	47	5	S
7464.69847	5^1F	6^1D	28105	0.007825922	15	5	A
7468.525911	5^3F	6^3D	36181	0.009655892	47	15	A
7468.596286	5^1F	6^3D	4912	0.00410757	15	15	S
7484.974196	6^3D	8^1F	39380	0.11245633	15	51	S
7484.992866	6^3D	8^3F	159420	1.437172391	15	161	A
7488.893221	6^1D	8^1F	133210	1.142407219	5	51	A
7488.911911	6^1D	8^3F	22979	0.622118482	5	161	S
7498.179297	6^3F	8^1F	24309	0.013227278	79	51	S
7498.198033	6^3F	8^3F	2099000	3.605568062	79	161	F
7498.221844	6^1F	8^1F	684360	1.17673865	25	51	F
7498.24058	6^1F	8^3F	26988	0.146495395	25	161	S
7502.162202	6^3F	8^1D	3614	0.000192998	79	5	S
7502.204794	6^1F	8^1D	10240	0.001728051	25	5	A
7503.917779	6^3F	8^3D	12739	0.002041852	7	15	A
7503.960391	6^1F	8^3D	1517.1	0.000768414	25	15	S
7504.998014	5^1P	6^1P	0.1129	9.53078E-08	3	3	F
7518.260167	7^3S	10^3P	4727.8	0.012018872	3	9	A
7573.090868	6^1P	8^1D	120940	0.173306045	3	5	A
7574.879802	6^1P	8^3D	9.426	4.05413E-05	3	15	S
7585.484007	5^1P	6^1D	466030	0.670004748	3	5	A
7589.509018	5^1P	6^3D	40.82	0.000176246	3	15	S
7653.21919	6^3D	8^3P	47665	0.025112376	15	9	A
7657.316426	6^1D	8^3P	3.103	4.90971E-06	5	9	S
7839.503798	5^3D	6^3P	247360	0.136743451	15	9	A
7846.507718	5^1D	6^3P	5.936	9.86207E-06	5	9	S
7882.592933	6^3P	8^3S	189230	0.058756456	9	3	A

λ_{ij} (nm)	i	j	A_{ji} (s^{-1})	f_{ij}	g_i	g_j	Trans. type
7938.681958	6^1P	8^1S	156940	0.049426273	3	1	A
8063.627538	3^1S	3^1D	0.0012	6.08852E-09	1	5	F
8082.809009	7^1S	10^1P	10590	0.031116483	1	3	A
8357.16451	5^1D	6^1S	0.1201	2.51543E-08	5	1	F
8434.022864	7^3P	10^1D	1.844	1.09246E-06	9	5	S
8435.187249	7^3P	10^3D	34374	0.061110655	9	15	A
8529.470515	5^1P	6^1S	593210	0.215665172	3	1	A
8726.304223	7^1D	10^1P	10833	0.007420093	5	3	A
8743.702528	7^3D	10^1F	12042	0.046926369	15	51	S
8743.715865	7^3D	10^3F	52198	0.642139248	15	161	A
8747.186887	7^1D	10^1F	44184	0.516952542	5	51	A
8747.200235	7^1D	10^3F	12040	0.444702076	5	161	S
8755.211256	7^3F	10^1F	8408.4	0.004211915	117	51	S
8755.224629	7^3F	10^3F	670000	1.059492936	117	161	F
8755.248717	7^1F	10^1F	218000	0.345311136	37	51	F
8755.26209	7^1F	10^3F	9216.245	0.046085587	37	161	S
8758.00397	7^3F	10^1D	1440	7.07629E-05	117	5	S
8758.041455	7^1F	10^1D	4528.8	0.000703743	37	5	A
8759.259536	7^3F	10^3D	5526.3	0.000814936	117	15	A
8759.297032	7^1F	10^3D	604.12	0.000281708	37	15	S
8807.380029	5^3P	6^3S	776780	0.301105657	9	3	A
8819.109783	7^1P	10^1D	40864	0.079412302	3	5	A
8820.382932	7^1P	10^3D	3.024	1.7635E-05	3	15	S
8860.070032	7^3D	10^3D	18409	0.012998835	15	9	A
8863.647772	7^1D	10^3P	1.116	2.36598E-06	5	9	S
8945.20332	7^3P	10^3S	65217	0.026077662	9	3	A
9066.369485	7^1P	10^1S	56053	0.023024653	3	1	A
9164.26748	6^3S	7^3P	10673	0.040313633	3	9	A
9371.247258	7^3S	9^3P	5354	0.021146723	3	9	A
10195.78916	7^1S	9^1P	13311	0.062233223	1	3	A
10371.09539	6^1S	7^1P	33283	0.161005844	1	3	A
10774.31583	7^3P	9^1D	2.486	2.40357E-06	9	5	S
10776.89615	7^3P	9^3D	45472	0.131955915	9	15	A
10882.25526	4^3S	4^3P	228270	1.215784419	3	9	A
11235.70908	7^3D	9^1P	1.288	4.87523E-07	15	3	S
11241.46325	7^1D	9^1P	16163	0.018372471	5	3	A
11283.1916	7^3D	9^1F	17227	0.111789537	15	51	S
11283.22178	7^3D	9^3F	72520	1.485618585	15	161	A
11288.99451	7^1D	9^1F	61082	1.190344327	5	51	A

λ_{ij} (nm)	i	j	A_{ji} (s^{-1})	f_{ij}	g_i	g_j	Trans. type
11289.02473	7^1D	9^3F	10057	0.618708144	5	161	S
11302.36356	7^3F	9^1F	12810	0.010693519	117	51	S
11302.39384	7^3F	9^3F	1082500	2.852708885	117	161	F
11302.42599	7^1F	9^1F	352720.92	0.93109003	37	51	F
11302.45627	7^1F	9^3F	14084.23	0.117368511	37	161	S
11308.73691	7^3F	9^1D	2265	0.000185579	117	5	S
11308.79941	7^1F	9^1D	7126.2	0.001846324	37	5	A
11311.57958	7^3F	9^3D	8694.2	0.002138111	117	15	A
11311.64211	7^1F	9^3D	950.4	0.000739088	37	15	S
11397.50647	6^3P	7^1D	10.65	1.15225E-05	9	5	S
11403.42759	6^3P	7^3D	133520	0.433824979	9	15	A
11410.82706	7^1P	9^1D	564910	1.837853634	3	5	A
11413.7213	7^1P	9^3D	4.276	4.17552E-05	3	15	S
11551.90484	7^3D	9^3P	27700	0.033249635	15	9	A
11557.98751	7^1D	9^3P	1.68	6.05613E-06	5	9	S
11980.75666	7^3P	9^3S	98608	0.070730716	9	3	A
11993.07339	7^1P	9^1S	83180	0.059787075	3	1	A
12209.77769	6^3D	7^1P	3.83	1.71196E-06	15	3	S
12220.20943	6^1D	7^1P	45011	0.060461076	5	3	A
12328.79571	6^3D	7^1F	62215	0.34969993	15	37	S
12328.86999	6^3D	7^3F	237740	4.225635857	15	117	A
12339.43189	6^1D	7^1F	196520	3.319536651	5	37	A
12339.50631	6^1D	7^3F	36343	1.941247289	5	117	S
12364.663	6^3F	7^1F	47767	0.0512762	79	37	S
12364.73771	6^3F	7^3F	4940900	16.77194052	79	117	F
12364.77869	6^1F	7^1F	1617100	5.485547123	25	37	F
12364.85341	6^1F	7^3F	53581	0.574755683	25	117	S
12380.77787	6^3F	7^1D	6695	0.000973729	79	5	S
12380.89387	6^1F	7^1D	18985	0.008725559	25	5	A
12387.76502	6^3F	7^3D	23615	0.010315415	79	15	A
12387.88115	6^1F	7^3D	2810.1	0.003878964	25	15	S
12575.14513	6^1P	7^1D	177890	0.702869922	3	5	A
12582.35345	6^1P	7^3D	14.54	0.000172547	3	15	S
13033.67663	6^3D	7^3P	82459	0.126000381	15	9	A
13045.56439	6^1D	7^3P	2.717	1.24778E-05	5	9	S
13569.06455	8^3S	10^3P	2592.2	0.021465363	3	9	A
14204.82181	6^1P	7^1S	270910	0.273164353	3	1	A
14316.91623	7^3S	8^3P	4331.1	0.039927038	3	9	A
14672.97585	8^1S	10^1P	6796.7	0.065811899	1	3	A

λ_{ij} (nm)	i	j	A_{ji} (s^{-1})	f_{ij}	g_i	g_j	Trans. type
14803.98917	6^3P	7^3S	346810	0.379818869	9	3	A
15473.23348	8^3P	10^1D	1.22	2.43275E-06	9	5	S
15477.15305	8^3P	10^3D	22813	0.13654065	9	15	A
16064.13579	7^1S	8^1P	14688	0.170469746	1	3	A
16110.4495	8^1D	10^1P	10063	0.023493228	5	3	A
16173.6094	8^3D	10^1F	8417.9	0.112239376	15	51	S
16173.65504	8^3D	10^3F	36472	1.535179669	15	161	A
16181.77106	8^1D	10^1F	8427.4	0.337438434	5	51	A
16181.81674	8^1D	10^3F	8427.4	1.065252835	5	161	S
16200.24487	8^3F	10^1F	6961.882	0.008676864	161	51	S
16200.29065	8^3F	10^3F	568209.2878	2.235643768	161	161	F
16200.33233	8^1F	10^1F	184971.68	0.727782738	51	51	F
16200.37812	8^1F	10^3F	7592.225	0.094302615	51	161	S
16209.80919	8^3F	10^1D	1453	0.000177752	161	5	S
16209.89675	8^1F	10^1D	4899.3	0.001892095	51	5	A
16214.11087	8^3F	10^3D	5905.6	0.002168525	161	15	A
16214.19848	8^1F	10^3D	609.35	0.000706362	51	15	S
16350.85203	8^1P	10^1D	29119	0.194515693	3	5	A
16355.2289	8^1P	10^3D	2.159	4.32897E-05	3	15	S
16576.32115	8^3D	10^3P	16855	0.041658629	15	9	A
17221.63504	8^1P	10^1S	47328	0.070144613	3	1	A
17285.45435	8^3P	10^3S	55364	0.08266401	9	3	A
17603.81478	7^3P	8^1D	4.377	1.12971E-05	9	5	S
17613.48414	7^3P	8^3D	57426	0.4451399	9	15	A
18100.03139	4^1S	4^1P	58221	0.857843833	1	3	A
18504.65881	3^3P	3^1D	2.317	6.60791E-06	9	5	S
18622.53083	3^3P	3^3D	12916	0.11191875	9	15	A
18806.63881	7^3D	8^1P	2.02	2.14216E-06	15	3	S
18822.76582	7^1D	8^1P	25468	0.081163662	5	3	A
18996.63662	7^3D	8^1F	25031	0.460425332	15	51	S
18996.75688	7^3D	8^3F	101220	5.877715236	15	161	A
19013.09126	7^1D	8^1F	84683	4.681128196	5	51	A
19013.21173	7^1D	8^3F	14631	2.5532275	5	161	S
19051.04438	7^3F	8^1F	20881	0.049524699	117	51	S
19051.16533	7^3F	8^3F	1948700	14.59072101	117	161	F
19051.22175	7^1F	8^1F	636362	4.772731649	37	51	F
19051.3427	7^1F	8^3F	23073.77	0.546314279	37	161	S
19076.77685	7^3F	8^1D	3904	0.000910233	117	5	S
19076.9547	7^1F	8^1D	12290	0.009061225	37	5	A

λ_{ij} (nm)	i	j	A_{ji} (s^{-1})	f_{ij}	g_i	g_j	Trans. type
19088.13254	7^3F	8^3D	14995	0.010500922	117	15	A
19088.31061	7^1F	8^3D	1638.4	0.003628216	37	15	S
19369.10264	7^1P	8^1D	79119	0.741646929	3	5	A
19380.80913	7^1P	8^3D	6.189	0.000174254	3	15	S
19753.9024	4^1S	4^1D	0.0002	5.93364E-09	1	5	F
20119.15687	7^3D	8^3P	45429	0.165406527	15	9	A
20137.61454	7^1D	8^3P	2.762	3.02246E-05	5	9	S
21098.41161	8^3S	9^3P	2000.2	0.040044499	3	9	A
21955.03841	7^1P	8^1S	137390	0.330941273	3	1	A
22040.21975	5^3S	5^3P	70092	1.531335004	3	9	A
23039.00466	7^3P	8^3S	172950	0.458749284	9	3	A
23522.30451	8^1S	9^1P	7258.9	0.180634402	1	3	A
25724.35276	8^3P	9^1D	1.507	8.30574E-06	9	5	S
25739.06663	8^3P	9^3D	27821	0.460527678	9	15	A
27425.03098	8^3D	9^1P	1.151	2.59566E-06	15	3	S
27448.50628	8^1D	9^1P	15165	0.102773171	5	3	A
27709.6603	8^3D	9^1F	11555	0.452230586	15	51	S
27709.84232	8^3D	9^3F	48613	6.006255617	15	161	A
27733.62562	8^1D	9^1F	40994	4.821502851	5	51	A
27733.80795	8^1D	9^3F	11580	4.299640065	5	161	S
27787.9346	8^3F	9^1F	10266.345	0.037646218	161	51	S
27788.11766	8^3F	9^3F	890209.5325	10.30526492	161	161	F
27788.19193	8^1F	9^1F	290204.68	3.359492329	51	51	F
27788.37498	8^1F	9^3F	11217.002	0.409927884	51	161	S
27826.49122	8^3F	9^1D	2370	0.000854394	161	5	S
27826.74926	8^1F	9^1D	7991.6	0.009095094	51	5	A
27843.70892	8^3F	9^3D	9634.4	0.010432608	161	15	A
27843.96728	8^1F	9^3D	994.28	0.003398918	51	15	S
28244.73422	8^1P	9^1D	39331	0.783984335	3	5	A
28262.47356	8^1P	9^3D	2.987	0.000178844	3	15	S
29388.51184	8^3D	9^3P	26504	0.205904826	15	9	A
29415.47052	8^1D	9^3P	1.541	3.59812E-05	5	9	S
29731.36065	9^3S	10^3P	1018.5	0.040491188	3	9	A
32102.49628	8^1P	9^1S	75513	0.388889969	3	1	A
32982.9773	9^1S	10^1P	3909.2	0.191265887	1	3	A
33866.69493	8^3P	9^3S	93837	0.537832638	9	3	A
35848.71393	5^1S	5^1P	18738	1.083029563	1	3	A
36036.77887	9^3P	10^3D	14748	0.478544656	9	15	A
38366.99939	9^1D	10^1P	9442.9	0.125031941	5	3	A

λ_{ij} (nm)	i	j	A_{ji} (s^{-1})	f_{ij}	g_i	g_j	Trans. type
38740.61022	9^3D	10^1F	5905.3	0.451754471	15	51	S
38740.87205	9^3D	10^3F	25573	6.175949592	15	161	A
38773.99102	9^1D	10^1F	21686	4.985506632	5	51	A
38774.25331	9^1D	10^3F	5920	4.296483289	5	161	A
38848.74461	9^3F	10^1F	5519.956	0.039562393	161	51	S
38849.0079	9^3F	10^3F	453686.1121	10.26511957	161	161	F
38849.10239	9^1F	10^1F	147699.98	3.341881733	51	51	F
38849.36569	9^1F	10^3F	5976.028	0.426859401	51	161	S
38903.79033	9^3F	10^1D	1497	0.001054869	161	5	S
38904.14913	9^1F	10^1D	5295	0.011778942	51	5	A
38928.57754	9^3F	10^3D	6333	0.013404808	161	15	A
38928.93679	9^1F	10^3D	627.76	0.004194773	51	15	S
38967.64933	6^3S	6^3P	26981	1.842622524	3	9	A
39249.90971	5^1S	5^1D	0	5.19393E-09	1	5	F
39479.41409	9^1P	10^1D	21278	0.828647098	3	5	A
39504.94047	9^1P	10^3D	1.583	0.000185184	3	15	S
41134.31109	9^3D	10^3P	16240	0.247169224	15	9	A
43967.67293	4^3P	4^3D	4153.7	0.200631675	9	15	A
44969.56906	9^1P	10^1S	44230	0.446973523	3	1	A
47426.97496	7^3S	7^1P	0.0017	5.70895E-08	3	3	S
47641.34456	9^3P	10^3S	54401	0.61702436	9	3	A
62484.50709	6^1S	6^1P	7432.1	1.305047016	1	3	A
62862.26025	7^3S	7^3P	12106	2.151545679	3	9	A
68539.28698	6^1S	6^1D	0	4.50827E-09	1	5	F
85878.46759	5^3P	5^3D	1517.4	0.279618605	9	15	A
92748.28946	3^3D	3^1P	0.0398	1.02731E-06	15	3	S
94921.73501	8^3S	8^3P	6068.3	2.4590553	3	9	A
95787.1018	3^1D	3^1P	152.81	0.012611471	5	3	A
99808.04134	7^1S	7^1P	3404.4	1.525251865	1	3	A
136343.7385	9^3S	9^3P	3307.9	2.765621132	3	9	A
148525.8565	6^3P	6^3D	641.81	0.353759428	9	15	A
149619.842	8^1S	8^1P	1732.6	1.74440214	1	3	A
188325.9281	10^3S	10^3P	1925.6	3.071540363	3	9	A
206527.0175	7^1S	7^3P	0	1.33401E-07	1	9	S
207335.7397	4^3D	4^1P	0.0081	1.0381E-06	15	3	S
213720.4098	9^1S	9^1P	955.42	1.962710482	1	3	A
216187.5095	4^1D	4^1P	56.862	0.023904697	5	3	A
236084.2643	7^3P	7^3D	305.29	0.42515185	9	15	A
293910.2208	10^1S	10^1P	561.27	2.180575482	1	3	A

λ_{ij} (nm)	i	j	A_{ji} (s^{-1})	f_{ij}	g_i	g_j	Trans. type
352729.159	8^3P	8^3D	159.18	0.494844375	9	15	A
395085.2694	5^3D	5^1P	0.0025	1.17004E-06	15	3	S
413695.3225	5^1D	5^1P	22.222	0.034209307	5	3	A
502636.4073	9^3P	9^3D	89.249	0.563389379	9	15	A
673986.1903	6^3D	6^1P	0.001	1.33423E-06	15	3	S
689982.0647	10^3P	10^3D	53.059	0.631149258	9	15	A
707316.1437	6^1D	6^1P	9.7658	0.043947571	5	3	A
1352628.083	4^3D	4^3F	0.0781	0.002999209	15	21	A
1837655.232	4^1D	4^1F	0.0225	0.00159629	5	7	A
2356232.533	9^1D	9^1P	1.4325	0.071537019	5	3	A
3225775.25	10^1D	10^1P	0.8596	0.080456193	5	3	A

Chapter C: Electron Induced Excitation and Ionization Fitting Coefficients for Neutral Helium

These fitting coefficients were published by Ralchenko in 2008 [83].

Table C.1: Dipole allowed electron induced excitation fitting coefficients used in the CGS-CRM.

i	j	A_1	A_2	A_3	A_4	A_5	A_6
1^1S	2^1P	7.09E-01	-9.35E-02	-1.598	2.986	-1.293	3.09E-01
1^1S	3^1P	1.73E-01	2.41E-02	-4.71E-01	7.69E-01	-3.22E-01	8.57E-01
1^1S	4^1P	6.92E-02	6.89E-03	-2.08E-01	3.51E-01	-1.50E-01	4.28E-02
2^1S	2^1P	3.40E+01	7.27E+01	1.71E+02	-7.03E+02	4.70E+02	1.19E+01
2^1S	3^1P	3.336	-1.147	-4.889	2.02E+01	-1.34E+01	1.06E+01
2^1S	4^1P	8.83E-01	-3.62E-01	-1.231	5.606	-3.985	5.89
2^1P	3^1S	4.604	-2.204	-1.09E+01	3.89E+01	-2.44E+01	5.612
2^1P	3^1D	6.26E+01	4.46E+01	-2.41E+02	4.07E+02	-1.96E+02	1.06E+01
2^1P	4^1S	5.55E-01	-4.40E-04	-6.36E-01	1.785	-4.66E-01	3.675
2^1P	4^1D	7.91	9.449	-4.53E+01	7.30E+01	-3.37E+01	5.963
3^1S	3^1P	1.84E+02	5.15E+02	-2.76E+03	4.08E+03	-1.83E+03	2.33E+01
3^1S	4^1P	1.52E+01	-3.47E+01	7.92E+01	-6.47E+01	2.03E+01	2.14E+00
3^1D	3^1P	2.93E+02	8.06E+02	1.23E+05	-9.22E+05	1.90E+06	1.13E+02
3^1D	4^1F	4.15E+02	3.15E+02	-2.07E+03	3.52E+03	-1.65E+03	2.41E+01
3^1D	4^1P	3.712	2.713	-5.615	5.29	-2.158	0
3^1P	4^1S	7.88E+00	1.10E+02	-5.54E+02	1.01E+03	-5.63E+02	3.56E+01
3^1P	4^1D	1.63E+02	6.05E+01	-1.06E+03	2.40E+03	-1.39E+03	2.59E+01
4^1S	4^1P	6.79E+02	9.86E+02	-1.75E+04	-4.42E+03	2.28E+05	1.88E+01
4^1D	4^1F	1.50E+03	3.30E+03	1.25E+04	-2.97E+04	1.50E+04	6.44E+00
4^1D	4^1P	1.16E+03	3.65E+03	6.91E+05	-1.08E+07	5.97E+07	1.52E+02
2^3S	2^3P	7.70E+01	1.25E+02	4.94E+01	-4.78E+02	3.19E+02	8.157
2^3S	3^3P	3.292	-3.594	3.934	1.14E+01	-8.145	3.36
2^3S	4^3P	9.70E-01	-4.92E-01	1.629	5.63E-01	4.41E-02	5.963
2^3P	3^3S	1.93E+01	4.277	-6.31E+01	1.48E+02	-6.06E+01	8.088
2^3P	3^3D	1.41E+02	9.03E+01	-6.24E+02	1.18E+03	-6.42E+02	8.626

i	j	A_1	A_2	A_3	A_4	A_5	A_6
2^3P	4^3S	2.198	2.45E-01	-4.39E-01	-1.691	7.824	4.614
2^3P	4^3D	2.21E+01	2.20E+01	-1.16E+02	2.05E+02	-1.06E+02	5.876
3^3S	3^3P	4.88E+02	7.57E+02	-6.38E+03	1.26E+04	-7.06E+03	1.65E+01
3^3S	4^3P	7.079	-9.04E-01	-1.83	2.06E+01	-8.431	2.199
3^3P	3^3D	9.80E+02	1.37E+03	8.39E+04	-4.65E+05	6.38E+05	4.21E+01
3^3P	4^3S	1.23E+02	2.41E+01	-5.26E+02	1.27E+03	-6.44E+02	2.30E+01
3^3P	4^3D	3.30E+02	6.36E+01	-1.63E+03	4.16E+03	-2.51E+03	2.52E+01
3^3D	4^3F	1.26E+03	8.46E+02	-6.97E+03	1.32E+04	-6.78E+03	2.29E+01
3^3D	4^3P	2.64E+01	-8.708	8.50E+01	4.8	-2.92E+01	4.31
4^3S	4^3P	3.31E+03	-8.48E+03	2.03E+04	-1.87E+04	6.91E+03	2.73E+00
4^3P	4^3D	3.46E+03	8.77E+03	5.01E+05	-6.35E+06	1.99E+07	6.45E+01
4^3D	4^3F	2.88E+03	2.42E+04	1.66E+07	-2.55E+08	2.91E+09	5.76E+02

Table C.2: Dipole forbidden electron induced excitation fitting coefficients used in the CGS-CRM.

i	j	A_1	A_2	A_3	A_4	A_5
1^1S	2^1S	1.89E-01	-5.75E-01	3.439	-2.088	2.54E+01
1^1S	3^1S	4.03E-02	-1.87E-02	2.368	-1.379	1.26E+02
1^1S	3^1D	9.71E-03	2.86E-02	-8.27E-02	4.94E-02	1.99E-01
1^1S	4^1S	1.61E-02	-5.56E-02	2.94E-01	-2.02E-01	2.34E+01
1^1S	4^1D	5.42E-03	1.20E-02	-3.17E-02	1.61E-02	1.06E-01
1^1S	4^1F	4.38E-05	-1.03E-04	3.77E-03	1.63E-02	5.64E+01
2^1S	3^1S	3.762	-1.14E+01	1.40E+01	-5.377	1.01
2^1S	3^1D	1.06E+01	3.49E+01	7.83E+01	-1.04E+02	5.37E+01
2^1S	4^1S	7.83E-01	-2.417	2.876	-1.108	0
2^1S	4^1D	1.872	5.458	-6.857	5.902	3.36E+01
2^1S	4^1F	5.04E-01	4.182	-6.329	3.139	9.425
2^1P	3^1P	1.69E+01	-4.92E+01	1.19E+02	-7.71E+01	1.08E+01
2^1P	4^1F	4.731	2.71E+01	-3.21E+01	1.99E+01	2.37E+01
2^1P	4^1P	3.599	-1.27E+01	1.92E+01	-1.01E+01	0
3^1S	3^1D	4.27E+01	-1.49E+01	-1.04E+02	7.96E+01	1.70E+00

i	j	A_1	A_2	A_3	A_4	A_5
3^1S	4^1S	1.52E+01	-8.16E+01	1.70E+02	-9.93E+01	5.103
3^1S	4^1D	2.59E+01	-8.59E+01	1.02E+02	-4.01E+01	0
3^1S	4^1F	1.94E+01	-4.54E+01	3.91E+01	-1.20E+01	0
3^1D	4^1S	5.089	-2.33E+01	5.94E+01	-4.07E+01	6.13E-01
3^1D	4^1D	9.11E+01	-2.98E+02	6.17E+02	-3.16E+02	1.18E+01
3^1P	4^1F	1.54E+02	7.43E+02	4.11E+02	-5.99E+02	2.06E+02
3^1P	4^1P	6.44E+01	-2.37E+02	4.78E+02	-3.08E+02	1.64E+01
4^1S	4^1D	1.68E+02	-7.06E+02	1.02E+03	-4.83E+02	0.00E+00
4^1S	4^1F	3.02E+01	-8.98E+02	2.24E+04	-2.15E+04	2.75E+02
4^1F	4^1P	1.66E+02	3.06E+03	2.50E+04	-2.82E+04	2.26E+02
2^3S	3^3S	8.344	-2.66E+01	3.49E+01	-1.43E+01	0
2^3S	3^3D	1.68E+01	5.84E+01	3.44E+02	-3.92E+02	6.29E+01
2^3S	4^3S	1.636	-3.577	1.959	8.52E-01	0
2^3S	4^3D	4.063	1.54E+01	6.09E+01	-7.12E+01	5.76E+01
2^3S	4^3F	5.68E-01	4.383	9.326	-9.539	1.82E+01
2^3P	3^3P	4.51E+01	-1.26E+02	2.15E+02	-6.75E+01	4.133
2^3P	4^3P	9.11	-2.18E+01	2.24E+01	-5.75E+00	0
2^3P	4^3F	9.56	6.00E+01	3.66E+01	-5.02E+01	3.16E+01
3^3S	3^3D	1.29E+02	-2.07E+01	-3.57E+02	2.50E+02	0
3^3S	4^3S	3.86E+01	-1.90E+02	3.64E+02	-5.59E+01	1.72E+01
3^3S	4^3D	3.03E+01	1.19E+02	1.21E+02	-1.56E+02	5.76E+01
3^3S	4^3F	3.90E+01	1.08E+02	8.38E+02	-8.42E+02	4.84E+01
3^3P	4^3F	4.06E+02	1.63E+03	6.41E+03	-5.66E+03	1.83E+02
3^3P	4^3P	1.83E+02	-8.06E+02	1.38E+03	-7.12E+02	2.103
3^3D	4^3S	2.78E+01	9.86E+01	8.70E+02	2.31E+03	1.77E+02
3^3D	4^3D	2.77E+02	-8.11E+02	3.73E+03	-2.66E+03	3.31E+01
4^3S	4^3D	5.09E+02	-1.95E+03	2.49E+03	-1.04E+03	0
4^3S	4^3F	1.05E+02	-1.97E+03	2.35E+04	-2.14E+04	9.32E+01
4^3P	4^3F	6.85E+02	-8.64E+04	1.88E+07	-1.83E+07	2.74E+04

Table C.3: Spin forbidden electron induced excitation fitting coefficients used in the CGS-CRM.

i	j	A_1	A_2	A_3	A_4	A_5
1^1S	2^3P	2.82E-01	2.048	5.287	-7.363	2.73E+01
1^1S	2^3S	6.89E-01	1.98E-01	7.232	-4.839	5.00E+01
1^1S	3^3D	2.21E-03	8.43E-03	1.82E-01	-1.81E-01	9.54E+00
1^1S	3^3P	6.73E-02	5.47E-01	-4.43E-01	-1.04E-01	1.14E+01
1^1S	3^3S	9.39E-02	-1.64E-01	7.61E-02	-4.54E-03	-9.25E-01
1^1S	4^3D	1.33E-03	1.82E-02	-3.85E-02	1.90E-02	-9.89E-01
1^1S	4^3F	0.00E+00	4.08E-04	-3.86E-04	1.70E-05	-9.50E-01
1^1S	4^3P	2.59E-02	2.28E-01	-5.83E-02	-1.62E-01	1.51E+01
1^1S	4^3S	3.01E-02	-3.96E-02	-1.94E-03	1.15E-02	-9.81E-01
2^3S	2^1S	5.48E+01	3.48E+05	2.35E+05	-5.09E+05	5.42E+04
2^3S	2^1P	4.89E+01	4.25E+03	-4.33E+03	1.93E+02	8.93E+02
2^3S	3^1S	6.56E-01	5.72E+02	2.98E+03	-1.77E+03	5.21E+03
2^3S	3^1D	1.854	3.98E+01	4.699	-2.65E+01	8.09E+01
2^3S	3^1P	1.383	5.35E+01	3.94E+02	-4.38E+02	4.33E+02
2^3S	4^1S	1.69E-01	7.33E+01	8.90E+01	1.83E+02	2.18E+03
2^3S	4^1D	5.49E-01	8.462	-1.08E+01	5.007	3.46E+01
2^3S	4^1F	8.21E-02	-1.31E+01	1.16E+03	-1.00E+03	5.40E+03
2^3S	4^1P	3.41E-01	9.77	2.17E+02	-2.24E+02	5.03E+02
2^1S	2^3P	5.98E+02	-5.31E+02	3.35E+02	-2.41E+02	2.24E+02
2^1S	3^3S	6.65E-01	1.94E+03	6.94E+02	1.45E+03	6.34E+03
2^1S	3^3P	1.382	8.31E+01	2.83E+02	-1.83E+02	3.18E+02
2^1S	3^3D	4.042	1.36E+02	8.14E+01	-2.09E+02	1.74E+02
2^1S	4^3S	1.24E-01	2.04E+02	-2.54E+02	1.09E+03	3.58E+03
2^1S	4^3P	2.70E-01	1.19E+01	7.598	1.182	1.05E+02
2^1S	4^3D	9.48E-01	2.12E+01	-7.385	-1.09E+01	7.92E+01
2^1S	4^3F	2.34E-01	-6.76E+01	8.61E+03	-8.04E+03	1.77E+04
2^3P	2^1P	7.48E+03	-7.36E+01	-1.48E+04	9.36E+03	1.36E+03
2^3P	3^1S	3.068	1.91E+02	1.31E+03	-1.19E+03	5.77E+02
2^3P	3^1D	1.25E+01	8.43E+02	-7.19E+02	1.67E+02	2.11E+02
2^3P	3^1P	1.01E+01	3.35E+03	1.03E+04	-1.27E+04	3.02E+03
2^3P	4^1S	5.90E-01	1.76E+01	1.29E+01	1.79E+01	1.16E+02
2^3P	4^1D	3.009	1.19E+02	-1.72E+02	9.98E+01	9.53E+01
2^3P	4^1F	5.66E-01	1.78E+01	-3.46E+01	1.99E+01	1.57E+01
2^3P	4^1P	2.226	4.01E+02	3.28E+03	-3.64E+03	1.90E+03
2^1P	3^3S	4.98	4.42E+02	1.00E+03	-8.06E+02	5.63E+02
2^1P	3^3P	1.09E+01	8.33E+03	1.93E+04	-1.73E+04	5.54E+03

i	j	A_1	A_2	A_3	A_4	A_5
2^1P	3^3D	1.70E+01	1.48E+03	-4.59E+02	-8.79E+02	3.23E+02
2^1P	4^3S	6.49E-01	2.53E+01	-1.162	5.16E+01	1.23E+02
2^1P	4^3P	2.243	5.62E+02	8.40E+02	-3.63E+02	1.50E+03
2^1P	4^3D	3.686	1.89E+02	-9.472	-1.47E+02	1.73E+02
2^1P	4^3F	8.68E-01	3.06E+01	-3.48E+01	1.13E+01	3.76E+01
3^3S	3^1S	1.73E+02	2.35E+06	5.04E+06	-7.31E+06	3.60E+05
3^3S	3^1D	1.55E+02	4.93E+04	4.58E+04	-9.48E+04	6.63E+03
3^3S	3^1P	6.10E+01	-1.35E+02	1.27E+02	-5.26E+01	6.19E+00
3^3S	4^1S	9.80E-01	7.70E+03	-2.35E+04	4.41E+04	1.80E+04
3^3S	4^1D	3.036	-2.08E+03	6.54E+05	-5.50E+05	1.36E+05
3^3S	4^1F	9.16E-01	6.19E+02	2.08E+02	-6.68E+02	3.05E+02
3^3S	4^1P	1.725	4.20E+02	1.48E+03	-1.85E+03	1.19E+03
3^1S	3^3P	1.24E+03	1.09E+07	-2.10E+07	1.14E+07	3.43E+05
3^1S	3^3D	6.73E+02	6.02E+05	-2.03E+06	1.79E+06	2.71E+04
3^1S	4^3S	1.395	1.37E+04	-3.39E+04	7.06E+04	2.14E+04
3^1S	4^3P	1.878	7.17E+02	1.40E+03	6.21E+01	1.29E+03
3^1S	4^3D	4.674	2.27E+02	7.47E+02	-8.39E+02	2.91E+02
3^1S	4^3F	1.601	1.31E+03	5.19E+02	-1.59E+03	4.90E+02
3^3P	3^1D	6.04E+03	4.21E+07	-1.97E+08	2.64E+08	2.22E+05
3^3P	3^1P	6.01E+03	-1.06E+04	1.09E+04	-6.08E+03	8.16E+02
3^3P	4^1S	3.483	1.34E+03	5.30E+03	-2.06E+03	2.15E+03
3^3P	4^1D	7.376	2.99E+03	8.03E+03	-7.80E+03	1.07E+03
3^3P	4^1F	6.27E+01	6.84E+03	1.57E+03	-5.61E+03	1.12E+03
3^3P	4^1P	2.78E+01	-8.09E+01	3.21E+02	-2.67E+02	2.33E+01
3^3D	3^1D	1.14E+09	2.02E+12	-1.20E+15	1.67E+17	1.34E+08
3^3D	3^1P	1.10E+05	-5.17E+05	8.28E+05	-4.20E+05	1.46E+04
3^3D	4^1S	6.08E-01	9.78E+02	1.62E+03	-1.57E+03	8.71E+02
3^3D	4^1D	4.72E+01	1.22E+05	2.17E+05	-2.72E+05	1.94E+04
3^3D	4^1F	6.31E+01	2.58E+04	-1.48E+04	-5.01E+03	1.50E+03
3^3D	4^1P	0	2.96E+03	6.34E+03	-9.30E+03	9.41E+02
3^1D	4^3S	1.499	1.81E+03	1.01E+03	-6.55E+02	9.34E+02
3^1D	4^3P	0	3.37E+03	6.12E+03	-5.15E+03	8.64E+02
3^1D	4^3D	4.74E+01	1.22E+05	2.07E+05	-2.89E+05	1.90E+04
3^1D	4^3F	6.31E+01	2.58E+04	-5.74E+03	-1.45E+04	1.54E+03
3^1P	4^3S	7.973	5.67E+03	5.42E+03	-6.55E+03	3.90E+03
3^1P	4^3P	1.13E+01	1.30E+05	5.81E+04	-8.94E+04	4.62E+04
3^1P	4^3D	1.47E+01	5.35E+03	5.28E+03	-9.21E+03	1.56E+03
3^1P	4^3F	7.77E+01	1.25E+04	8.90E+03	-2.05E+04	2.00E+03
4^3S	4^1S	3.43E+02	9.92E+06	-7.24E+06	3.13E+07	1.15E+06

i	j	A_1	A_2	A_3	A_4	A_5
4^3S	4^1D	2.22E+02	3.02E+06	9.32E+06	-1.23E+07	4.57E+05
4^3S	4^1F	4.68E+01	7.68E+04	-1.27E+05	6.42E+04	5.85E+03
4^3S	4^1P	1.65E+02	1.46E+06	-2.70E+06	1.28E+06	1.72E+05
4^1S	4^3P	2.97E+03	1.71E+08	-4.11E+08	3.78E+08	4.49E+06
4^1S	4^3D	9.65E+02	3.40E+07	-1.02E+08	7.97E+07	1.76E+06
4^1S	4^3F	2.10E+02	9.00E+05	-2.90E+06	2.50E+06	3.24E+04
4^3P	4^1D	1.47E+04	8.68E+08	-3.53E+09	4.06E+09	4.53E+06
4^3P	4^1F	1.88E+04	4.40E+07	-2.11E+08	2.66E+08	2.11E+05
4^3P	4^1P	1.48E+04	-4.75E+04	3.96E+04	3.24E+03	2.20E+03
4^3D	4^1D	7.37E+08	-2.85E+09	5.37E+09	-3.23E+09	6.74E+07
4^3D	4^1F	5.18E+07	-3.39E+08	7.08E+08	-4.14E+08	3.81E+06
4^3D	4^1P	3.47E+05	-1.22E+05	-1.17E+07	2.97E+07	7.59E+04
4^1D	4^3F	8.17E+07	-4.65E+08	9.30E+08	-5.42E+08	7.00E+06
4^3F	4^1F	1.03E+10	3.47E+13	-2.93E+16	5.67E+18	6.30E+08
4^3F	4^1P	2.52E+05	-1.06E+06	-1.45E+06	8.09E+06	4.05E+04

Table C.4: Electron induced ionization fitting coefficients used in the CGS-CRM.

i	A_1	A_2	A_3	A_4	A_5	A_6
1^1S	5.86E-01	-4.46E-01	7.68E-01	-2.521	3.317	0
2^3S	2.43E-01	-1.90E-01	3.21E-01	7.63E-01	-8.33E-01	-2.41E-01
2^1S	3.08E-01	-2.75E-01	4.46E-01	-1.84E-01	1.336	-1.775
2^3P	2.10E-01	-1.75E-01	2.99E-01	9.49E-01	-4.48E-01	-3.83E-01
2^1P	2.07E-01	-2.03E-01	5.76E-01	-2.44E-01	1.986	-2.019
3^3S	1.88E-01	-1.87E-01	1.223	-3.805	8.412	-5.872
3^1S	1.79E-01	-1.78E-01	7.02E-01	-1.132	3.727	-3.255
3^3P	2.69E-01	-2.61E-01	6.48E-01	-2.256	5.876	-4.273
3^3D	8.03E-02	-7.67E-02	8.84E-01	-4.051	1.11E+01	-7.427
3^1D	9.64E-02	-9.37E-02	1.051	-4.831	1.25E+01	-8.287
3^1P	1.65E-01	-1.64E-01	3.12E-01	-4.33E-02	1.729	-1.691
4^3S	9.43E-02	-7.48E-02	8.67E-01	-3.637	8.681	-5.816
4^1S	1.21E-01	-1.14E-01	7.41E-01	-3.115	7.325	-4.9
4^3P	2.13E-01	-1.96E-01	4.73E-01	-1.8	3.918	-2.596
4^3D	2.51E-02	-4.72E-03	1.34E-01	7.72E-01	-4.39E-01	1.25E-01
4^1D	1.81E-02	1.05E-02	6.38E-	1.172	-9.80E-01	3.38E-01
4^3F	6.74E-03	4.43E-02	-8.95E-02	1.335	4.96E-01	-1.073
4^1F	4.34E-02	1.22E-02	3.51E-01	-1.911	6.694	-4.631
4^1P	1.81E-01	-1.72E-01	2.45E-01	-6.58E-01	2.026	-1.535

Bibliography

[1] H. Barkhausen, "Whistling tones from the Earth," Proceedings of the Institute of Radio Engineers, Vol. 18, No. 7, 1155 (1930).

[2] D. R. Hartree, "The propagation of electromagnetic waves in a refracting medium in a magnetic field," Proceedings of the Cambridge Philosophical Society, Vol. 27, 143 (1931).

[3] E. V. Appleton, "Wireless studies of the ionosphere," Journal of the Institution of Electrical Engineers, Vol. 71, No. 430, 642 (1932).

[4] L. R. O. Storey, "An Investigation of whistling atmospherics," Philosophical Transactions of the Royal Society of London A, Vol. 246, No. 908, 113 (1953).

[5] P. Aigrain, "Les 'helicons' dans les semiconductors," Proceedings of the International Conference on Semiconductor Physics, Prague, Czechoslovakia, 224 (1960).

[6] C. R. Legéndy, "Macroscopic theory of helicons," Physical Review, Vol. 135, No. 6A, A 1713 (1964).

[7] J. P. Klozenberg, B. McNamara, and P. C. Thonemann, "The dispersion and attenuation of helicon waves in a uniform cylindrical plasma," Journal of Fliud Mechanics, Vol. 21, No. 3, 545 (1965).

[8] R. M. Gallet, J. M. Richardson, B. Wieder, and G. D. Ward, "Microwave whistler propagation in a dense laboratory plasma," Physical Review Letters, Vol. 4, No. 7, 347 (1960).

[9] J. A. Lehane and P. C. Thonemann, "An experimental study of helicon wave propagation in a gaseous plasma," Proceedings of the Physical Society, Vol. 85, No. 2, 301 (1965).

[10] R. W. Boswell, "Plasma production using a standing helicon wave," Physics Letters, Vol. 33A, No. 7, 457 (1970).

[11] A. J. Perry, R. W. Boswell, "Fast anisotropic etching of silicon in an inductively coupled plasma reactor, "Applied Physics Letters, Vol. 55, No. 2, 148 (1989).

[12] C. Charles, "Ion energy distribution functions in a multipole confined argon plasma diffusing from a 13.56-MHz helicon source," Journal of Vacuum Science & Technology A, Vol. 11, No. 1, 157 (1993).

[13] H. Kitagawa, "Etching characteristics in helicon wave plasma," Plasma Sources Science & Technology, Vol. 2, No. 1, 11 (1993).

[14] N. Jiwari, H. Iwasawa, A. Narai, H. Sakaue, H. Shindo, T. Shoji, and Y. Horiike, "Al etching characteristics employing helicon wave plasma," Japanese Journal of Applied Physics Part 1, Vol. 32, No. 6B, 3019 (1993).

[15] N. Benjamin, B. Chapman, and R. Boswell, "Process of an advanced diffusion source plasma reactor," Proceedings of SPIE, Vol. 1392, (1991).

[16] J. P. Squire, F. R. Chang Díaz, V. T. Jacobson, G. E. McCaskill, "Helicon plasma injector and ion cyclotron acceleration development in the VASIMR experiment," 36th AIAA/ASME/SAE/ASEE Joint Propulsion Conference, 17-19 July, AIAA 2000-3752 (2000).

[17] F. F. Chen, "Plasma ionization by helicon waves," Plasma Physics and Controlled Fusion, Vol. 33, No. 4, 339 (1991).

[18] B. M. Harvey, C. N. Lashmore-Davies, "The absorption mechanisms of whistler waves in cool, dense, cylindrically bounded plasmas," Physics of Fluids B, Vol.5, No. 11, 3864 (1993).

[19] A. Komori, T. Shoji, K. Miyamoto, J. Kawai, and Y. Kawai, "Helicon waves and efficient plasma production," Physics of Fluids B: Plasma Physics **Vol. 3**, 893 (1991).

[20] P. A. Keiter, E. E. Scime, and M. M. Balkey, "Frequency dependent effects in helicon plasmas," Physics of Plasmas, Vol. 4, No. 7, 2741 (1997).

[21] F. F. Chen and D. D. Blackwell, "Upper Limit to Landau Damping in Helicon Discharges," Physical Review Letters, Vol. 82, No. 13, 2677 (1999).

[22] K. P. Shamrai and V. B. Taranov, "Volume and surface RF power absorption in a helicon plasma source," Plasma Sources Science & Technology, Vol. 5, 474 (1996).

[23] G. G. Borg and R. W. Boswell, "Power coupling to helicon and Trivelpiece-Gould modes in helicon sources," Physics of Plasmas, Vol. 5, No. 3, 564 (1998).

[24] Y. Mouzouris and J. E. Scharer, "Wave propagation and absorption simulations for helicon sources," Physics of Plasmas, Vol. 5, No. 12, 4253 (1998).

[25] D. Arnush, "The role of Trivelpiece-Gould waves in antenna coupling to helicon waves," Physics of Plasmas, Vol. 7, No. 7, 3042 (2000).

[26] D. D. Blackwell, T. G. Madziwa, D. Arnush, and F. F. Chen,"Evidence for Trivelpiece-Gould modes in a helicon discharge," LTP-106, Low Temperature Plasma Technology Laboratory, UCLA (2001).

[27] J. L. Kline, E. E. Scime, R. F. Boivin, A. M. Keesee, X. Sun, and V. S. Mikhailenko, "RF absorption and ion heating in helicon sources," Physical Review Letters, Vol. 88, No. 19, 195002 (2002).

[28] R. D. Tarey, B. B. Sahu, and A. Ganguli, "Understanding helicon plasmas," Physics of Plasmas, Vol. 19, 073520 (2012).

[29] E. B. Hooper, S. W. Ferguson, M. A. Makowski, B. W. Stallard, J. L. Power, "Analysis and experiments of a whistler-wave plasma thruster," Lawrence Livermore preprint UCRL-JC-114643, IEPC-93-03B, 361 (1993).

[30] C. Charles, R. W. Boswell, "Current-free double-layer formation in a high-density helicon discharge," Applied Physics Letters, Vol. 82, No. 9, 1356 (2003).

[31] C. Charles, R. W. Boswell, "Laboratory evidence of a supersonic ion beam generated by a current-free helicon double-layer," Physics of Plasmas, Vol. 11, No. 4, 1706 (2004).

[32] A. M. Keesee, E. E. Scime, C. Charles, A. Meige, and R. W. Boswell, "The ion velocity distribution function in a current-free double layer," Physics of Plasmas, Vol. 12, 093502 (2005).

[33] F. N. Gesto, B. D. Blackwell, C. Charles, and R. W. Boswell, "Ion detachment in the helicon double-layer thruster exhaust beam," Journal of Propulsion and Power, Vol. 22, No. 1, 24 (2006).

[34] W. Cox, C. Charles, R. W. Boswell, and R. Hawkins, "Spatial retarding field energy analyzer measurements downstream of a helicon double layer plasma," Applied Physics Letters, Vol. 93, 071505 (2008).

[35] M. D. West, C. Charles, and R. W. Boswell, "Testing a helicon double layer thruster immersed in a space-simulation chamber," Journal of Propulsion and Power, Vol. 24, No. 1, 134 (2008).

[36] F. F. Chen, "Physical mechanism of current-free double layers," Physics of Plasmas, Vol. 13, 034502 (2006).

[37] N. Plihon, P. Chabert, and C. S. Corr, "Experimental investigation of double layers in expanding plasmas," Physics of Plasmas, Vol. 14, 013506 (2007).

[38] T. Ziemba, J. Carscadden, J. Slough, J. Prager, and R. Winglee, "High power helicon thruster," AIAA 2005-4119, 41st AIAA/ASME/SAE/ASEE Joint Propulsion Conference & Exhibit, 10-13 July, Tucson, Arizona (2005).

[39] N. Plihon, P. Chabert, J. Raimbault, "Helicon double layer thruster concept for high power NEP missions," Final Report, Laboratorie de Physique et Technologie des Plasmas, CNRS- Ecole Polytechnique (2006).

[40] J. M. Pucci, N. Sinenian, J. Palaia, M. Çelik, Z. LaBry, A. Shabshelowitz, O. Batishchev, and M. Martinez-Sanchez, "Preliminary characterization of a helicon plasma source for space propulsion," AIAA 2006-5255, 42nd AIAA/ASME/SAE/ASEE Joint Propulsion Conference & Exhibit, 9-12 July, Sacramento, California (2006).

[41] K. Toki, S. Shinohara, T. Tanikawa, K. P. Shamrai, "Small helicon plasma source for electric propulsion," Thin Solid Films, Vol. 506-507, 597 (2006).

[42] K. P. Shamrai, "Compact helicon plasma source with permanent magnets for electric propulsion Application," AIAA 2006-4845, 42nd AIAA/ASME/SAE/ASEE Joint Propulsion Conference & Exhibit, 9-12 July, Sacramento, California (2006).

[43] F. F. Chen, "Permanent magnet helicon source for ion propulsion," IEEE Transactions on Plasma Science, Vol. 36, No. 5, 2095 (2008).

[44] M. DeMaio, R. Sedwick, "Development and test of a permanent magnet helicon thruster," College Park, Maryland, Masters Thesis (2010).

[45] J. P. Squire, F. R. Chang-Díaz, V. T. Jacobson, T. W. Glover, F. W. Baity, M. D. Carter, R. H. Goulding, R. D. Bengston, and E. A. Bering, III, "Investigation

of a light gas helicon plasma source for the VASIMR space propulsion system," Radio Frequency AIP Conference Proceedings, Vol. 694, 423 (2003).

[46] C. Charles, "Hydrogen ion beam generated by a current-free double-layer in a helicon plasma," Applied Physics Letters, Vol. 84, No. 3, 332 (2004).

[47] O. Batishchev, J. Cambier, "Experimental Study of the Mini-Helicon Thruster," AFRL-RZ-ED-TR-2009-0020 (2009).

[48] S. Nguyen, "Hydrogen Production in a Radio-Frequency Plasma Source Operating on Water Vapor," Ann Arbor, Michigan, Ph.D. Thesis (2009).

[49] S. Nguyen, "Operating a radio-frequency plasma source on water vapor," Review of Scientific Instruments, Vol. 80, 083503 (2009).

[50] D. Biggs, S. Avery, L. Raymond, W. Liang, N. Gascon, A. L. Fabris, J. Rivas-Davila, M. Cappelli, "A Compact Helicon Thruster for CubeSat Applications," IEPC-2015-244 / ISTS-2015-b-244, Joint Conference of 30th International Symposium on Space Technology and Science, 34th International Electric Propulsion Conference and 6th Nano-satellite Symposium, Hyogo-Kobe, Japan, July 4-10, (2015).

[51] S. P. Cunningham, "Spectroscopic Observations," U.S. Atomic Energy Commission Report, Vol. 289, 279, (1955).

[52] R. J. Sovie, "Spectroscopic determination of electron temperature and percentage ionization in a helium plasma," Phyiscs of Fluids, Vol. 7, 613, (1964).

[53] R. F. DeVries and R. Mewe, "Spectroscopic determination of electron temperature in a helium plasma," Physics of Fluids, Vol. 9, 414, (1966).

[54] N. Brenning, "Electron temperature measurements in low-density plasmas by helium spectroscopy," Journal of Quantitative Spectroscopy & Radiative Transfer, Vol. 24, 293, (1979).

[55] B. J. Eastlund, D. Spero, M. Johnson, P. Korn, C. B. Wharton, and E. R. Wilson, "Optical diagnostics of an ECRH plasma," Journal of Applied Physics, Vol. 44, 4930, (1973).

[56] R. Prakash, P. Vasu, V. Kumar, R. Manchanda, M. B. Chowdhuri, and M. Goto, "Characterization of helium discharge cleaning plasmas in ADITYA tokamak using collisional-radiative model code," Journal of Applied Physics, Vol. 97, 043301, (2005).

[57] S. J. Davies, P. D. Morgan, Y. Ul'Haq, C. F. Maggi, S. K. Erents, W. Fundamenski, L. D. Horton, A. Loarte, G. F. Matthews, R. D. Monk, P. C. Stangeby, "Parallel electron temperature and density gradients measured in the JET MkI divertor using thermal helium beams," Journal of Nuclear Materials, Vol. 241-243, 426, (1997).

[58] Y. Andrew, S. J. Davies, D. Elder, L. D. Horton, G. F. Matthews, A. Meigs, P. D. Morgan, M. O'Mullane, M. Stamp, R. Prentice, P. C. Stangeby, "Interpretive modelling of JET's thermal helium diagnostic," Journal of Nuclear Materials, Vol. 266-269, 1234, (1999).

[59] H. Kubo, M. Goto, H. Takenaga, A. Kumagai, T. Sugie, S. Sakurai, N. Asakura, S. Higashijima, and A. Sasaki, "Study of intensity ratios of He I lines (668 nm, 706 nm and 728 nm) for measurement of electron temperature and density in the JT-60U divertor plasma,",Plasma Physics and Fusion Technology, Vol. 75, 945, (1999).

[60] S. Kajita, N. Ohno, S. Takamura, and T. Nakano, "Comparison of He I line intensity ratio method and electrostatic probe for electron density and temperature measurements in NAGDIS-II," Physics of Plasmas, Vol. 13, 013301, (2006).

[61] L. Carraro, G. De Pol, M. E. Puiatti, F. Sattin, P. Scarin, and M. Valisa, "Edge temperature and density measurements with a thermal helium beam in the RFX reversed field pinch," Plasma Physics and Controlled Fusion, Vol. 42, 1, (2000).

[62] B. Brañas, D. Tafalla, F. L. Tabarés, and P. Ortiz, "Atomic beam diagnostics for characterization of edge plasma in TJ-II stellarator," Review of Scientific Instruments, Vol. 72, No. 1, 602, (2001).

[63] E. de la Cal, "Application of passive spectroscopy to the He I line intensity ratio technique: a new tool for electron temperature and density measurement in fusion boundary plasmas," Plasma Physics and Controlled Fusion, Vol. 43, 813, (2000).

[64] A. K. Srivastava, M. K. Garg, K. S. G. Prasad, V. Kumar, M. B. Chowdhuri, and R. Prakash, "Characterization of atmospheric pressure glow discharge in helium using langmuir probe, emission spectroscopy, and discharge resistivity," IEEE Transactions on Plasma Science, Vol. 35, No. 4, 1135, (2007).

[65] R. Prakash, J. Jain, V. Kumar, R. Manchanda, B. Agarwal, M. B. Chowdhuri, S. Banerjee, and P. Vasu, "Calibration of a VUV spectrograph by collisional-

radiative modelling of a discharge plasma," Journal of Physics B: Atomic, Molecular and Optical Physics, Vol. 43, 144012, (2010).

[66] S. M. Collis, R. Dall, J. Howard, D. Andruczyk, and B. W. James, "Validation of collisional radiative modelling of emission line ratios for helium beam plasma diagnostic," Journal of Quantitative Spectroscopy & Radiative Transfer, Vol. 110, 340, (2009).

[67] C. P. Ballance, D. C. Griffin, S. D. Loch, R. F. Boivin, and M. S. Pindzola, "Collisional-radiative calculations of He line emission in low-temperature plasmas," Physical Review A, Vol. 74, 012719, (2006).

[68] R. F. Boivin, S. D. Loch, C. P. Ballance, D. Branscomb, and M. S. Pindzola, "Line ratio diagnostics in helium and helium seeded argon plasmas," Plasma Sources Science and Technology, Vol. 16, 470, (2007).

[69] D. R. Bates, A. E. Kingston, and R. W. P. McWhirter, "Recombination between electrons and atomic ions I. Optically thin plasmas," Proceedings of the Royal Society of London. Series A, Mathematical and Physical Sciences, Vol. 267, No. 1330, 297, (1962).

[70] T. Fujimoto, "A collisional-radiative model for helium and its application to a discharge plasma," Journal of Quantitative Spectroscopy & Radiative Transfer, Vol. 21, 439, (1979).

[71] M. Goto, "Collisional-radiative model for neutral helium in plasma revisited," Journal of Quantitative Spectroscopy & Radiative Transfer, Vol. 76, 331, (2003).

[72] S. Sasaki, S. Takamura, S. Watanabe, S. Masuzaki, T. Kato, and K. Kadota, "Helium I line intensity ratios in a plasma for the diagnostics of fusion edge plasmas," Review of Scientific Instruments, Vol. 67, 3521,(1996).

[73] R. F. Boivin, J. L. Kline, and E. E. Scime, "Electron temperature measurement by a helium line intensity ratio method in helicon plasmas," Physics of Plasmas, Vol. 8, 5303 (2001).

[74] M. Çelik, M. Martinez-Sanchez, "Experimental and Computational Studies of Electric Thruster Plasma Radiation Emission," Massachusetts Institute of Technology, Cambridge, Massachusetts, Ph.D. Thesis (2007).

[75] E. M. Sciamma, "Plasma Spectroscopic Diagnostic Tool Using Collisional-Radiative Models and its Application to Different Plasma Discharges for Elec-

tron Temperature and Neutral Density Determination," The University of Texas at Austin, Ph.D. Thesis (2007).

[76] I. D. Sudit, F. F. Chen, "RF compensated probes for high-density discharges," Plasma Sources Science and Technology, Vol. 3, 162 (1994).

[77] F. F. Chen, "Lecture Notes on Langmuir Probe Diagnostics," IEEE-ICOPS meeting, Jeju, Korea, (2003).

[78] S. Chen and T. Sekiguchi, "Instantaneous direct-display system of plasma parameters by means of triple probe," Journal of Applied Physics, Vol. 36, No. 8, 2363, (1965).

[79] F. F. Chen, "Langmuir probes in RF plasma: surprising validity of OML theory," (2008).

[80] https://terpconnect.umd.edu/ toh/spectrum/InteractivePeakFitter.htm.

[81] A. Kramida, Yu. Ralchenko, J. Reader, and NIST ASD Team (2015). NIST Atomic Spectra Database (ver. 5.3), [Online]. Available: http://physics.nist.gov/asd [2015, November 30]. National Institute of Standards and Technology, Gaithersburg, MD.

[82] Yu. V. Ralchenko, R. K. Janev, T. Kato, D. V. Fursa, I. Bray, and F. J. de Heer, "Cross section database for collision processes of helium atom with charged particles. I. electron impact processes," NIFS-DATA-59, National Institute for Fusion Science, (2000).

[83] Y. Ralchenko, R. K. Janev, T. Kato, D. V. Fursa, I. Bray, F. J. de Heer, "Electron-impact excitation and ionization cross sections for ground state and excited helium atoms," Atomic Data and Nuclear Data Tables, Vol. 94, 603, (2008).

[84] L. C. Johnson, "Approximations for collisional and radiative transition rates in atomic hydrogen," The Astrophysical Journal, Vol. 174, 227, (1972).

[85] M. Mitchner, C. H. Kruger, Jr., "Partially Ionized Gases," John Wiley & Sons, Inc., (1973).

[86] W. L. Wiese and J. R. Fuhr, "Accurate atomic transition probabilities for hydrogen, helium, and lithium," Journal of Physical Chemistry Reference Data, Vol. 38, No. 3, (2009).

[87] T. Fujimoto, "Semi-empirical cross sections and rate coefficients for excitation and ionization by electron collision and photoionization of helium," IPPJ-AM-8, National Institute for Fusion Science, (1978).

[88] K. Sawada, Y. Yamada, T. Miyachika, N. Ezumi, A. Iwamae, and M. Goto, "Collisional-radiative model for spectroscopic diagnostic of optically thick helium plasma," Plasma and Fusion Research, Vol. 5, 001, (2010).

[89] M. Goto and K. Sawada, "Determination of electron temperature and density at plasma edge in the Large Helical Device with opacity-incorporated helium collisional-radiative model," Journal of Quantitative Spectroscopy & Radiative Transfer, Vol. 137, 23, (2014).

[90] D. Péquignot, P. Petitjean, and C. Boisson, "Total and effective radiative recombination coefficients," Astronomy and Astrophysics, Vol. 251, 680, (1991).

[91] T. Fujimoto, "Plasma Spectroscopy," Oxford University Press, New York, NY, (2004).

[92] H. J. Kolker and H. H. Michels, "Elastic scattering, diffusion, and excitation transfer of metastable helium in helium," The Journal of Chemical Physics, Vol. 50, 1762, (1969).

[93] B. Schweer, G. Mank, A. Pospieszczyk, B. Brosda, and B. Pohlmeyer, "Electron temperature and electron density profiles measured with a thermal He-beam in the plasma boundary of TEXTOR," Journal of Nuclear Materials, Vol. 196, 174, (1992).

[94] Plasma Data Exchange Project LxCat (www.lxcat.net)

[95] S. F. Biagi 2011 FORTRAN Magboltz v8.97, www.lxcat.net, retrieved on April 20, 2016.

[96] D. V. Fursa and I. Bray,"Calculation of electron-helium scattering," Physical Review A, Vol. 52, 1279, (1995).

[97] M. Santos, C. Noel, T. Belmonte and L. L. Alves, "Microwave capillary plasmas in helium at atmospheric pressure," Journal of Physics D: Applied Physics, Vol. 47, 265201, (2014).

[98] L. L. Alves, *et al*, "Comparisons of sets of electron-neutral scattering cross sections and swarm parameters in noble gases: II. He & Ne", Journal of Physics D: Applied Physics, Vol. 46, 334002, (2013).